# Diffraction properties of deformed copper single crystals.

A thesis submitted in supplication for the degree of

Doctor of Philosophy.

Vanessa Cheel

Linacre College
Oxford University.

Trinity term 1980.

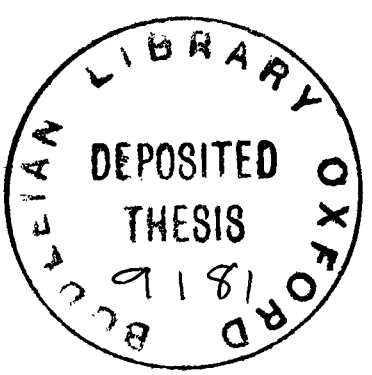

## Abstract

This dissertation concerns the diffraction properties of deformed copper single crystals with emphasis on their behaviour as neutron monochromators. It presents an examination of the effect of crystal imperfection on the diffraction of gamma and neutron radiation, using transmission electron microscopy to determine the detailed defect structure. The basic diffraction equations for transmission geometry are studied as a function of wavelength and thickness for neutrons and γ-rays, and qualitative agreement between experimental and theoretical parameters is obtained. However the theoretical approach is dependent on an idealised defect structure, having a Gaussian distribution of lattice misorientations, which is rarely found in deformed copper single crystals. A relatively simple relationship between γ-ray and neutron rocking curves is only applicable to uniform defect distributions. The wavelength dependence of neutron absorption for the range 0.5 to 5.0Å is established theoretically for various neutron monochromator materials and experimentally for copper. The temperature dependence of this behaviour is also considered.

The γ-ray diffraction is extremely sensitive to variations in the defect structure with position in the crystal, and this sensitivity is found to be dependent on both the dislocation density and the large-scale arrangement of dislocation structures. The dependence of the rocking curve width on the crystallographic direction of incidence could be reproduced qualitatively from a model in which bands of heavily deformed crystal are assumed to delineate regions of relatively perfect crystal. In order to determine defect densities and arrangements from γ-diffraction data x-ray theories were applied, but these also require a uniform microstructure, which was not found in the crystals examined. This is due to the neutron monochromator requirement of a large deformed single crystal. All crystals were deformed in compression, either as flat plates or as large rectangular blocks from which plates were cut.

## Preface

This dissertation is an account of some of the research carried out at the Institut Laue-Langevin, Grenoble, and the Department of Metallurgy and Science of Materials, Oxford, between September 1975 and September 1980. The work described in this thesis is original although the work of others has been drawn on freely, with due acknowledgement in the text.

I would like to express my gratitude to the many people without whose assistance, encouragement and forbearance this work would have been so much more difficult and much less enjoyable. In particular Prof. J. W. Christian who supervised the research with unending patience and faith. My thanks go to Prof. P. B. Hirsch for the freedom of the laboratory in Oxford, and to the I.L.L. for their generous financial support and the provision of facilities.

Linacre College

Oxford

June 1980.

INDEX


| | | Page |
|---|---|---|
| 1. | Introduction | 1 |
| 1.1 | Neutron monochromators: choice of materials | 1 |
| 1.2 | The diffraction process in monochromators | 3 |
| 1.3 | The effects of defect structure on monochromators | 8 |
| 1.4 | Monochromator production techniques | 10 |
| 1.5 | The deformation structure of copper single crystals | 11 |
| 1.6 | X-ray studies of the defect structure of copper single crystals | 14 |
| 2. | Theory and experimental background | 17 |
| 2.1 | γ-ray diffraction | 22 |
| 2.1.1 | The apparatus | 22 |
| 2.1.2 | Theoretical aspects of the experimental work | 25 |
| 2.2 | Neutron diffraction | 32 |
| 2.2.1 | The apparatus | 33 |
| 2.2.2 | Theoretical aspects of the experimental work | 35 |
| 2.3 | Electron diffraction | 40 |
| 3. | Gamma diffraction | 43 |
| 3.1 | Flat plate crystals | 43 |
| 3.1.1 | Crystal PP4 | 45 |
| 3.1.2 | Crystal PP3 | 49 |
| 3.2 | Rectangular block crystals | 54 |
| 3.3 | Small plate crystals | 62 |
| 4. | Electron diffraction | 68 |
| 4.1 | Preparation of foils | 68 |
| 4.2 | Interpretation of electron micrographs | 71 |
| 4.3 | TEM observations | 73 |
| 4.3.1 | The stability of thin foils in the electron beam | 73 |
| 4.3.2 | Glossary of terms used to describe the dislocation structures | 76 |
| 4.3.3 | Crystal PP4 | 77 |
| 4.3.4 | The small flat plates | 86 |
| 5. | Neutron diffraction | 93 |
| 5.1 | Experimental neutron measurements | 93 |
| 5.2 | γ-diffraction measurements | 97 |
| 5.2.1 | The use of γ-diffraction to determine neutron diffraction profiles | 99 |
| 5.3 | The wavelength dependence of neutron absorption | 100 |
| 6. | Discussion | 104 |
| 6.1 | The large flat plate crystals | 112 |
| 6.2 | The rectangular block crystals | 116 |
| 6.3 | The effect of rotation about the scattering vector | 120 |
| 6.4 | Application of x-ray theories to γ-ray measurements | 127 |
| | Conclusions | 134 |
| | References | 136 |
| | Appendix I - tables of results | 141 |
| | Appendix II - additional bibliography | 149 |
| | Appendix III - symbols used in text | 156 |

## 1. Introduction

This study of the diffraction properties of deformed copper single crystals represents a contribution to the investigations into the behaviour of neutron monochromators at the Institut Laue-Langevin. The neutron flux intensity obtained from metal and semiconductor monochromators was always lower than theoretically calculated values by a significant amount, and the production of good monochromator crystals was, until recently, largely a matter of chance. Studies have been undertaken to produce monochromators and monochromator systems consisting of perfect or nearly perfect crystals for special focussing techniques[1-8,11] as well as deformed or doped crystals for normal techniques. This thesis presents an examination of the effect of crystal imperfection on the diffraction of gamma and neutron radiation using transmission electron microscopy to determine the detailed defect structure.

### 1.1 Neutron monochromators: choice of materials.

Neutron monochromatisation by single crystals is based on coherent Bragg scattering and monochromator crystals are chosen for their high intrinsic reflectivity, i.e. the absolute intensity of the Bragg-scattered neutrons is high and the background neutron and gamma-ray intensity is low, while being uniform over the scattered beam cross-section. By suitable choice of Bragg angle, $\theta$, and d-spacing, a small band of any desired wavelength may be selected from a beam of white radiation. The width of such a band depends largely on the horizontal divergence of the beam incident on the monochromator which is typically between 1 and 20 mrad. For maximum resolution this divergence should match the wavelength spread, $\Delta\lambda$, caused by imperfections in the crystal. The function describing the angular range of these imperfections is assumed to be Gaussian and the standard deviation of this function is referred to as the mosaic spread. It is desirable to avoid second and higher order wavelength components,

which is achieved naturally in materials with the diamond structure since the 111 second order structure factor is zero. The low density per square millimetre of neutrons available from reactors necessitates the use of relatively large single crystal monochromators, 5000mm$^2$, to give a usable intensity. This normally precludes the use of isotopes, e.g. Ni$^{58}$, which has otherwise good properties for monochromator.

The intensity of radiation scattered out of a white beam depends inversely on the square of the volume of the primitive unit cell, which restricts the choice of material to those with small unit cells. Another requirement is that the coherent elastic scattering cross-section for neutron interaction with the material is large compared with all other contributions to the total cross-section (i.e. inelastic and incoherent scattering processes, and absorption by nuclear capture).

Materials satisfying these conditions and which have been used as monochromators are aluminium, beryllium, copper, germanium, iron, lead, silicon, zinc and pyrolitic graphite. Beryllium shows the most promise as a monochromator, having a small unit cell, very low absorption and low incoherent scattering as well as a high coherent scattering cross-section. However the as-grown crystals consisted of large sub-grains inclined to each other by relatively large angles[9]. In an attempt to overcome this the crystals are grown by zone-melting[10].

Copper and pyrolitic graphite are preferred to silicon and germanium for short and long wavelength work respectively, but high order contamination has to be eliminated by the use of filters with the consequent loss in intensity. Large crystals of copper, silicon and germanium with homogenous and controlled defect structures are being produced on a routine basis, cut from the central region of even larger, plastically deformed single crystals. In many cases reflectivities close to the theoretical prediction can be obtained.

Pyrolitic graphite was the first monochromator material with good, highly reproducible neutron reflectivities, but its use is limited to long wavelengths and by the fact that its minimum mosaic spread is 7mrad. Metal halide crystals, e.g. Lif, NaCl, $CaF_2$, tend to have a nearly perfect crystal structure with mosaic spreads of the order of 1mrad. The disadvantage of these crystals is their low intrinsic reflectivity which led to their being replaced by lead and copper.

## 1.2 The diffraction process in monochromators

In terms of diffraction properties most real crystals do not behave as either the ideally perfect or the ideally imperfect crystals defined in the theories which exist mainly for these extreme cases (the dynamical and kinematical theories respectively). The former sums the amplitudes of waves excited within the crystal, the latter sums the intensities[12-14].

In order to present a mathematical treatment of the diffraction process in a real crystal, C.G.Darwin[15] modelled the usually complicated defect structure by an assembly of small perfect crystallites, called mosaic blocks, distributed in orientation according to a Gaussian function. The concept of a mosaic block is a purely theoretical one, with no exact interpretation in terms of the crystal defect structure. If the dimensions of these blocks are small enough, kinematic theory can be applied to the calculation of the diffraction profile. The diffraction profile, or rocking curve, is understood to be the variation of reflected intensity as a crystal is rotated through a Bragg reflection in a monochromatic, parallel beam; the detector window being large enough to receive all the diffracted radiation. The integrated intensity, or integrated reflectivity, is the total radiation diffracted into this reflection and is given by the area under the recorded rocking curve. An ideally imperfect crystal would have the maximum integrated intensity

which can be obtained at given diffraction conditions. If the blocks are not thin enough or are too well aligned, or both, corrections for extinction effects have to be applied in order to calculate the diffraction profile. Primary extinction occurs in regions of perfect crystal oriented for Bragg reflection, and is the attenuation of the incident beam by diffraction. The energy of the incident beam is totally transferred to the diffracted beam over a short distance and the phase lag on reflection at each plane leads to beams rediffracted into the incident direction suffering a reduction in amplitude. This effect is particularly severe in Bragg geometry where deeper parts of the crystal may never contribute to the diffraction process. Secondary extinction is due to small regions of perfect crystal being too well aligned as a function of depth in the crystal. The incident beam reaching lower blocks is depleted due to diffraction in upper blocks of the same orientation.

In an ideally imperfect crystal the peak reflectivity must be small to satisfy kinematical theory, whereas in a monochromator a high peak reflectivity over a relatively narrow angular spread is required. Thus a good monochromator crystal may be defined as an imperfect crystal in which there is no primary extinction but a significant amount of secondary extinction, i.e. a crystal containing microscopic blocks of perfect crystal only relatively well aligned. These conditions are wavelength dependent and a given crystal may be ideally imperfect for short wavelengths or weak reflections, but not for longer wavelengths or stronger reflections.

The neutron wavelength dependence of the diffracting properties of imperfect lead and copper single crystals was reported by Dorner[16] who measured reflectivities at two wavelengths, 1·226 and 1·825 Å, and found reasonable agreement with theoretical values calculated using an expression given by Bacon and Lowde[17] and based on the Darwin model.

Dorner used extinction corrections to explain the discrepancy between measured and calculated reflectivities at the longer wavelength and noted reduced peak widths and intensities at the shorter wavelength. Malik[18] made a neutron diffraction study in the wavelength range 0·83Å to 2·39Å with lead, germanium, zinc and beryllium single crystals, comparing measured integrated intensities with those calculated according to an expression given by Dietrich and Als-Nielsen[21] as well as that of Bacon and Lowde. In all cases the measured values were smaller than the theoretical predictions, but no extinction corrections were attempted. The Bacon and Lowde expression formed the basis for the theoretical calculations and neutron diffraction measurements on four different defect structures in a copper single crystal at wavelengths from 0·68Å to 2·4Å reported in this thesis. The effect of crystal thickness at each wavelength was also studied.

The experimentally measured diffraction profile is a multiple convolution of six component distributions: the intrinsic diffraction profile, the source intensity distribution, the angle scale spectral distribution, the crystal size distribution, and crystal imperfection due to lattice strains and/or the angular distribution of the mosaic blocks. In order to correct data for the last three effects, which are termed extinction effects, most experimentalists use Zachariasen's theory[12] for x-ray diffraction based on Darwin's model. More recent improvements to this theory have been based on the Tagaki-Taupin[19,20] dynamical theory of diffraction for a distorted crystal. This formulation gives the diffraction equations in a form readily adaptable to computer use, and is the basis for the simulation of x-ray topograph images. The fundamental equations of the Tagaki-Taupin approach were derived for both x-rays and electrons from the Maxwell or Schrödinger equations

inside a crystalline medium which may contain distortions. This theory, put forward separately by the two authors, gives results coincident with those of the Ewald-Laue theory, Kato's theory[22] and that of Schlangenoto[23]. The electron diffraction theories of Howie and Whelan[24,25], and Wilkens[26] which rely on the column approximation, are a special case of the Tagaki-Taupin formulation. In these theories both the incident and diffracted waves are expressed as composed of two or more plane waves with slightly different wave vectors, so that each of them shows an amplitude and phase modulation. The basic assumption is that the period of the interaction between incident and diffracted beams within a crystal is large compared to the wavelength of the carrier wave, which is of the order of, or less than, an atomic distance. This assumption is valid for a crystal in which the distortion is slight.

Another theory dealing with the refraction of x-rays in a strained crystal was developed by Penning and Polder[27]. They considered that the x-rays were split into beams narrow enough that within the width of a beam the crystal is almost perfect, but wider than the extinction distance. This restricts application of the theory to crystals with very slight distortion in which any part with dimensions of the extinction length can be regarded as almost perfect. Kato[28] and Kambe[29] have independently given theoretical derivations of the theory from the fundamental equations without removing the restriction of very slightly distorted crystals.

Kuriyama[30] proposed a general dynamical theory derived from quantum theoretical considerations and proving some of the assumptions made within the classical dynamical diffraction theory to be unnecessary. In a theoretical study of primary and secondary extinction in imperfect crystals he applied amplitude instead of intensity coupling of incident and diffracted waves and treated extinction as caused solely by

inhomogenous strains in a single coherent domain. . Neither the mosaic block model nor the statistical treatment of imperfections was used.

Kato[28] formulated an energy-transfer equation, from the wave equation of Tagaki-Taupin, for describing secondary extinction. The coupling constants between the incident and diffracted beams were given as being proportional to the kinematical diffracting power per unit length multiplied by the correlation length of the lattice phase factors at two distinct positions, with the limitation that the correlation length was much shorter than the extinction distance. The mosaic block model could be treated as a special case of this theory, and other possible models considered a distribution of elastic strain, or a size distribution of mosaic blocks similar to conventional theory. General relationships were established between the integrated reflecting powers for three types of incident wave; a spherical wave (narrow beam), a plane wave and a wave from an incoherent homogeneous source (wide beam). This theory was extended to less imperfect crystals by considering higher order correlation functions of the lattice phase factors than previously, which leads to reduced coupling constants between the incident and diffracted waves.

Becker and Coppens[31] working within the Zachariasen approximation, which assumes spherical mosaic blocks of uniform size, have published corrections for anisotropic extinction in spherical and non-spherical crystals. Two types of crystal are defined for the extreme cases of extinction dominated by mosaic spread (type I) and extinction dominated by particle size (type II). The type I correction involves the use of an anisotropic mosaic distribution functions, and for type II the average particle shape is described as an ellipsoid rather than a sphere. In each case the six independent components of a symmetrical second order tensor are added to the list of parameters to be refined in a conventional crystallographic least squares program. This approach is limited to intensity coupling between incident and diffracted radiation, and treatment of primary extinction is rather oversimplified.

Extinction in parallelopiped crystals was investigated theoretically by Werner[34], who derived an expression for the secondary extinction coefficient from exact solutions of the transport equations. Werner suggests a correction for primary extinction which is valid only in the case of small extinction effects, as are most corrections. Despite the development of diffraction theories for imperfect single crystals, these have not been correlated with the defect structure of the samples via measurable quantities describing the degree of imperfection of the crystals, and Darwin's cruder approximation is still widely used in the form of Zachariasen's theory.

## 1.3 The effects of defect structure on monochromators

The effect of dislocation density and arrangement on the diffraction profile is of importance for monochromator crystals. From integrated intensity measurements on lightly deformed copper single crystals for a series of x-ray wavelengths, Freund[32,33] derived mosaic block sizes roughly corresponding to published values of the mean distance between dislocations. This was found to vary as the negative half power of the dislocation density. For more heavily deformed crystals with a dislocation density of greater than $10^{6}\,mm^{-2}$, which gives the appropriate mosaic spread for neutron monochromators, the block size was comparable to the width of the glide bands in which the dislocations were arranged. However where dislocations concentrate in low angle grain boundaries, this gives rise to uneven mosaic distributions. Such inhomogeneities in angular and spatial mosaic distributions are responsible for poor monochromator performance. These effects are observed as multiple peak rocking curves when recorded with short wavelength gamma radiation, whereas approximately the same crystal volume gives a smoothly varying, single peak, neutron diffraction profile.

Schneider[35] used the diffraction of 412keV gamma radiation to study rocking curves from copper, beryllium and tungsten single crystals. The γ-radiation can be obtained at high intensity, with low absorption, and will penetrate 80mm of copper. The rocking curves were found to vary in shape, height and width with position in the crystal. The mosaic distributions did not take either Gaussian or Lorentzian form. They were determined assuming negligible extinction effects, since measured and kinematical integrated intensities agreed to within a few percent, by substituting measured reflectivities into the expression for the mosaic distribution in the theoretical reflectivity equation. Schneider showed that increasing secondary extinction had the effect of intensifying any irregularities in the diffraction profile. A further investigation of secondary extinction effects in a large copper single crystal with an inhomogeneous mosaic structure indicated that the secondary extinction measured in such a crystal is greater than that generally assumed for a homogeneous mosaic spread. The cross-section of a neutron beam is commonly twenty times that of a γ-ray beam and this leads to a smoothing of the neutron profile due to spatial averaging.

In the determination of the mosaic distribution parameters of a $2mm^3$ copper single crystal with γ-ray and neutron radiation[36], the mosaic structure was found to vary with the direction of incidence on rotating the crystal about the scattering vector (i.e. rotating the scattering planes about the plane normal). Schneider and Lehmann measured the full width at half maximum intensity, (FWHM), of rocking curves for different azimuthal angles $\phi$. A polar plot of FWHM as a function of $\phi$ when measured with γ-rays had a peanut-shell form, whereas with neutrons the distinctive minima were smoothed out and the trace was elliptical. The shape of the γ-ray plot was explained in terms of bent lattice planes and an 'intrinsic mosaic spread' which is that corresponding

to the minimum FWHM measured. They assumed the maximum FWHM to be a sum of the broadening due to the curvature and the local mosaic spread. This anisotropy, said to be due to many straight edge dislocations aligned parallel to each other on{111} planes, was used by Freund[32] to obtain a variation in experimental resolution using the same set of reflecting planes and rotating the monochromator crystal.

## 1.4 Monochromator production techniques

There are three basic techniques for the production of monochromator crystals:

(a) the variation of growth conditions and the addition of impurities[37].

(b) machining the reflecting surfaces of crystals[38].

(c) the plastic deformation of crystals[39-42].

Schneider and Stump[43] produced well-controlled, homogeneous mosaic spreads by diffusing deuterium into niobium single crystals under conditions for which the cubic $\alpha$-phase coexists with the orthorhombic $\beta$-phase. The misfit dislocations introduced between the different phases give lattice distortions and particle sizes corresponding to neutron mosaic widths of between 3 and 9 mrads depending on deuterium concentration. The reflectivity is comparable with that of copper. However, the crystal preparation is lengthy and requires ultra high vacuum treatment at temperatures greater than 2000$^{o}$C.

In the earliest experiments by Sturm[44] the surfaces of metal halide crystals, notably lithium fluoride, were roughened giving a significant increase in reflectivity. This technique only works for materials with a relatively high absoprtion coefficient for neutrons so that the beam only penetrates the surface layers for which the mosaic spread has been increased. With calcium fluoride and potassium bromide the absorption is less and so correspondingly is the reflectivity increase.

Early attempts to improve crystal reflectivities were made by Schull[42] who deformed germanium and silicon single crystals, and by Barrett, Meuller and Heaton[40] who pioneered the technique of uniaxial compression along [110]. Experience has shown that plastic deformation gives the best results for homogeneity of mosaic spread and block size, which is necessary to give a reflected beam of uniform intensity across the reflecting volume. Vertically and horizontally focussing monochromators have been made by glueing slabs of plastically deformed, single crystal copper onto an aluminium support and these gave satisfactory agreement with theory. A similar experiment with hot-pressed silicon was less successful due to inhomogeneities within the plates.

## 1.5 The deformation structure of copper single crystals

During the past twenty years very few studies of uniaxial compression of copper single crystals have been reported. LeHazif et al[45] investigated {110}<110> slip in f.c.c. crystals deformed in compression at high temperatures: Jazienski et al[46] investigated twin formation during dynamic compression of [110] oriented copper single crystals in the form of blocks 10 x 10 x 4.5mm$^2$. The samples were deformed at strain rates greater than $10^2 s^{-1}$ for slip line analysis, x-ray pole-figure studies and transmission electron microscopy to determine the deformation mechanism.

Vorbrugg[47] et al have published work hardening and surface investigations on copper single crystals oriented for multiple glide in tension. They found that [110] crystals show the same work hardening behaviour as single glide crystals, whereas in [111] and [100] crystals multiple glide is fundamental. Takeuchi[48] studied the work-hardening of copper single crystals with multiple glide orientations, including [101] and [111] compression axes. He used optical microscopy of slip band patterns to determine the operative systems in crystals 2.1 x 5.4 x 10mm. For

crystals in compression along [101], it was found that although the orientation is geometrically stable, slip tended to occur on one system locally. This was possibly due to particular combinations of slip vectors producing abnormal dislocation multiplication. These results were compared with tensile tests on similar crystals.

The dislocation structure of copper as a function of strain when deformed in uniaxial tension is well documented. Detailed investigations employing a variety of techniques[49] and giving reasonably consistent results, have been published. The distinct stages of the stress-strain curve are only observed for crystals deformed in single glide. The absence of easy glide in the compression of single slip orientations is due to squat or flat specimen shapes[50]. Curves for multiple glide orientations deformed in compression are similar to those for multiple glide in tension. When multiple slip occurs the crystal rapidly strain hardens and Takeuchi has shown that for [101] oriented copper single crystals, the work-hardening rate in compression is twice that in tension. For [112] crystals he found the rate to be approximately the same in tension and compression.

Dislocation densities and arrangements have been determined using etch pit counts and transmission electron microscopy with crystals both in the stress-applied and relaxed conditions. Essmann[51], Gottler[52] and Mughrabi[53] have shown that there are significant differences between the dislocation structures while the crystal is under load and that following load removal. These measurements were performed by comparing transmission electron micrographs of crystals irradiated with fast neutrons while under tension to pin dislocations, with micrographs of equivalent crystals given the same deformation but not irradiated. The dislocation structure follows the same general trends with increasing

applied stress in both cases, but in the stress-applied condition the dislocation density was greater than in the relaxed state. It was also suggested that dislocation pinning was necessary to prevent loss of dislocations during the preparation of thin foils for the electron microscope. The regions of the work hardening curve investigated using these techniques were stage I, early stage II and the stage I - stage II transition. For crystals deformed into stages II and III it is likely that the influence of dislocation tangles and arrays prevents the escape of dislocations during thinning[54].

Stage I of the stress-strain curve is characterised by dislocation braids [52,55] running parallel to a [110] direction and consisting of primary edge dislocation dipoles spaced 50 - 100μm apart. A combination of slip line and etch-pit measurements was necessary to obtain details of large scale dislocation structures since visible areas in the electron microscope were of the order of 100 x 30μm.

In the stage I - stage II transition the dipoles 'catch' dislocations forming the beginning of cell walls aligned along the [$\bar{1}$10] direction[54]. As the deformation proceeds the two dimensional cell structure becomes more clearly defined, parallel to the active slip planes. Crystals oriented for single glide show a less open structure than those oriented for double glide[55]. The higher dislocation density in the cell walls is proportional to the tensile stress[54-56]. With increasing applied stress the dislocation density in the cell walls increases, while the ratio of cell wall thickness to dislocation-free area remains constant, i.e. the structure becomes finer while remaining similar to that in early stage II. Kawasaki[55] describes the structure for double glide in stage III as a grid of parallelograms based on the active slip planes.

From investigations in single glide, Steeds [54] constructed a model of the cell structure in stage III. It took the form of an octagonal

pillbox with sides composed of dense multipole walls and elongated arrays, and having at their edges tilt and twist boundaries. Such cells had linear dimensions of the order of tens of microns. In stage III the degree of misorientation between regions increases in magnitude to the order of several degrees or more[54]. Low temperature tensile tests[57] with crystals oriented for double slip and deformed into stage III showed inhomogeneities in the slip line patterns which, on examination by transmission electron microscopy, turned out to be due to the formation of large angle grain boundaries with misorientations of $25^{\circ}$ - $30^{\circ}$. The planes of the 2-dimensional cell structure, by stage III, were inclined slightly to the slip planes.

A pillbox structure composed of hexagonal dislocation loops was developed for computer studies of the stress fields associated with a dislocation cell structure[58]. On repetition the hexagonal loops formed sub-boundaries of simple cells made up of screw dislocations. Other prototype units, triangular and star-shaped, were considered and it was shown that the hexagonal unit could be built up into an aggregate of cells of similar sizes but with opposite senses of misorientation. Evidence for such a structure in fatigued germanium, with cells aligned parallel to {111} planes along <110> directions, was given by Scoble and Weissman[59].

## 1.6 X-ray studies of the defect structure of copper single crystals

X-ray measurements are restricted by the high absorption of this radiation exhibited by copper. X-ray topography is limited to very lightly deformed crystals for the resolution of detailed structure, but may be used to image macroscopic dislocation distribution over dimensions of greater than 50μm. Wilkens[60] used the Berg-Barrett

technique to obtain topographs showing traces of dislocation layers parallel to the primary slip planes, and contrast due to kink walls. He achieved a resolution of about 5μm.

A general concept of the effect of imperfections on x-ray diffraction properties has been published by Krivoglaz[61] based on kinematical theory and giving line broadening[62] as a special case. The broadening of x-ray line widths using nearly perfect[63,64] and plastically deformed crystals has been used to derive dislocation densities and distributions. Wilkens[64] followed the theory of Krivoglaz and Ryaboshapka[62], modified to fit a model consisting of a restrictedly random distribution of dislocations parallel to the axis of a cylinder. The dislocation densities derived from this agreed well in comparison with densities obtained from transmission electron microscopy investigations[64]. Another theory derived expressions for the probable misorientations introduced by dislocations in a crystal and the contributions to measured rocking curve half-widths of tilts and strains, again assuming Gaussian or Cauchy distributions. This treatment holds for as-grown crystals and those with low densities of dislocations, for which tilt broadening was found to be independent of Bragg angle, whereas the strain contribution was a function of $\tan\Theta$.

The effect of dislocations on integrated intensities and rocking curve widths from deformed copper single crystals was reported by Bachmann et al[66]. They found that changes in these parameters can be described by a model of independently scattering perfect crystal blocks at low dislocation densities ( $2 \times 10^3 mm^{-2}$), and at higher densities the variations are due mainly to lattice tilts.

Warren and Averbach[67], working with gold filings and cold rolled

copper -2% silicon single crystals, were able to differentiate between strain broadening and particle size broadening in x-ray line widths. Their general theory expressed the shape of a diffraction profile as a Fourier series, the coefficients of which could be separated for the two types of broadening. From the particle size broadening coefficients an average particle size was derived and from the remaining coefficients, root mean square strains were obtained, but the application is limited to small strains. They also used the same approach to correct for thermal diffuse scattering in experimentally measured curves.

## 2. Theory and experimental background

The basis for most modern diffraction theories applied to neutron and gamma-ray experiments has been described by Zachariasen[12], amongst others, who enlarged on the Darwin-Ewald equations and presented a dynamical theory for x-rays. He derived the power equations for a perfect crystal with zero absorption in the forms necessary for comparison with the various experimental parameters. The experimentally measured quantities are (1) the power of the incident beam $P_o$, or of the transmitted beam, $P_T$, when far from the Bragg reflecting position, and (11) the energy recorded as a function of crystal rotation through the Bragg reflection, $P_H$. The reflectivity as a function of the relative angle between the scattering planes and the incident radiation, $\omega$, is given by the power ratio $P_H(\omega)/P_T$ or $P_H(\omega)/P_o$; and the integrated reflectivity, the area under the diffraction curve, is obtained by summing this ratio over $\omega$. The characteristics of the diffraction peak thus derived are the peak reflectivity, $r_p$, which is the maximum ordinate of the diffraction pattern expressed as a percentage of the incident radiation; the full width at half maximum intensity, $\beta$, and the integrated reflectivity, $R_\Theta$. Since the experimental work for this thesis was performed in Laue transmission geometry, only the theory relevant to this case will be given. In Laue geometry the transmitted and diffracted beams leave the crystal through the face opposite to that through which the incident beam entered. The reflecting planes are perpendicular to the entry and exit surfaces for symmetrical Laue geometry.

The power transfer equations for a crystal, including the effects of absorption, were given by Zachariasen for a plane parallel perfect crystal plate in which the polarisability and refractive index were complex functions, i.e. the conditions for dynamical theory. The

equations presented here were derived for crystals with an inversion centre so that the quantities involved are real. Zachariasen used a parameter $\kappa$, dependent on the real and imaginary parts of the structure factor, and a factor A to select the form of the diffraction equations applicable in each case. $\kappa$ is a measure of the absorption and related to the anomalous dispersion of electrons in the outer valence shells. It is assumed, justifiably, to have a value small compared to unity. The term A, dependent on structure factor, incident wavelength, and crystal parameters, characterises the behaviour of a given crystal.

$$A = \frac{r_o F \lambda T_o K}{\gamma V} \qquad 2\cdot1$$

where F is the structure factor, V the unit cell volume, $\lambda$ the incident wavelength, $T_o$ the crystal thickness and $\gamma$ is the cosine of the Bragg angle. The classical electron radius $r_o = e^2/mc^2$ and the polarisation factor $K = \frac{1+\cos^2 2\theta}{2}$.

In casting the power equations an exponential term accounting for the linear absorption is introduced. Experimentally this term is included by using the transmitted beam intensity as the normalising factor.

The equations of dynamical theory for a perfect crystal predict values which are much smaller than measured values and to explain this the mosaic structure model for a real crystal was proposed by Darwin. He suggested that crystals have inherent imperfections in one of two forms; either a warping of atomic layers or an arrangement of misaligned blocks of perfect crystal. The term 'mosaic structure' was coined by P.P.Ewald for the latter model, which was adopted because it was mathematically simpler. Since relative displacements of the blocks are large compared with the incident radiation wavelengths, it is assumed there are no definite phase relationships between scattering

from various blocks, i.e. the real crystal is an aggregate of independently scattering perfect crystals.

The theory was derived for x-rays in a plane-parallel crystal plate of thickness $T_o$, composed of mosaic blocks in the form of small perfect crystal plates nearly parallel to each other and the large plate. It is assumed that the thickness of each block fluctuates about a mean value, $t_o$, which is sufficiently small for primary extinction to be neglected. The power loss due to both primary and secondary extinction effects may be estimated in terms of an effective absorption coefficient $\mu_e$.

$$\mu_e = \mu_o + \zeta\sigma \qquad 2\cdot2$$

where $\zeta\sigma$ is the fractional power loss due to diffraction per unit path length, and is called the secondary extinction coefficient, and $\mu_o$ is the linear absorption coefficient.

For convenience the distribution function $W(\Delta)$ describing the orientation of the mosaic blocks is assumed to have cylindrical symmetry and to be given by an error function

$$W(\Delta) = \frac{1}{\eta\sqrt{2\pi}} \exp\left(-\frac{\Delta^2}{2\eta^2}\right) \qquad 2\cdot3$$

The standard deviation of this function, $\eta$, is the mosaic spread parameter and related to the measured full width at half maximum $\beta$, of a diffraction peak by

$$\beta = \eta 2\sqrt{2 \ln 2} \qquad 2\cdot4$$

$\Delta$ is the deviation from the exact Bragg angle.

The scattering power was derived for a layer of thickness dT containing many mosaic blocks conforming to the same distribution function as for the crystal as a whole. The expression for the reflecting power of a block is that for a perfect crystal with zero

absorption

$$\frac{P_H(T)}{P_o(0)} = \frac{\sin^2(A\sqrt{1+y^2})}{1+y^2} \qquad 2.5$$

$$y = \frac{T_o \Delta\pi \sin 2\Theta}{A\lambda\gamma}$$

where $P_H(T)$ and $P_o(0)$ are diffracted and incident intensities (respectively) at a depth T in the crystal. On the assumption that the half-width of the function $W(\Delta)$ is much greater than that of the diffracted intensity distribution for a single perfect crystal block, which differs from zero only in a narrow range, $W(\Delta)$ can be treated as a constant, giving for a layer of thickness dT

$$\sigma\, dT = \frac{WR\,dT}{t_o} \qquad 2.6$$

where R is the integrated reflectivity.

This value for $\sigma$ is then used in Darwin's coupled equations

$$\begin{aligned} dP_o &= -\mu_o P_o \frac{dT}{\gamma} - \sigma P_o dT + \sigma P_H dT \\ dP_H &= -\mu_o P_H \frac{dT}{\gamma} - \sigma P_H dT + \sigma P_o dT \end{aligned} \qquad 2.7$$

describing the power variation in the transmitted and diffracted beams to get an expression for the power ratio $P_H/P_0$

$$\frac{P_H(T)}{P_o(0)} = \sinh\sigma T_o \exp\left[-\left(\frac{\mu_o}{\gamma} + \sigma\right)T_o\right] \qquad 2.8$$

The implicit form of $\sigma$ must be used in the case where the standard deviation of the W function is comparable to the half width, $\Theta'$, of the perfect crystal diffraction pattern.

$$\sigma = \frac{1}{t_o}\int_{-\infty}^{\infty} W(\Delta)\ \frac{P_H}{P_o}(\Theta_B - \Theta' + \Delta)\, d\Delta \qquad 2.9$$

Assuming that for the Laue case the crystal plate is reasonably thin, i.e. $\sigma T_o \ll 1$, so that a series expansion of equation (2.8) is justified, the equation for an ideally imperfect crystal can then be given for the following cases: (i) negligible primary and negligible secondary

extinction, (ii) negligible primary and small secondary extinction, (iii) small primary and small secondary extinction.

Case (i) - both primary and secondary extinction are negligible.

When A has a value very much less than unity, i.e. the crystal is "thin" with respect to the reflection and wavelength used, kinematical theory is applicable as a limiting case of dynamical theory. The diffraction pattern of the ideal crystal has the same shape and FWHM as the distribution function $W(\Delta)$, and the integrated reflectivity normalised to the transmitted intensity is given by

$$R_\Theta = \frac{QT_0}{\gamma} \exp\left(-\frac{\mu_0 T_0}{\gamma}\right) = R_K \qquad 2\cdot10$$

where

$$Q = \frac{r_0^2 K \lambda^3 F^2}{V^2 \sin 2\Theta} \qquad 2\cdot11$$

The secondary extinction coefficient $\zeta\sigma$ is given by

$$\zeta\sigma = QW(\Delta) \qquad 2\cdot12$$

and the reflectivity as a function of rotation angle is the power ratio

$$r_{th}(\Delta) = \frac{P_H(T)}{P_0(0)} = \frac{W(\Delta)QT_0}{\gamma} \exp\left(-\frac{\mu_0 T_0}{\gamma}\right) \qquad 2\cdot13$$

Case (ii) - negligible primary and small secondary extinction.

For values of $\zeta\sigma$ which are small compared with $\mu_0$ but not negligible, it is necessary to include in the power equations the second term in the expansion of equation (2·8). Then the predicted reflectivity is smaller than in case (i) giving better agreement with measurements. The mean secondary extinction coefficient is proportional to Q, i.e. to $F^2$, and this indicates that secondary extinction is greater for the stronger reflections. The reflectivity in this case is

$$r_{th} \cong \frac{W(\Delta)QT_0}{\gamma} \exp\left(-\frac{\mu_0 T_0}{\gamma}\right)\left[1 - \frac{W(\Delta)QT}{\gamma}\right] \qquad 2\cdot14$$

and

$$R_\Theta \cong \frac{QT}{\gamma} \exp\left(1 - \frac{(\mu_0 + jQ)T_0}{\gamma}\right) \qquad 2\cdot15$$

where $jQ$ is the mean secondary extinction coefficient given by

$$jQ = Q\int W(\Delta)^2 \, d\Delta \qquad 2\cdot16$$

and using equation (2.3)

$$j = \frac{1}{\eta\sqrt{2\pi}} \qquad 2\cdot16a$$

Case (iii) - small primary and secondary extinction.

When the thin crystal approximation is no longer valid, the general expression for the integrated reflectivity, including primary extinction, must be used. This is

$$R_\Theta = \frac{Qf(A)t_0}{\gamma} \qquad 2\cdot17$$

where $f(A)$ takes the value unity for $A \ll 1$, and for $|A\cos 2\Theta| \gg 1$ it is

$$f(A) = \frac{1 + |\cos 2\Theta|}{2A\left[1+\cos^2 2\Theta\right]} \qquad 2\cdot18$$

This factor applies as a correction for primary extinction and from this it can be seen that both primary and secondary extinction decrease with decreasing wavelength and structure factor.

Finally when the thickness of the mosaic blocks is such that $\frac{\mu_0 t_0}{\gamma_0}$ is comparable to or greater than unity, the original transfer equations must be replaced by the corresponding difference equations.

## 2.1 Gamma-ray diffraction

### 2.1.1 The apparatus

The scattering of γ-radiation is analogous to that of x-rays and the same polarisation and form factors are used. The significant difference is that for the higher energy γ-rays the linear absorption

coefficients are much smaller than those for x-rays, and are comparable to those of neutrons. Thus the same considerations which apply to neutron diffraction can be applied to the diffraction of γ-rays.

The γ-ray diffractometers developed at the Institut Laue-Langevin are small angle scattering devices for studying crystals in Laue geometry. They consist of a gamma-ray source, beam defining slit, goniometer and counter, all mounted on a steel beam 6m. long (fig. 2.1). The source is a neutron-irradiated gold foil of cross-section 0·2 x 10 x 4mm long. The decay reactions are

$$^{197}Au\ (n, \gamma)\ ^{198}Au \xrightarrow{e^-} {}^{198}Hg + \gamma\ (412keV)$$

$$^{198}Au\ (n, \gamma)\ ^{199}Au \rightarrow {}^{199}Hg + \gamma\ (^{208}_{158}keV)$$

The use of a pulse height discriminator for the interval 350 - 500keV eliminates the lower energy radiation. The half-life of the 412keV radiation is 2·7 days, the initial flux of a monochromatic primary beam with horizontal divergence 0·05mrad, vertical divergence 2·3mrad, is of the order of $2{\cdot}5 \times 10^3$ photons.$mm^{-2}.s^{-1}$. The length of the foil is limited to 4mm by the strong self-absorption of the 412 keV radiation in gold. The absorption of this radiation in air is negligible and the count rate using a NaI(Tl) scintillation counter is about 5000 cps with a new source. The wavelength of the radiation is 0·0302 Å with an energy resolution $\Delta E/E$ of $10^{-6}$.

The collimator consists of a pair of lead blocks 60mm thick in the direction of the primary beam, with milled slots 10mm high by 0·2, 0·5, or 1mm wide, giving angular divergences in the primary beam of 0·05, 0·15, and 0·3 mrad. The precise rotation of the goniometer is controlled by a Slo-syn step motor which is directed by digital electronics. The motor drives a micrometer tangent screw which displaces a spring loaded

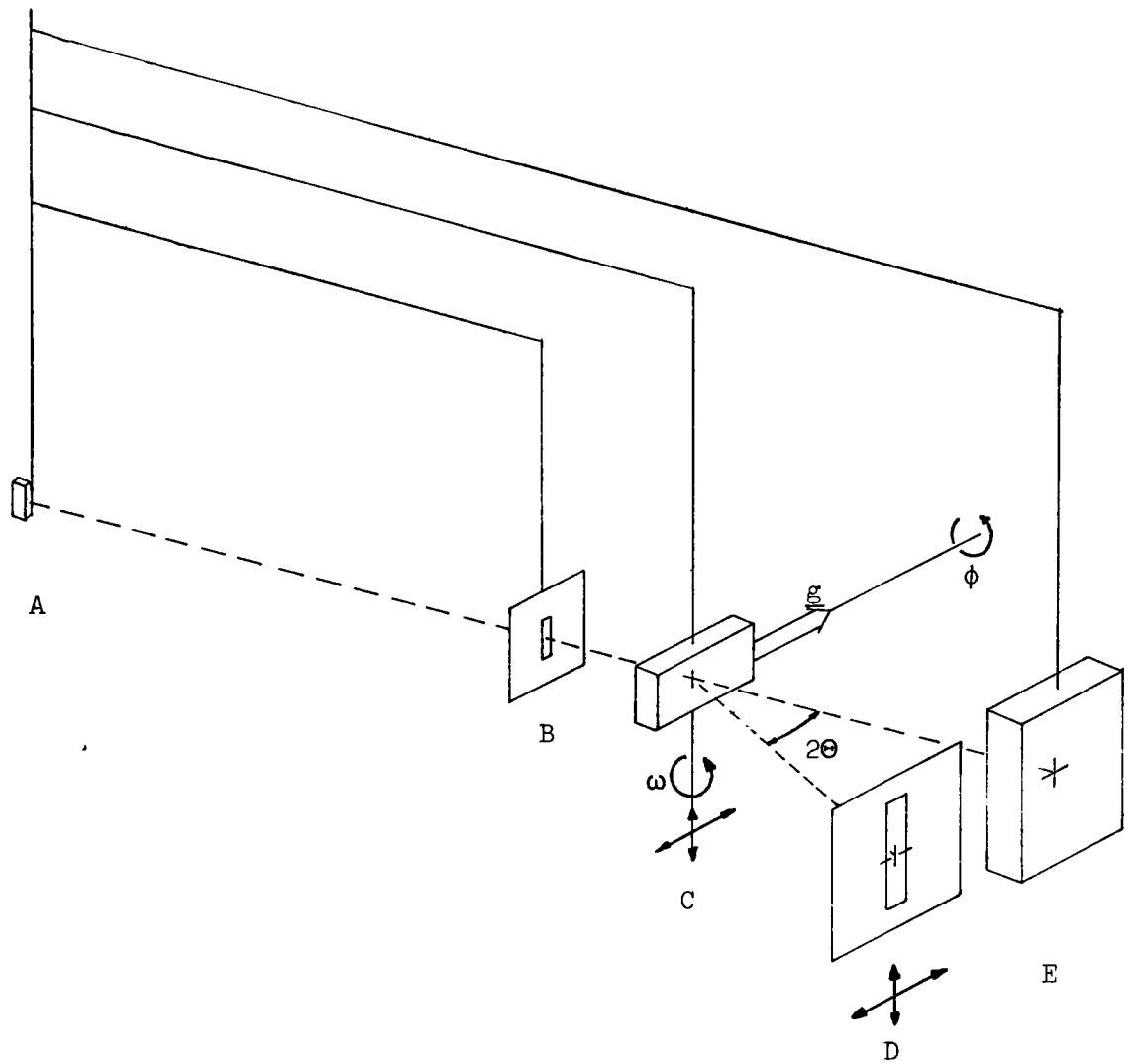


Figure 2.1

A schematic layout of a gamma-ray diffractometer showing:

A the γ-ray source, a gold foil of dimensions 0.2 x 4 x 10mm.

B the beam defining slit of dimensions typically 0.5 x 10mm.

C the sample on a goniometer which has two degrees of translational freedom as shown by the arrows, and the rotation, ω, through the Bragg reflection.

D the variable width receiving slit with two degrees of translational freedom.

E the beam stop, a lead block.

$\underline{g}$ the scattering vector, and ϕ is the rotation about $\underline{g}$.

lever arm fixed to a rotating table. One motor step gives a rotation of 0·01 mrad about the z-axis. Various sliding carriages and goniometer heads are mounted on the rotating table, giving translation and rotation about x- and z- directions (y- direction is the primary beam direction) for investigation of different volume elements.

The detector consists of a NaI(Tl) scintillation crystal, an EMI 9656 photomultiplier and a preamplifier. The variable width receiving slit, two lead plates 20mm thick, is placed parallel to the x and z axes. An energy resolution of about 10% can be obtained with a high tension of 1kV.

For a beam with cross-section 0·2 x 10mm, the ratio of primary beam intensity, $I_o$, to background intensity, $I_b$, is of the order of $10^3$ when measured with a receiving slit 2mm wide. Even for a crystal with 1% maximum reflectivity, the ratio $I_o/I_b$ is about 10.

Data is recorded in the form of an intensity versus angle of crystal rotation ($\omega$) plot on a chart recorder, in conjunction with a printed paper tape listing the number of counts in a given unit of time for a given angular step width. One diffractometer had the facility for producing a punched paper tape containing the data.

2.1.2 Theoretical aspects of the experimental work.

For $\gamma$-radiation of 0·0302 Å wavelength and a copper single crystal, the calculated dynamical half-width is of the order of $2{\cdot}4 \times 10^{-3}$ mrad for the 111 reflection and the mean free path is about 12mm. Thus the conditions for the application of the Zachariasen theory should be fulfilled for a number of crystals when studied on the diffractometer. Primary extinction can be eliminated or reduced by increasing the number of defects in the crystal (e.g. by deformation or fast neutron irradiation) to give small mosaic blocks, or by increasing the extinction length on changing the wavelength to values of $10^{-2}$ Å. In order to show dynamical

diffraction effects the crystal must be thicker than the extinction length which is defined as the thickness corresponding to Zachariasen's parameter A being equal to unity. In copper with 0·03Å radiation the extinction length is approximately 65μm for the 111 reflection, about 70μm for the 200 reflection and 90μm for the 220 reflection. This extinction length is the wavelength of the macroscopic variations in incident and diffracted beams, §1·2.

If the size of the perfect domains in the bulk crystal is of the order of or smaller than 10μm, primary extinction can reasonably be neglected and equations (2·10), (2·13) are applicable. $\sigma(\omega)$ becomes equal to $Q\mathcal{W}(\omega)$ and the extinction correction depends only on the mosaic distribution function. Assuming the validity of the Darwin transfer equations, the reflectivity per unit angle, normalised to the transmitted intensity, is obtained by rearranging equation (2·8) to

$$\frac{\mathcal{P}_H(\omega)}{P_T} = r_{th}(\omega) = 0{\cdot}5\left[1 - \exp\left(-\frac{2QTW(\omega)}{\gamma}\right)\right] \qquad 2{\cdot}19$$

If the measured integrated reflectivity is within a few percent of the kinematical value, primary and secondary extinction are negligible and the mosaic distribution function may be deduced directly from the measured values. A copper crystal of thickness 12mm satisfies these conditions if the measured peak reflectivity is about 2%. Assuming negligible primary extinction, a measure of the secondary extinction is obtained from the experimental and theoretical integrated reflectivities $R_m$ and $R_k$ respectively. This parameter, $E_s$, is usually given as a percentage

$$E_s = \frac{R_k - R_m}{R_k} \times 100 \qquad 2{\cdot}20$$

At the angular position for maximum intensity $\omega = 0$, the expression for $W(\omega)$ takes the value $(\eta\sqrt{2\pi})^{-1}$, which on substitution in equation (2·19)

gives an expression for the theoretical peak reflectivity. When the reflectivity is normalised to the incident intensity the term $\exp(-\frac{\mu T}{\gamma})$ is included.

$$r_p = 0{\cdot}5 \exp\left(\frac{-\mu T}{\gamma}\right)\left[1 - \exp\left(\frac{-2QT}{\gamma\eta\sqrt{2\pi}}\right)\right] \qquad 2{\cdot}21$$

The effect of linear absorption on the peak reflectivity, as shown by including this term, can be seen by comparing figures (2·5) and (2·4). These graphs represent the behaviour of peak intensity with increasing mosaicity for various crystal thicknesses for the 220 reflection. Figure 2·5 is based on equation (2·21) excluding the absorption term, and figure 2·4 includes it. The peak reflectivity is very sensitive to small changes in mosaicity up to a mosaic spread of about 0·4 mrad, and when normalised to the incident beam intensity is sensitive to thickness as well. The dependence on mosaicity is more clearly seen in figure 2·5. For the 200 and 111 reflections the behaviour is similar but peak reflectivities are higher for a given mosaicity.

The thickness dependence of the peak reflectivity for a given mosaicity is shown in figure 2·2b for the 220 reflection and figure 2·2a for the 111 reflection. The broken line through the peak maxima is the trace of the optimum thickness as a function of mosaicity, which is shown more clearly in figure 2·3. Rearranging equation (2·21) and maximising the peak reflectivity, an expression for the optimum thickness as a function of the linear absorption, mosaicity, and factor Q, is obtained.

$$T_{opt} = \frac{\gamma\eta\sqrt{2\pi}}{2Q}\ln\left(1 + \frac{2Q}{\eta\gamma\sqrt{2\pi}}\right)^{-1} \qquad 2{\cdot}22$$

This is shown graphically as a function of mosaicity in figure 2·3 for the 220, 200 and 111 reflections. A saturation value is reached for the 220 reflection at a thickness of 12·34mm and a mosaic spread of 1 mrad, which corresponds to a FWHM of the order of 2·3 mrad in a measured peak.

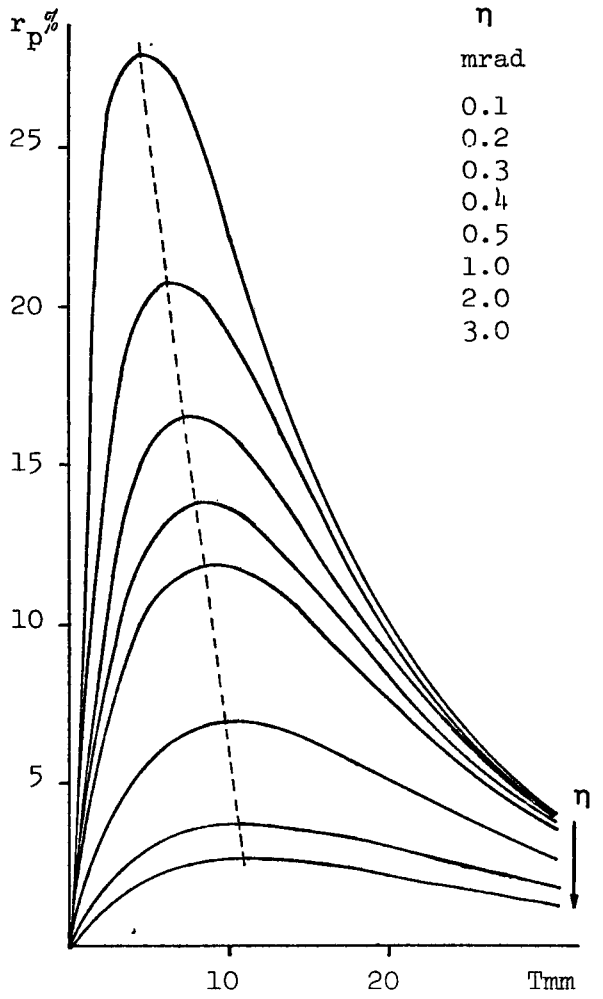


Figure 2.2a

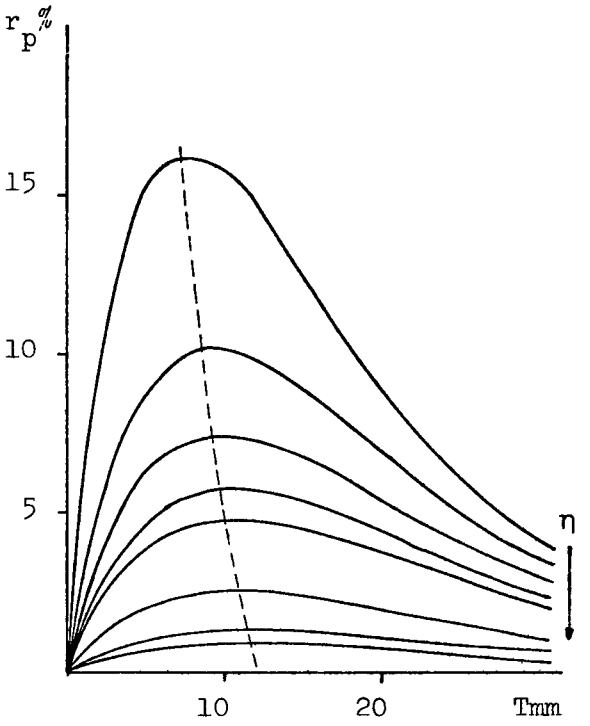


Figure 2.2b

These figures show the thickness dependence of the peak reflectivity for various mosaic spreads, η, which are increasing in the sense of the arrows. The broken line represents the optimum thickness (figure 2.3 Figure 2.2a is for the 111 reflection and fig.2.2b for the 220 reflection.

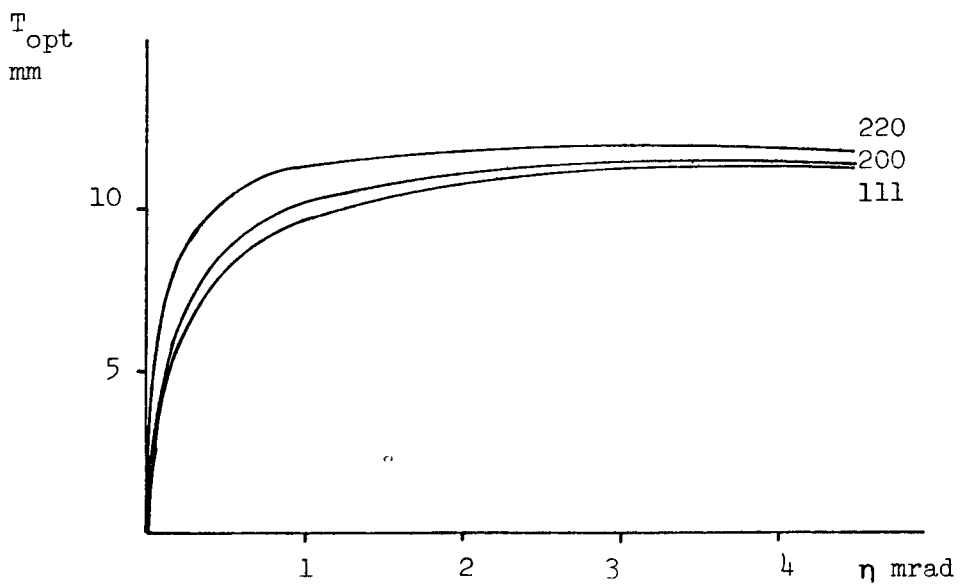


Figure 2.3. The optimum thickness as a function of mosaicity for the reflections 220, 200, 111; corresponding to the broken line in the figure above. These figures are for γ-radiation.

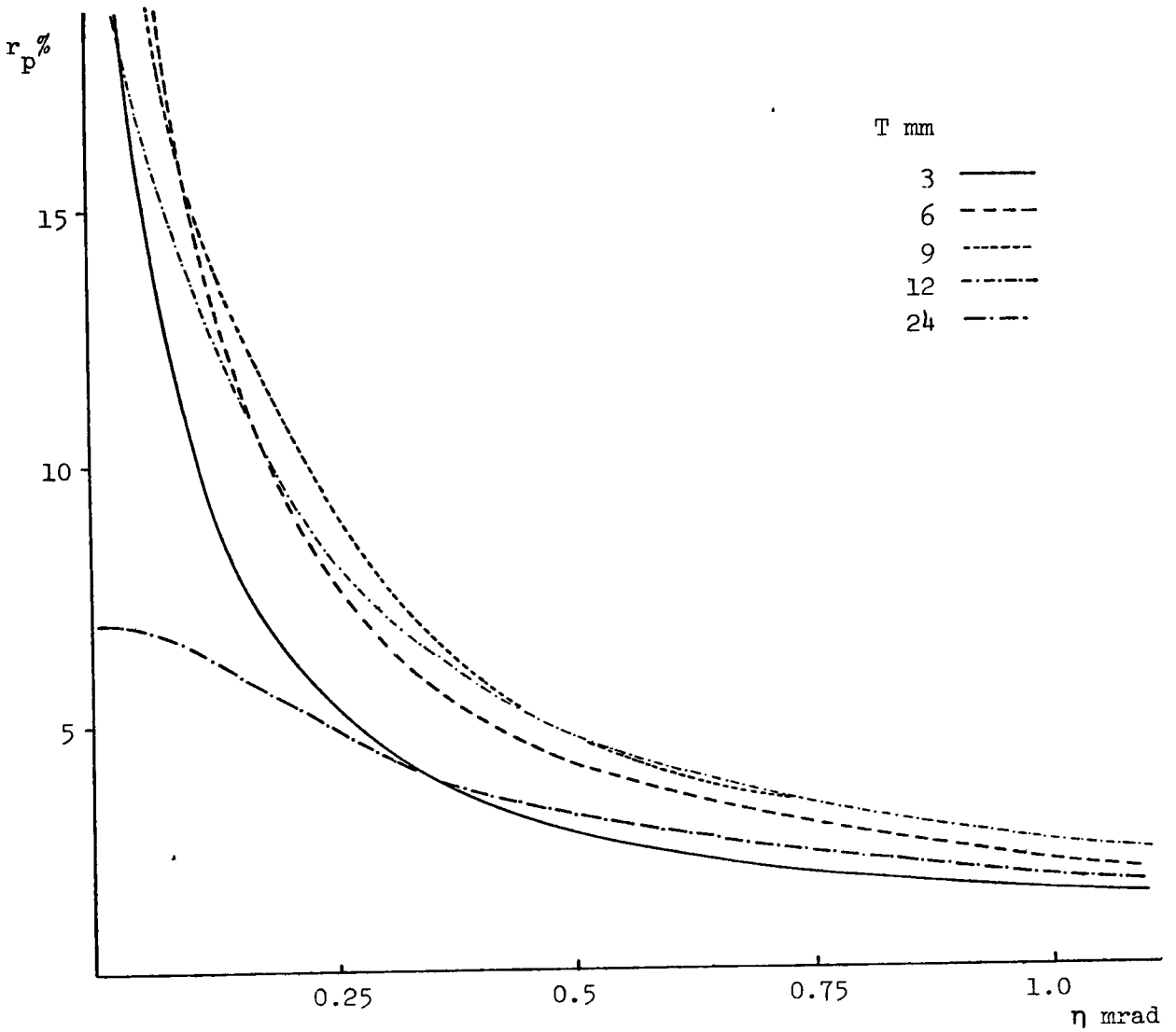


Figure 2.4

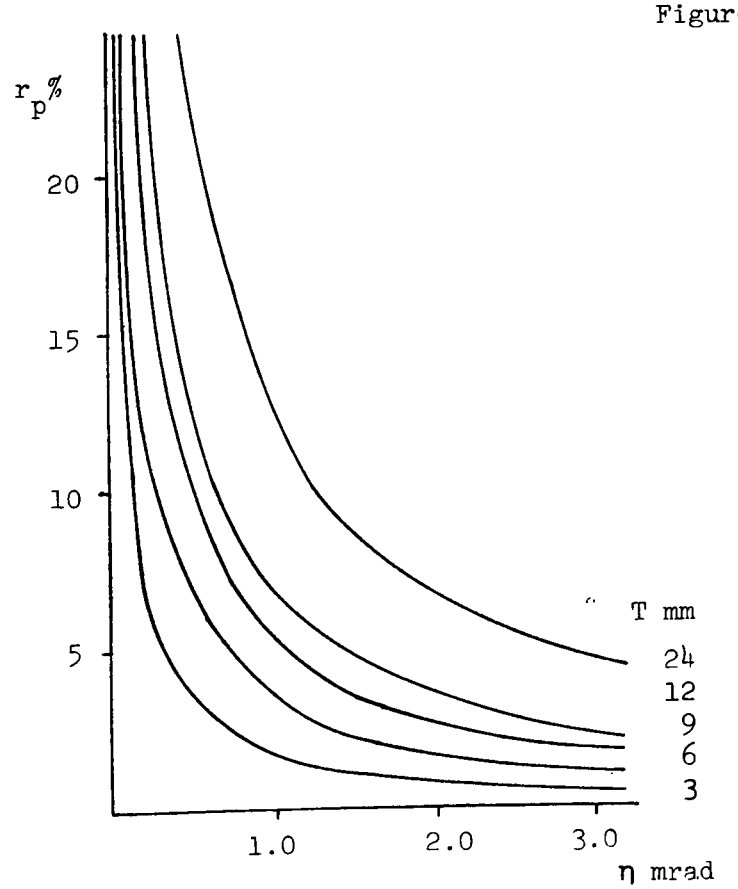


Figure 2.5 (left)

Figures 2.4 and 2.5.
These figures show the peak reflectivity as a function of mosaic spread for thicknesses of 3, 6, 9, 12 and 24mm, using the 220 reflection for γ-rays. They based on equation (2.21), including the effect of the absorption term $\exp(-\frac{\mu T}{\gamma})$ for figure 2.4 and excluding it in figure 2.5.

For the stronger 111 reflection the saturation point is reached at 11.58mm and a mosaicity of about 3.5 mrad, corresponding to a FWHM of 8 mrad.

The theoretical integrated reflectivities shown in figure 2.6 as functions of thickness for mosaic spreads were calculated from equation (2.15). The kinematical integrated reflectivity, $R_k$, is the linear function on each diagram. The thickness corresponding to the 'thin crystal' limit is at the point where the curves begin to deviate from the straight line.

From these figures (2.2 - 2.6) it is clear that there is no advantage to be gained in terms of increased reflectivity by increasing the crystal thickness beyond the saturation value for the reflection used. For gamma diffraction in copper using the three strongest reflections, the optimum thickness is about 12mm in deformed crystals.

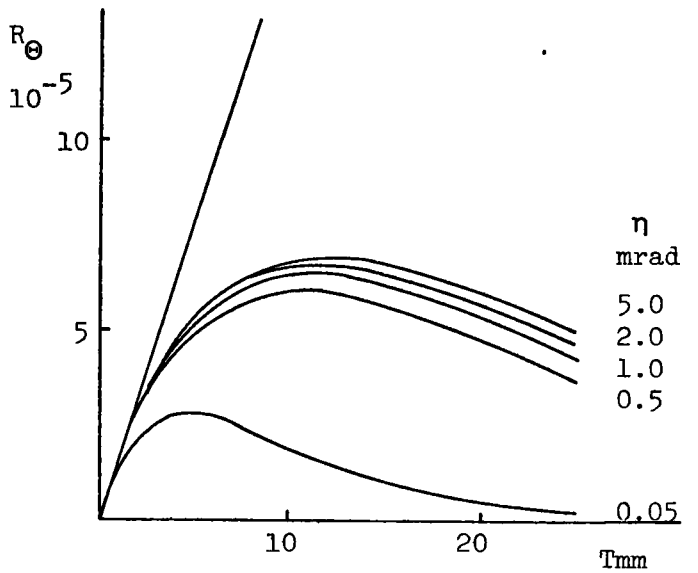


Figure 2.6a. γ-ray integrated reflectivities for the 220 reflection. calculated using equation(2.15). The straight line is $R_\Theta = QT$.

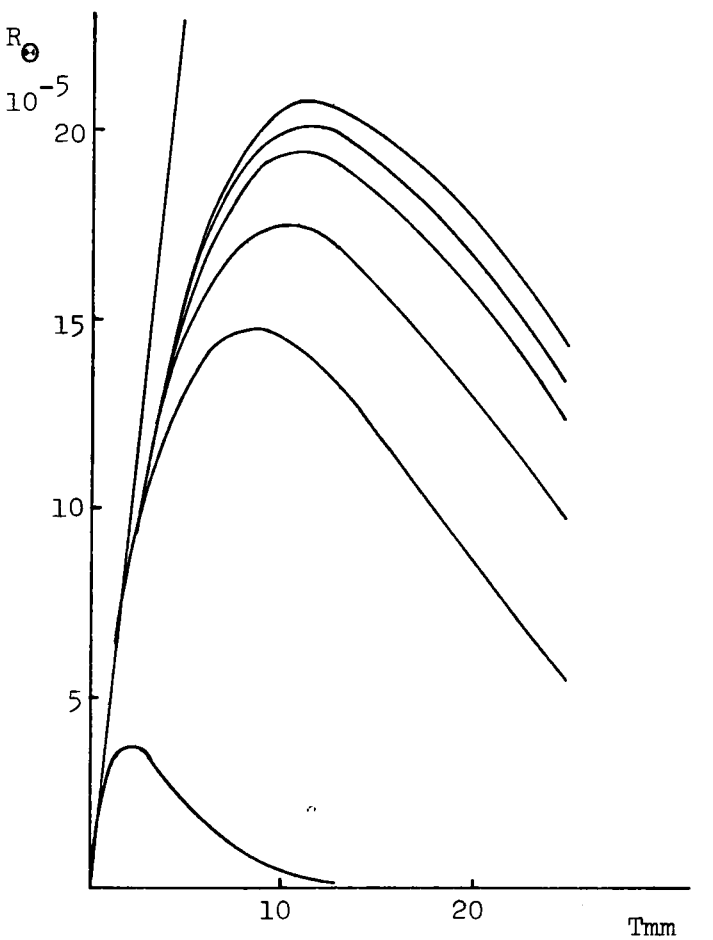


Figure 2.6b. Theoretical integrated reflectivities as a function of crystal thickness for various mosaic spreads using the 111 reflection, calculated with equations (2.15) and (2.10).

## 2·2 Neutron diffraction

Although the processes by which x-rays and neutrons are scattered are quite different, the same diffraction theory, with modifications, applies to both. In the x-ray case the incident radiation is scattered by interaction with the charged electron 'cloud' surrounding an atom, and the diffracted radiation is thus proportional to atomic number. The amplitude of the diffracted radiation, the atomic scattering or form factor, decays rapidly with increasing angle between incident and scattered directions because the dimensions of the electron 'cloud' are comparable to the x-ray wavelength. For neutron scattering it is the nucleus of the atom which interacts with the incident radiation, except for magnetic materials where electronic scattering is also appreciable. The neutron form factor, or scattering length $b_s$, shows no effective amplitude decay with increasing atomic number, and no variation with scattering angle $\Theta$, since the dimensions of the nucleus are small with respect to the incident wavelength. Also for neutrons there is no angularly dependent polarisation factor, which for x-rays depends on the incident electromagnetic vibration, again with the exception of magnetic materials in a magnetic field.

The values of linear absorption coefficients, or capture cross-sections, $\mu$, are typically of the order of a few units per millimetre for neutrons compared with tens of thousands of units per millimetre for x-rays. Thus a neutron beam passing through an ideally imperfect crystal at the Bragg reflecting position is attenuated mainly by diffraction, the attenuation by true (linear) absorption being very small. Zachariasen's general treatment of diffraction in mosaic crystals has been applied in the case of low absorption, e.g. neutron diffraction, by Bacon and Lowde[17] where the structure factor includes the scattering length $b_s$ instead of the x-ray form factor and the quantity Q no longer

contains the classical electron radius or the polarisation, i.e.

$$Q = \frac{\lambda^3 F^2}{V^2 \sin^2\Theta} \qquad 2.23$$

Rearranging equation (2.8) gives the theoretical reflectivity as a function of sample rotation angle $\omega$, which is the expression applicable to experimentally measured rocking curves.

$$r_{th}(\omega) = 0.5 \exp(-\frac{\mu T}{\gamma}) \; 1 - \exp(-\frac{2QTW(\omega)}{\gamma}) \qquad 2.24$$

2.2.1 The apparatus

The neutron experiments for this thesis were performed on a two-axis instrument with a cylindrical table on each axis connected by a steel tube which also supported the beam defining slits. The axis and beam defining slit separations could be varied up to 2m by translations along the steel arm, and the second axis could be rotated manually about the first. (figure 2.7). The cylindrical tables were mounted on air cushions on a high-precision-flat marble floor 2.4m x 2.4m, which was surrounded by 500 mm thick concrete shielding. The first table supported the goniometer mounting for the monochromator crystal and the second table held the goniometer for the sample to be studied. A beryllium trifluoride neutron counter was held by an arm free to rotate about the second axis, and the sample to counter distance was variable between 150 and 1000 mm. The $2\Theta$ monochromator angle could be selected between $10^\circ$ and $90^\circ$, which with suitable choice of crystal plane spacing gave a wavelength range of 0.6 to 2.5 Å. The only restriction on the counter angle was the direction of the monochromatic beam.

The rotation of monochromator and sample were controlled by step motor, as was the rotation of the counter about the sample. One motor step corresponded to 0.09 mrad, and the motor speed could be 9 mrad/s or 0.09 mrad/s. The data was recorded in the form of the number of counts registered per unit of time as a function of the rotation angle

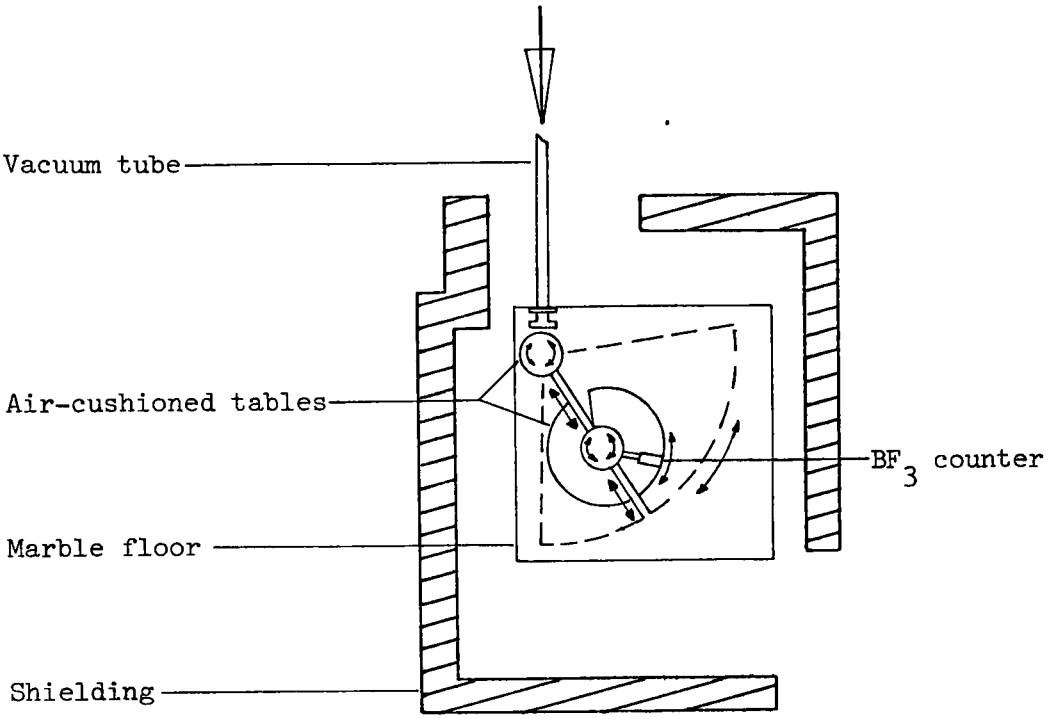


Figure 2.7a.

Plan of the neutron diffractometer.

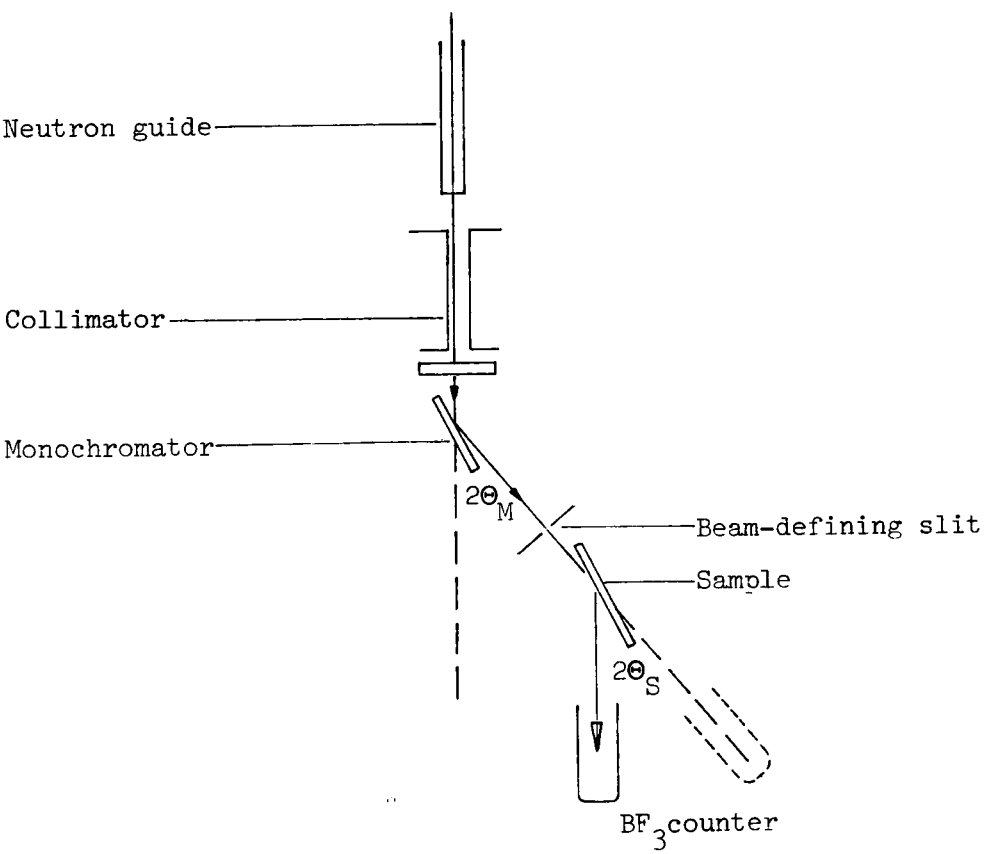


Figure 2.7b.

Sketch of the geometrical arrangement used.

of the sample, i.e. a rocking curve, and was displayed as a chart-recording and a printed list of counting time, counts, and step number. At the end of each counting period the sample crystal was automatically rotated through the required unit of angle.

The neutron flux from the reactor conforms to a Maxwellian distribution with maximum intensity at a wavelength of about 1.5Å, and a flux of about $5 \times 10^6$ neutrons/$mm^2$.s was obtained using a copper monochromator set for this wavelength.

2.2.2 Theoretical aspects of the experimental work

With the diffractometer just described it is possible to study the effect of varying wavelength as well as the crystal thickness and mosaicity. Examination of equations (2.23), (2.24) indicates that the wavelength dependence of the reflectivity is included in the factors $Q$ and $\gamma$, thus on substitution of the relevant values these equations are valid. The absorption coefficients, $\mu$, were obtained from an experimentally determined relationship between absorption and wavelength (Ch.5). The wavelengths and thicknesses used for the theoretical calculations are those corresponding to the experimental work. Figures 2.8a, b, c are for the 220 reflection showing the effect of increasing wavelength on the thickness dependence of the peak reflectivity for various mosaic spreads. With increasing wavelength the maximum reflectivity for a given thickness increases to a saturation value and reaches this value in progressively thinner crystals at higher wavelengths (fig. 2.8c). At a wavelength of 2Å there is no dependence on mosaicity, except for very thin (2mm) crystals, and the peak reflectivity is governed by the thickness of the crystal plate. For thicknesses up to about 10mm the peak reflectivity is strongly dependent on mosaicity as well as the linear dimensions, and both these effects are more critical than the variation

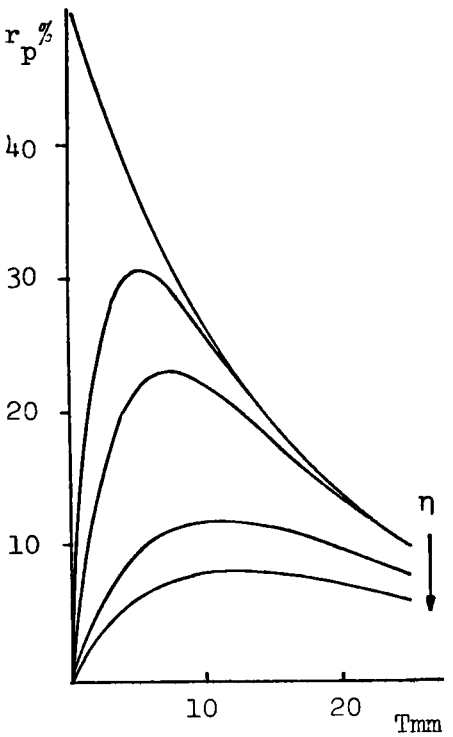


Figure 2.8a

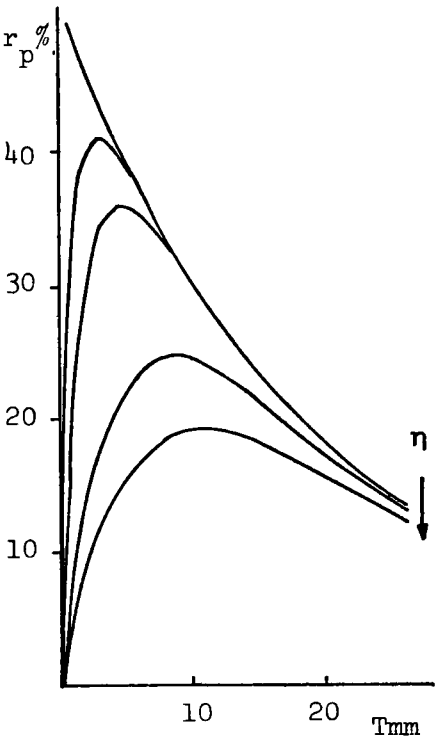


Figure 2.8b

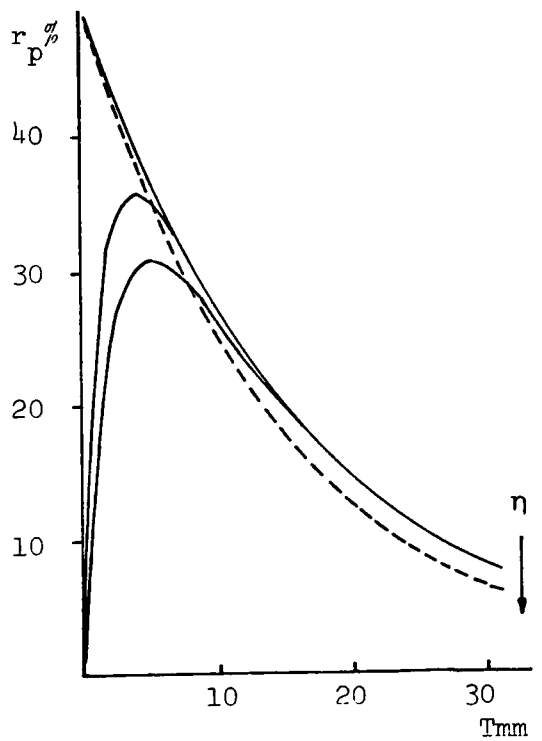


Figure 2.8c

Figure 2.8

These figures show the effect of increasing wavelength on the thickness dependence of the peak reflectivity for various mosaic spreads using the 220 reflection. The mosaic spreads increase in the sense of the arrows, and have the values of 0.05, 0.5, 1.0, 3.0 and 5.0 mrad. Figures 2.8a and 2.8b are for wavelengths of 0.683Å and 1.08Å respectively; the solid lines in figure 2.8c are for 1.69Å and the broken line is the saturation curve for 1.97Å. The curves were calculated using parameters relevant to neutron diffraction.

with wavelength. This can be seen in figure 2·10 which shows the variation of optimum thickness with mosaicity for the wavelength range 0·5 - 2·5Å according to equation (2·22).

Figures 2·8a, b, c, d show the dependence of peak reflectivity on mosaicity at various wavelengths, again indicating the strong dependence on mosaicity at shorter wavelengths. At longer wavelengths, with increasing thickness, the peak reflectivity is almost independent of mosaicity. The wavelength dependence of the peak reflectivity for various mosaic spreads at a crystal thickness of 6mm is given in figure 2·9 showing clearly the independence of mosaicity at wavelengths greater than 2Å. The form of the curves is similar for all thicknesses, the peak reflectivity being modified in each case according to equation (2·21).

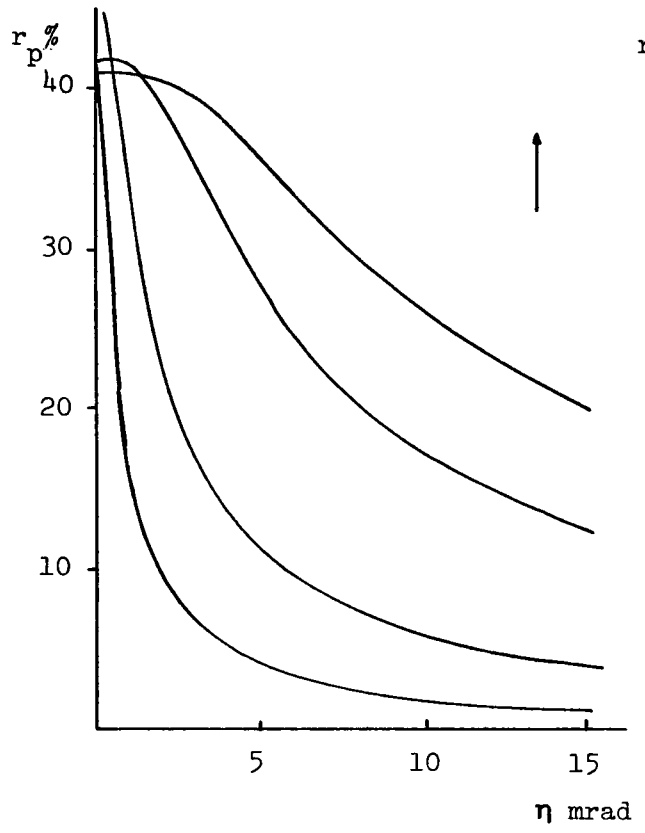


Figure 2.9a

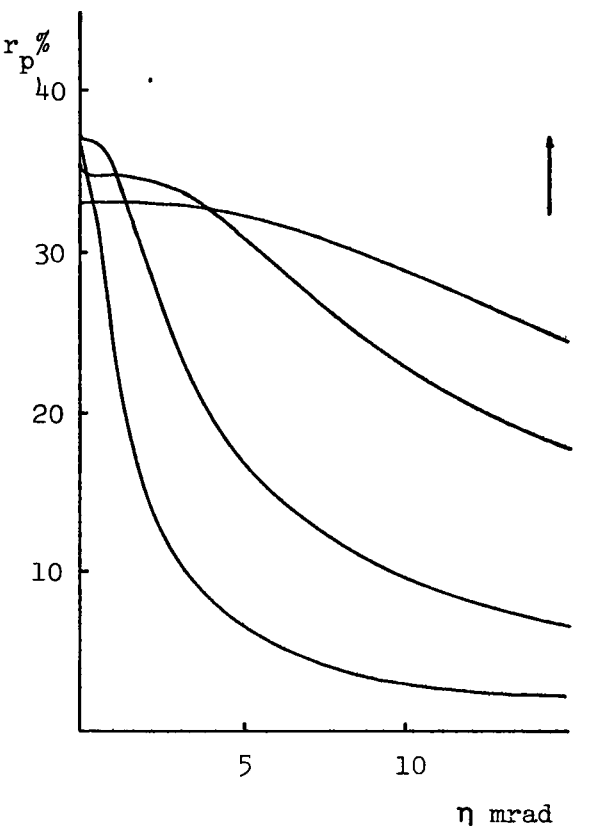


Figure 2.9b

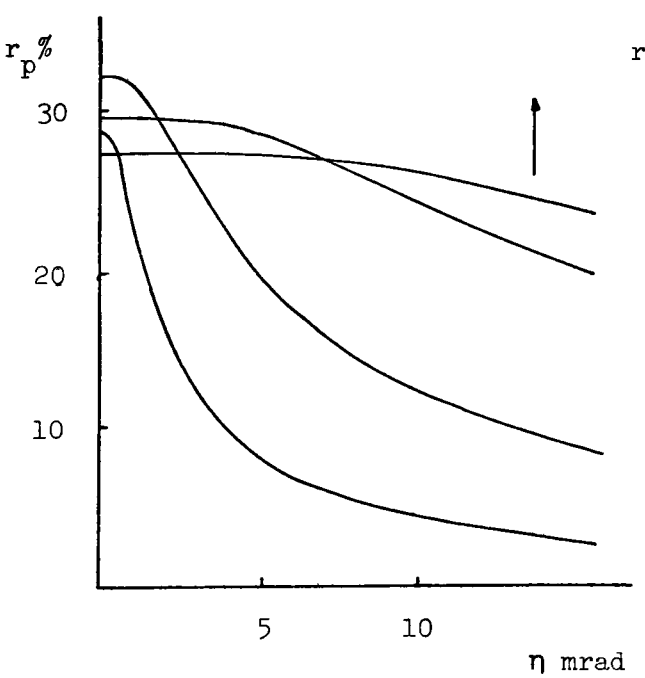


Figure 2.9c

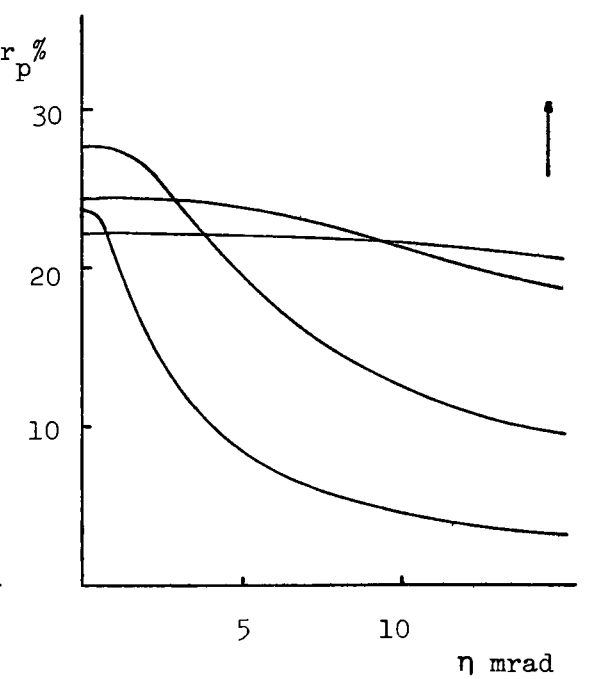


Figure 2.9d

Figures 2.9. The variation of peak reflectivity with mosaic spread for crystal thicknesses of 3, 6, 9, and 12mm at wavelengths of (a) 0.683Å, (b) 1.08Å, (c) 1.69Å and (d) 1.97Å. All are for a 220 neutron reflection. The thickness increases in the sense of the arrows.

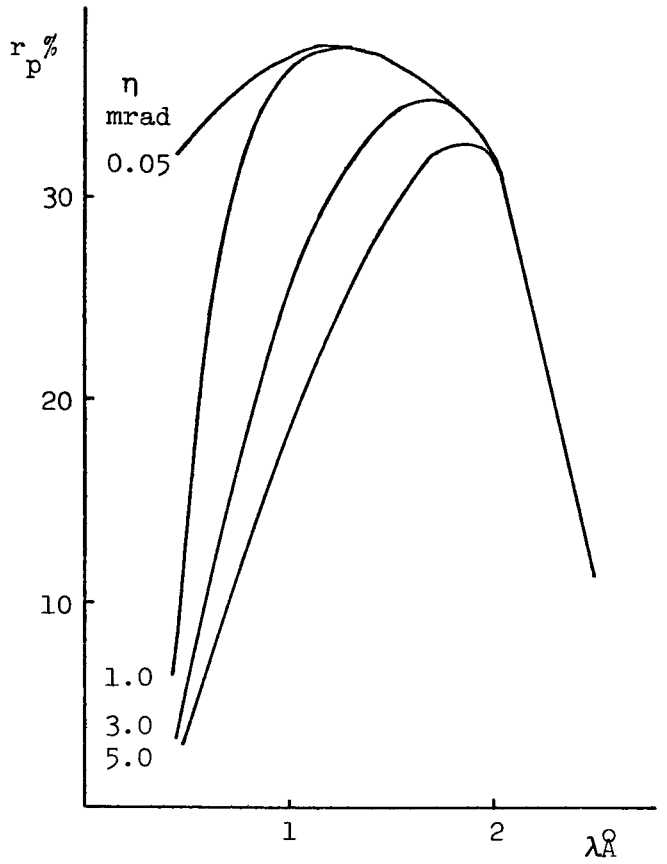


Figure 2.10

Figure 2.10 (left)
The wavelength dependence of the peak reflectivity for various mosaic spreads in a 6mm thick crystal, calculated for a 220 reflection with neutron radiation.

Figure 2.11 (below)
The variation of optimum thickness with mosaic spread for different neutron wavelengths using a 220 reflection.

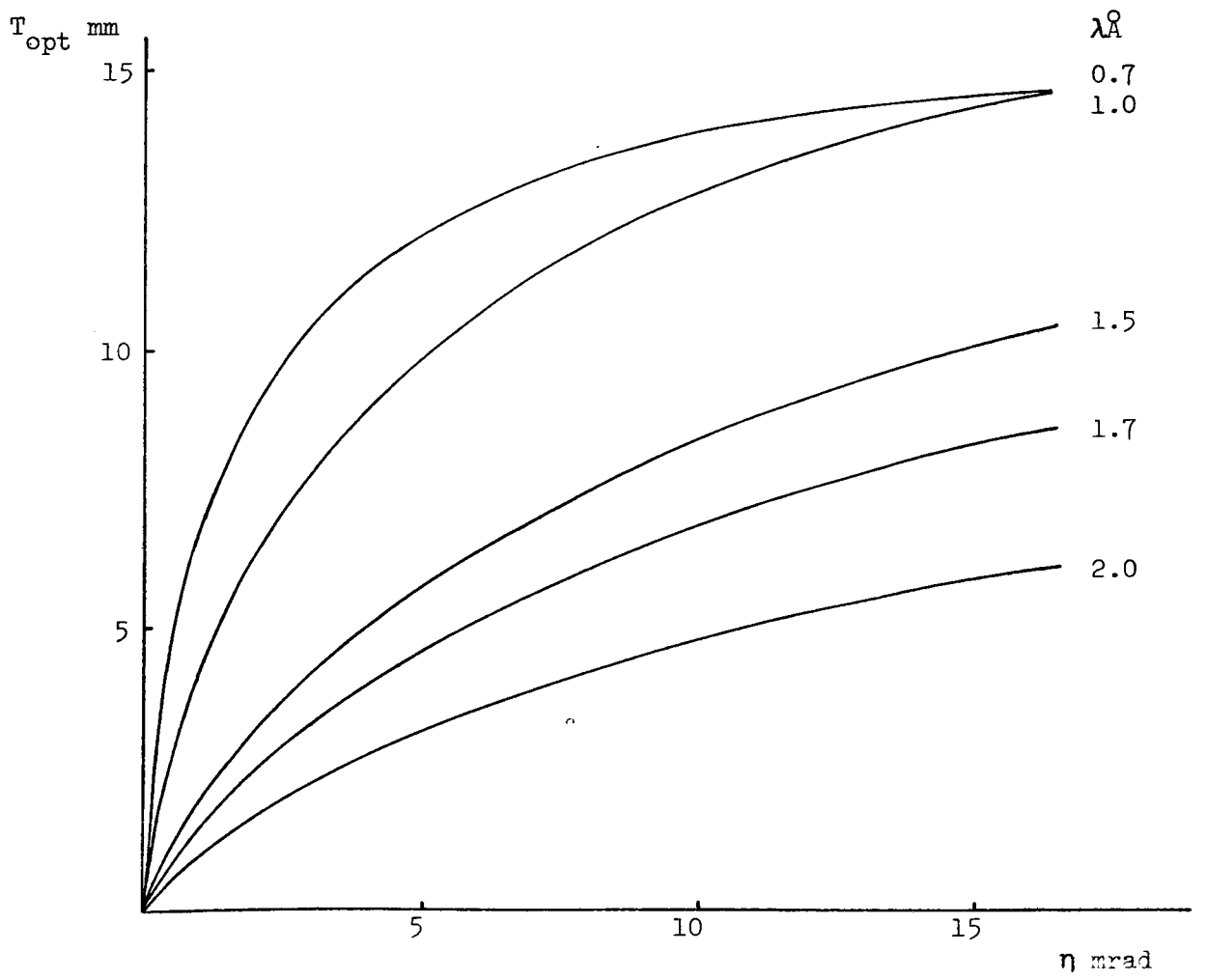


Figure 2.11

## 2·3 Electron diffraction

The basic transmission electron microscope consists of an electron source and an assembly of magnetic lenses arranged in a vertical column which is evacuated to $10^{-5}$ torr or better. The source produces a coherent parallel beam of electrons which can be varied in diameter from 1μm to 50μm at the specimen surface. Electrons passing through the thin specimen are brought to focus in the back focal plane of the objective lens, which is a converging lens, and form a diffraction pattern in this plane. An inverted image is formed in the first image plane and subsequent lenses are used to magnify either this image or the diffraction pattern. Virtually all analyses of crystal defects are carried out by inserting an aperture in or near the back focal plane to ensure that only one beam contributes to the formation of the electron image. If the direct beam is selected a bright field image is formed, whereas a dark field image is obtained by selecting a diffracted beam. Selected area diffraction, (SAD), is when an aperture is inserted at the first image plane so that the area of the specimen giving rise to the imaged diffraction pattern in the back focal plane is defined.

A diffraction pattern consists of a series of well-defined maxima, or diffraction spots, indicating that several sets of planes are at or nearly at their appropriate Bragg angles for diffraction. In the interpretation of contrast from crystal defects it is usual to arrange for only one set of crystal planes to be diffracting strongly, the so-called two-beam conditions. The solution of the diffraction pattern yields the indices of the plane giving rise to a diffraction spot and its precise deviation from the Bragg angle, as well as the electron beam direction, $\underline{B}$, defined as making an acute angle to the downward normal to the specimen, $\underline{N}$.

The electron image is a highly magnified image of the variation in

intensity of the selected beam across the bottom surface of the crystal. Contrast in bright field, (bf), arises if the intensity of the direct beam varies significantly from one region of the specimen to another, and corresponding variations are usually obtained in the dark field,(df), image. The two-beam dynamical theory of image contrast, as developed by Howie and Whelan[24], takes account of the rediffraction between the direct and diffracted beams with coupled equations for the variation with depth of the diffracted and transmitted amplitudes. The contrast from imperfect crystals is considered by introducing an extra phase factor $2\pi \underline{g}.\underline{D}$, where $\underline{D}$ is the displacement of a unit cell from its lattice position in perfect crystal. A convenient form of the equation is

$$\frac{d\Phi_o}{dz} = \left(-\frac{\pi\Phi_o}{\xi'_o}\right) + \pi\left(i/\xi_g\right) - \left(1/\xi'_g\right)\Phi_g \qquad 2.25a$$

$$\frac{d\Phi_g}{dz} = \pi\left(i/\xi_g\right) - \left(1/\xi'_g\right)\Phi_o + \left(-\frac{\pi}{\xi'_o}\right) + 2\pi i\left(S_g + \underline{g}.\frac{d\underline{D}}{dz}\right)\Phi_g. \qquad 2.25b$$

$\xi_o$, $\xi_g$ are complex (') quantities with dimensions of length, corresponding to the extinction length in section 2.1.2, and values for copper of a few hundred angstroms. $\Phi_o$, $\Phi_g$ are amplitudes of the direct and diffracted beams, where $\underline{g}$ is the operative reflection. A measure of the deviation from the exact Bragg angle is given by $s_g$, and z is the depth within the crystal. The displacement term $\left(\underline{g}.\frac{d\underline{D}}{dz}\right)$ locally changes the effective value of $s_g$ and the observed contrast depends on both terms. When $\left(\underline{g}.\frac{d\underline{D}}{dz}\right)$ is zero a defect will be invisible, and when $s_g$ is large, large values of $\left(\underline{g}.\frac{d\underline{D}}{dz}\right)$ will be necessary for any contrast to be observed. $\frac{d\underline{D}}{dz}$ is the variation of displacement with depth and equivalent to a local tilting of the reflecting planes.

Planar defects, e.g. stacking faults, represent a discontinuity rather than a continuous displacement and the term $\frac{d\underline{D}}{dz}$ is replaced by

a vector $\underline{D}$. The contrast from a planar defect inclined to the foil surface takes the form of dark and light fringes, the symmetry characteristics of which depend on the phase angle $2\pi\underline{g}.\underline{D}$. Under two beam conditions a defect will be invisible when

$$2\pi\underline{g}.\underline{D} = 0, 2n\pi \qquad 2.26$$

where n is an integer. In f.c.c. crystals stacking faults lie on {111} and can be described by the displacement vector $\frac{1}{3}<111>$. The only distinct values of $\underline{g}.\underline{D}$ are 0 and $\pm\frac{1}{3}$.

For a dislocation with Burgers vector $\underline{b}$, the condition for invisibility is

$$\underline{g}.\underline{b} = 0 \qquad 2.27a$$

for a screw dislocation, and for an edge dislocation

$$\underline{g}.\underline{b} = 0$$

and

$$\underline{g}.(\underline{b}\times\underline{u}) = 0 \qquad 2.27b$$

where u is a unit vector along the dislocation line. In f.c.c. crystals perfect dislocations have Burgers vectors equal to a lattice translation vector, i.e. $\frac{1}{2}<110>$, and for such vectors the only possible values for $\underline{g}.\underline{b}$ are integers or zero.

Partial dislocations have Burgers vectors of type $\frac{1}{6}<112>$ or $\frac{1}{3}<111>$ and visibility depends on the magnitude of $s_g$ as well as $\underline{g}.\underline{b}$.

## 3. Gamma diffraction

This chapter covers all treatments received by the crystals in preparation for the diffraction measurements as well as the experimental details and results. The crystals have been divided into two groups according to shape; i.e. flat plates and rectangular blocks. All the crystals used were 99·998% pure copper single crystals grown by Cristaltech of Grenoble using the Bridgeman technique. The crystals were seeded <111> and had approximate heights and diameters of 100mm. All crystallographic directions are defined with respect to the orientations of the samples immediately prior to deformation.

### 3.1 Flat plate crystals

Two flat parallel faced single crystals, PP3 and PP4, with approximately elliptical surface areas of 4000mm$^2$ and thicknesses of 13mm were spark-machined from two of the above-mentioned crystals, as shown in fig. 3.1. The face normals were [011] and the long axes [100]. The surface damage caused by the machining, estimated at about 0·5mm, was chemically removed in 75% nitric acid with 25% distilled water. Gamma-ray rocking curves were recorded at regular intervals throughout the crystal before and during sample preparation to determine the 'state' of the crystal structure. Well-defined, smoothly varying single peaks indicate a uniform mosaic structure, whereas irregular shaped peaks suggest an inhomogeneous deformation. The crystals were then deformed in compression along [011] to various degrees, with periodic interruptions to record γ-ray rocking curves monitoring the deformation. PP3 was halved longitudinally and one half received an additional deformation. The details of the deformations are given in figure 3.2, where the degree of deformation

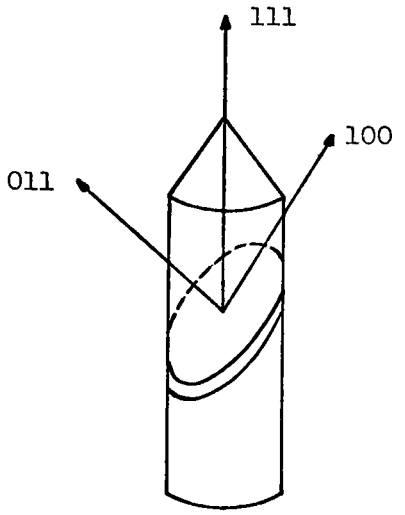


Figure 3.1a
Sketch showing the orientation of a flat plate crystal with respect to an as-grown crystal.

Figure 3.1b
Plan view (i) and elevation (ii) of the two halves of PP3, and the elevation (iii) after cutting into step configuration.

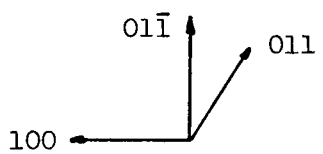


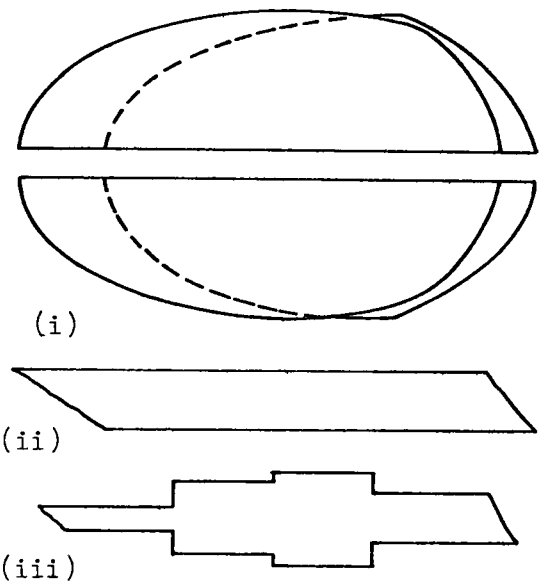


| | | | | | |
|---|---|---|---|---|---|
| Tmm | 3.0 | 8.9 | 11.8 | 5.9 | PP3II |
| Tmm | 2.5 | 8.5 | 11.4 | 5.4 | PP3I |

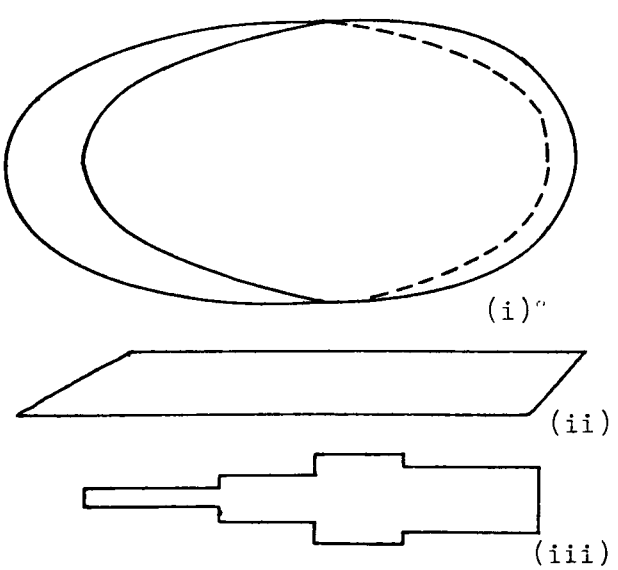


| | | | | |
|---|---|---|---|---|
| Tmm | 2.5 | 5.5 | 11.2 | 8.7 |

Figure 3.1c
Plan (i) and elevation (ii) of plate PP4, and elevation (iii) after cutting into step configuration.

is expressed as the average FWHM of all the rocking curves recorded for a given applied load.

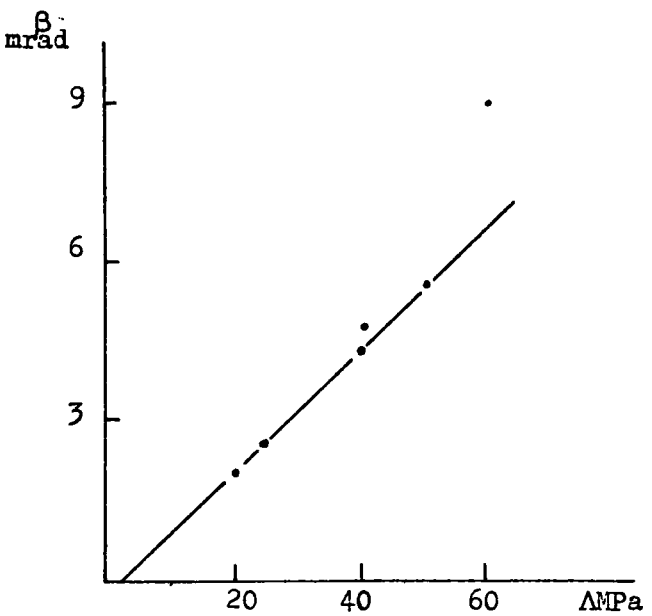


| Δ MPa | β mrad | crystal |
|---|---|---|
| 20.1 | 1.98 | |
| 24.5 | 2.47 | PP3I |
| 39.2 | 4.25 | PP3I |
| 40.1 | 4.62 | |
| 49.0 | 5.35 | |
| 59.1 | 8.96 | PP4 |

Figure 3.2

Measured FWHM's as a function of applied load for crystals PP4, PP3I and PP3II. The final loads for each crystal are indicated in the column on the right of the table giving the values for the figure.

After the final loading the plates were spark-machined into a step configuration with thicknesses, T, of approximately 3, 6, 9 and 12mm as shown in figure 3.1. Surface damage was removed chemically as before.

3.1.1 Crystal PP4

The deformation was monitored by 'mapping' the crystal with a series of rocking curves, using the 200 reflection, at translational intervals of 15mm throughout the crystal. The beam had a cross-section of 10x1mm$^2$ corresponding to an angular divergence in the scattering plane of 0·145 mrad. All measurements were under the same experimental conditions unless stated otherwise. The crystal

volumes shown in figure 3.3 were measured after each loading to 'map' the deformation of the crystal. The general trend with increasing deformation was for the peak intensities to decrease and the angular spread to increase. Double peaks, for a single reflection, appeared with the first loading, and with subsequent loading the peak separation remained unchanged while the peaks broadened and reduced in height until a very broad single peak was formed. The map following the final deformation of PP4 is shown in figure 3.4. The scale of the vertical axes is in arbitrary units of intensity and the diffraction patterns are referred to the same angular origin on the horizontal axis, which is the angle through which the crystal was rotated.

These measurements were repeated on the same volume elements after the crystal had been cut into step configuration, and also at 3mm intervals along a central band passing through points 4 to 9 using the 200 reflection. Curves from the latter measurements, corresponding to elements 5 to 9, are included in figure 3.5 showing the variation in form through the thickness of the crystal. The intensity scales of the two sets of curves in figures 3.4 and 3.5 are different, as are the angular scales. Figure 3.6 shows the variation in half-width and angular position of the peaks with respect to the translational position in the crystal, where the FWHM was taken to include the peak separation for double peaks rather than the sum of the half-widths of each peak. The angular position of the maximum intensity changed with volume element and a plot of this angular position from each profile against translational position did not indicate a uniform bending of crystal planes. The centre of gravity of a peak gives a more accurate estimate of the exact Bragg position than the peak maximum where profiles are broad with multiple peaks. This value is given as a horizontal bar on each of the half-widths shown in fig. 3.6b, and oscillates about a

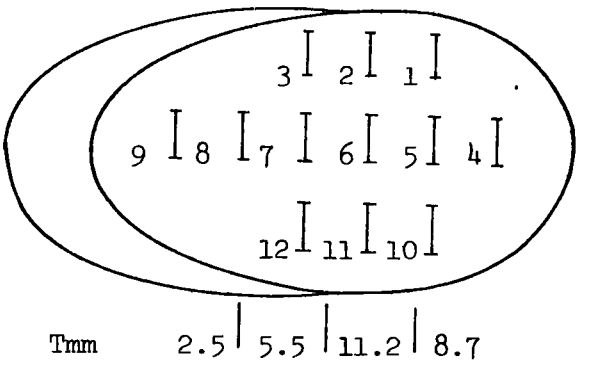


Figure 3.3

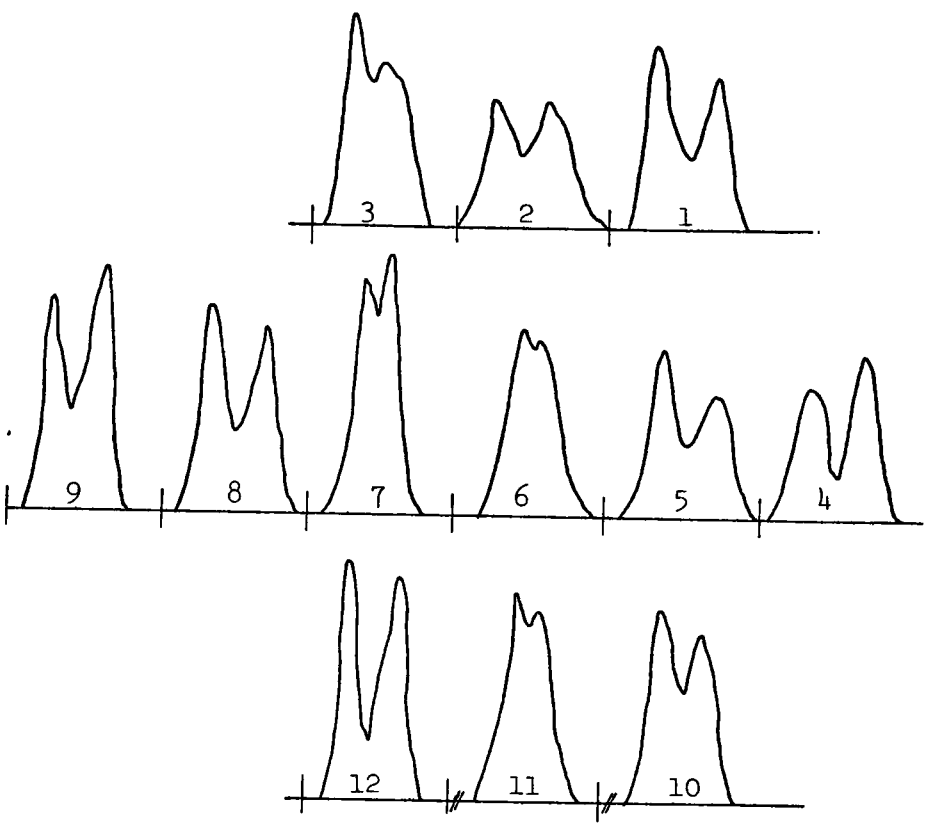


Figure 3.4. The form of the diffraction profiles measured in the volumes shown in figure 3.3 for crystal PP4, using the 200 reflection to compose a 'map'. The angular origin is marked by a vertical line to the left of each peak.

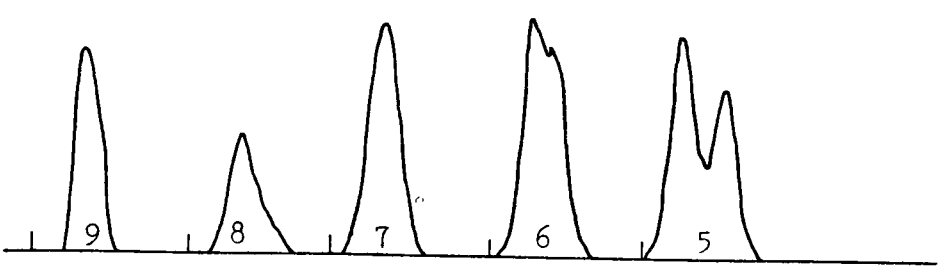


Figure 3.5. Diffraction profiles recorded in volume elements 5 to 9, after the crystal had been cut to step configuration, under the same conditions as the measurements for figure 3.4.

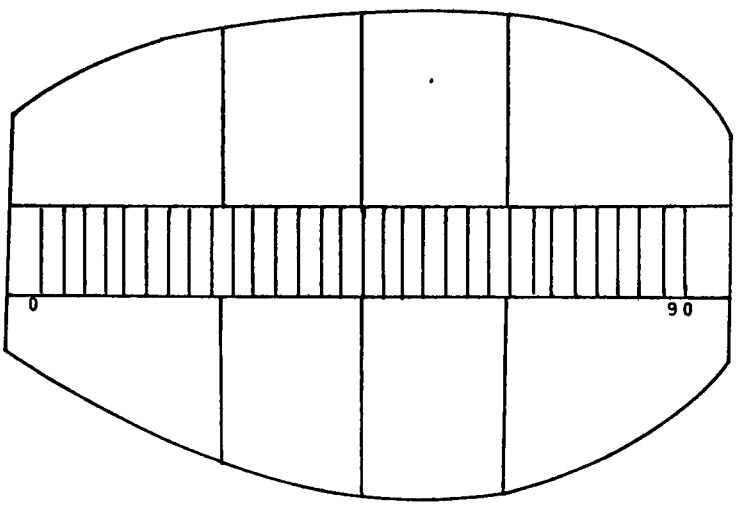


Figure 3.6a

| Tmm | 2.5 | 5.5 | 11.2 | 8.7 |
|---|---|---|---|---|

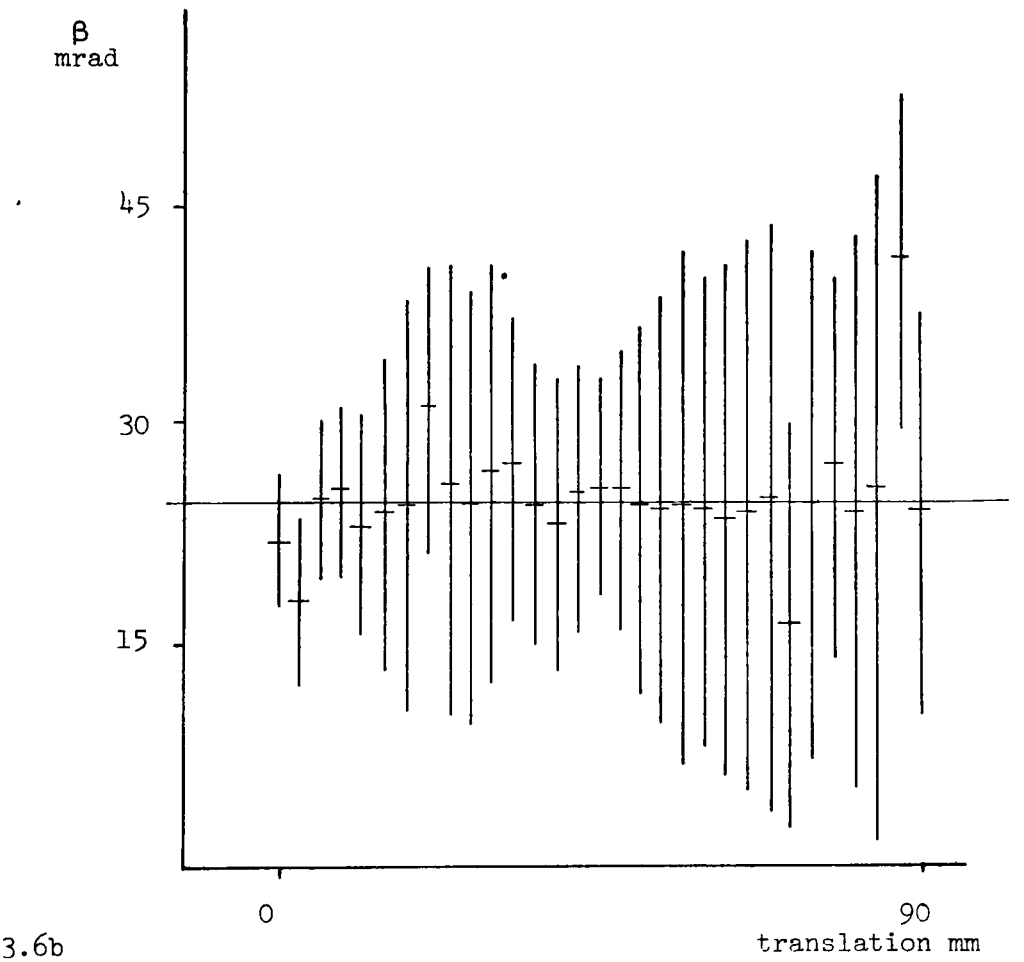


Figure 3.6b

This shows half-widths as a function of translational and angular position measured at 3mm intervals in the volumes of PP4 shown in figure 3.6a, using the 200 reflection. The curves are referred to the same, arbitrary angular origin and the position of the centre of gravity of each peak is shown by a short horizontal bar. The average value, corresponding to the Bragg angle $\theta_B$, is given by the continuous horizontal line.

mean value which is shown as a continuous line across the diagram. The average deviation of the centre of gravity from this mean value was about 4mrad.

Only the curves measured in the thicker (8.7, 11.2mm) regions registered double peaks, and the peak separations increased in going from the centre to the edge of the plate. The profiles for the 8.7mm region were broader than those for the 11.2 mm region, and this effect was observed in the same regions of the flat plate crystal before it was cut into step configuration. In the thinner regions of the crystal, smoothly varying single peaks were recorded, in which the peak heights and widths reduced with decreasing thickness while the form remained about the same. This indicated a more uniform structure.

A mapping was also performed with the $0\bar{2}2$ reflection after the crystal had been cut to step configuration. The results showed uniform single peaks for all thicknesses, with integrated intensities decreasing as the thickness decreased. However, the difference between the curves for the 8.7mm and the 11.2mm regions was very small. Further sets of γ-ray rocking curves were recorded in the regions of PP4 used for neutron diffraction measurements and these are reported in section 5.2. The curves from the mapping with the $0\bar{2}2$ reflection were narrower and more intense than those of the same reflection used with the neutron experiments.

### 3.1.2 Crystal PP3

The deformation was monitored as for crystal PP4 with the 200 reflection in the crystal volumes shown in figure 3.7. The results indicated a similar structure to PP4, with single peaks recorded for positions 2, 6 and 11, and double peaks for the other volume elements. Rocking curves for elements 1 and 5 were similar in size and shape, as

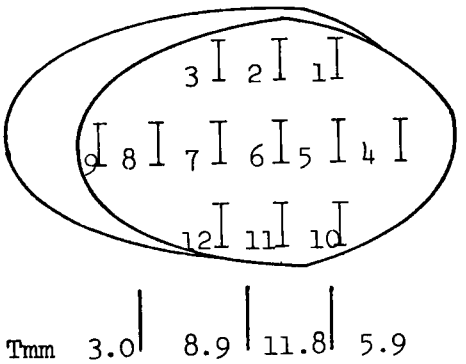


Figure 3.7a

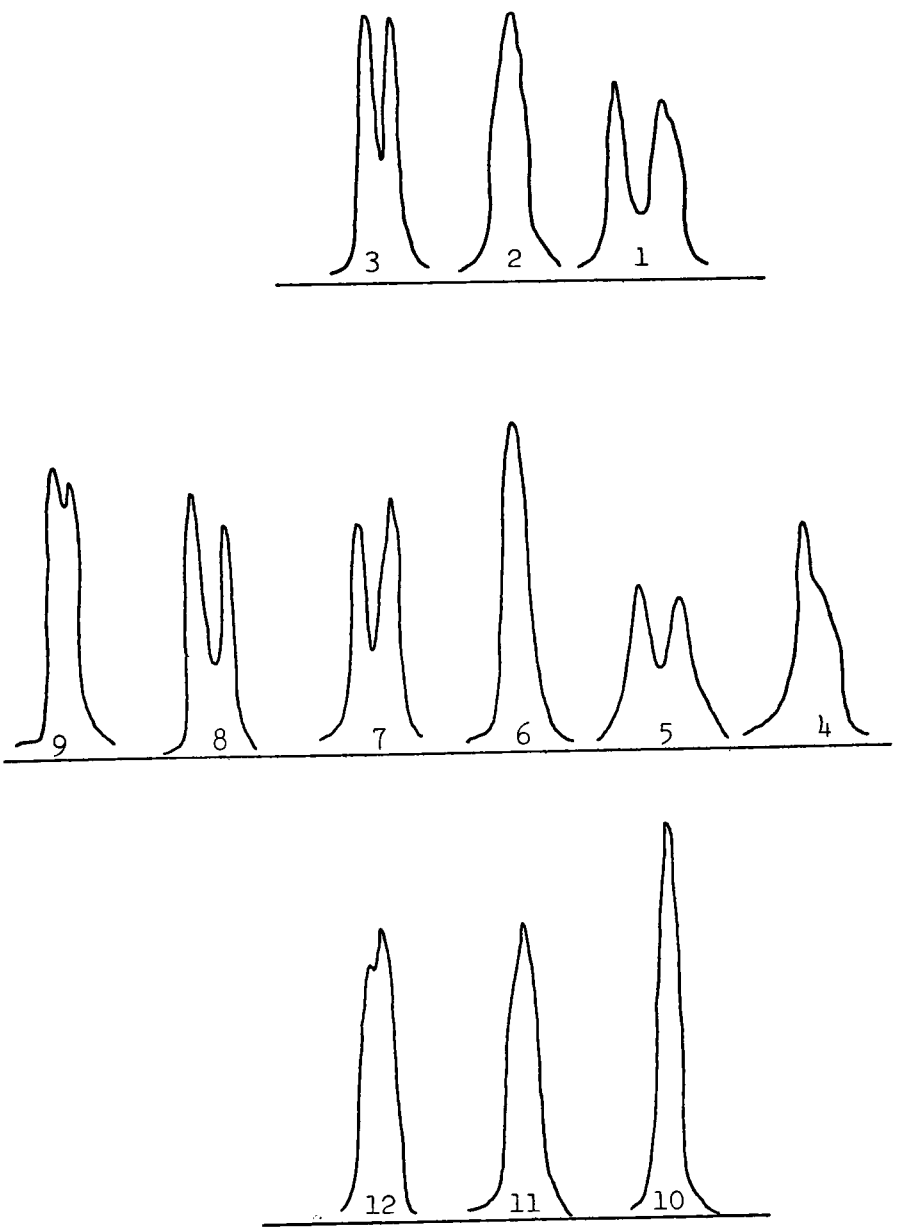


Figure 3.7b

A map of crystal PP3 using the 200 reflection following an applied load of 20.1MPa. The peaks correspond to the positions shown in figure 3.7a and were recorded in the uncut crystal plate.

were those for elements 3 and 7. There was virtually no difference in the profiles recorded after the first and second deformations, for which the difference in applied load was only 4MPa. The profiles recorded in PP3II after the final deformation were not much broader or less intense than those for PP3I, but this depended on the orientation of the crystals with respect to the scattering vector. For the flat plate crystals the half-widths of the measured profiles are approximately linearly related to the applied load, up to loads of 50MPa, (fig.3.2).

When the crystals had been cut into the step configuration of fig. 3.1b, rocking curves were recorded for the volume elements shown in figure 3.8, using the reflections $0\bar{2}2$, $1\bar{1}1$ and 200. For the 200 reflection in crystal PP3II, the measurements were repeated in the same volume elements after an arbitrary rotation about the scattering vector $\underline{g}$. The parameters obtained from all these measurements are listed in tables 3.3 to 3.6 (Appendix). Where double peaks were widely separated two values of $r_p$ and $\beta$ are given, one for each peak.

For the $0\bar{2}2$ reflection in PP3I the peaks in the 11.4mm region were broad single peaks. In the 8.5mm region all but two were smooth single peaks and these two were contaminated by edge effects. In the thinner regions the recorded curves were uniform single peaks, narrower than those for the thicker regions. Figure 3.9a and b shows some of the curves recorded with this reflection in PP3I in positions shown in fig. 3.8d. With the same reflection in PP3II, the peaks, although single, were of irregular shape with a suggestion of the formation of double peaks in all thicknesses.

The curves recorded using the $1\bar{1}1$ reflection were smoothly varying single peaks in the thickest and thinnest regions, and showed double or multiple peaks in the intermediate thicknesses. The peaks recorded in PP3I with this reflection are shown in figure 3.10 as a function

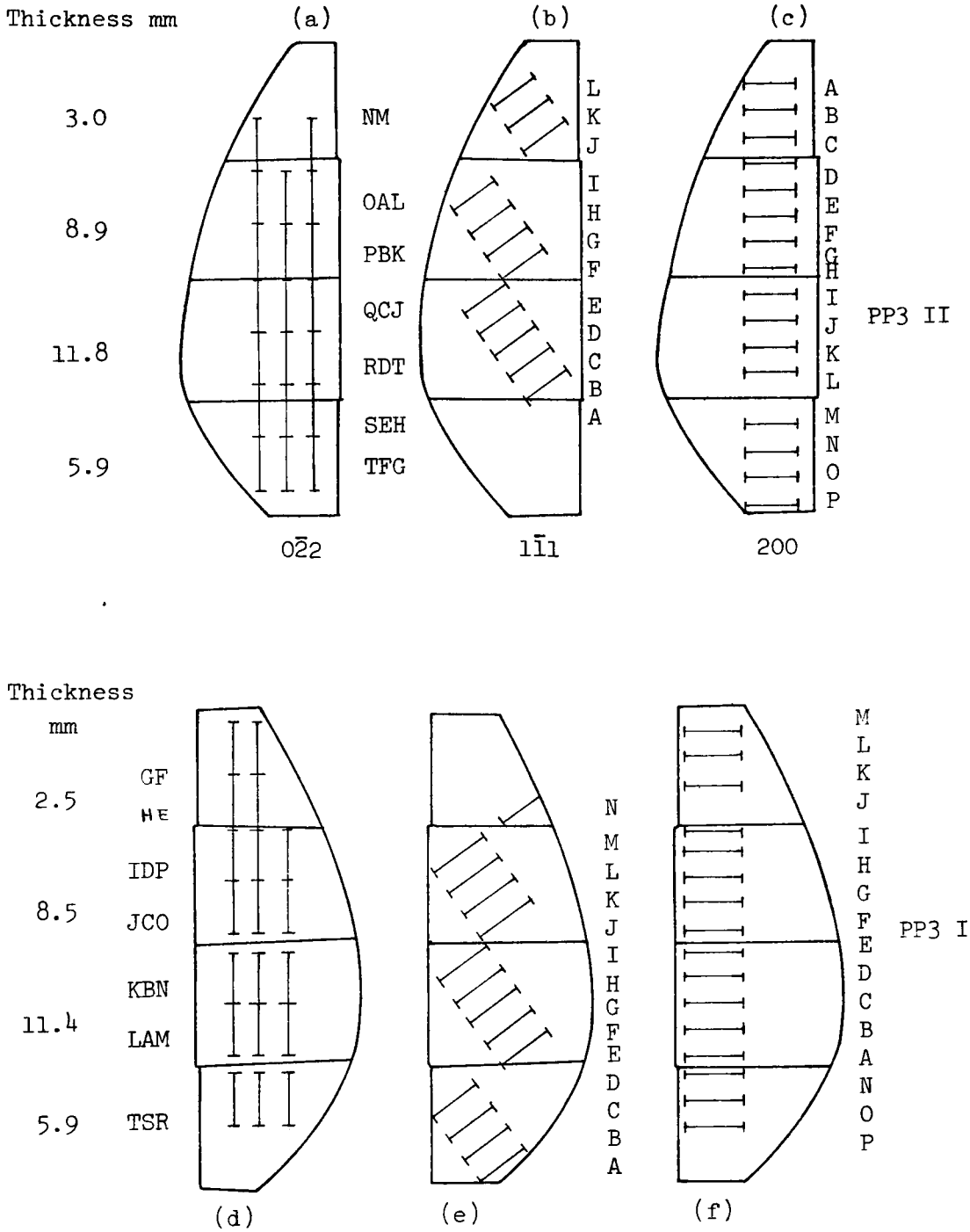


Figure 3.8

The volume elements used to map crystals PP3I and PP3II with the reflections 0$\bar{2}$2, 1$\bar{1}$1 and 200.

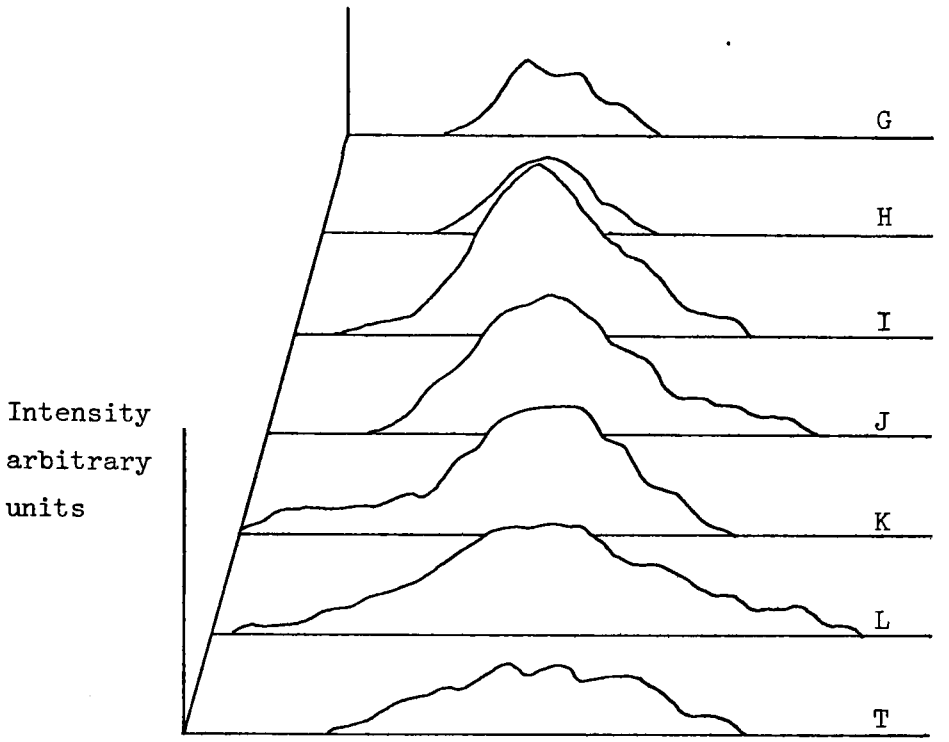


Figure 3.9a

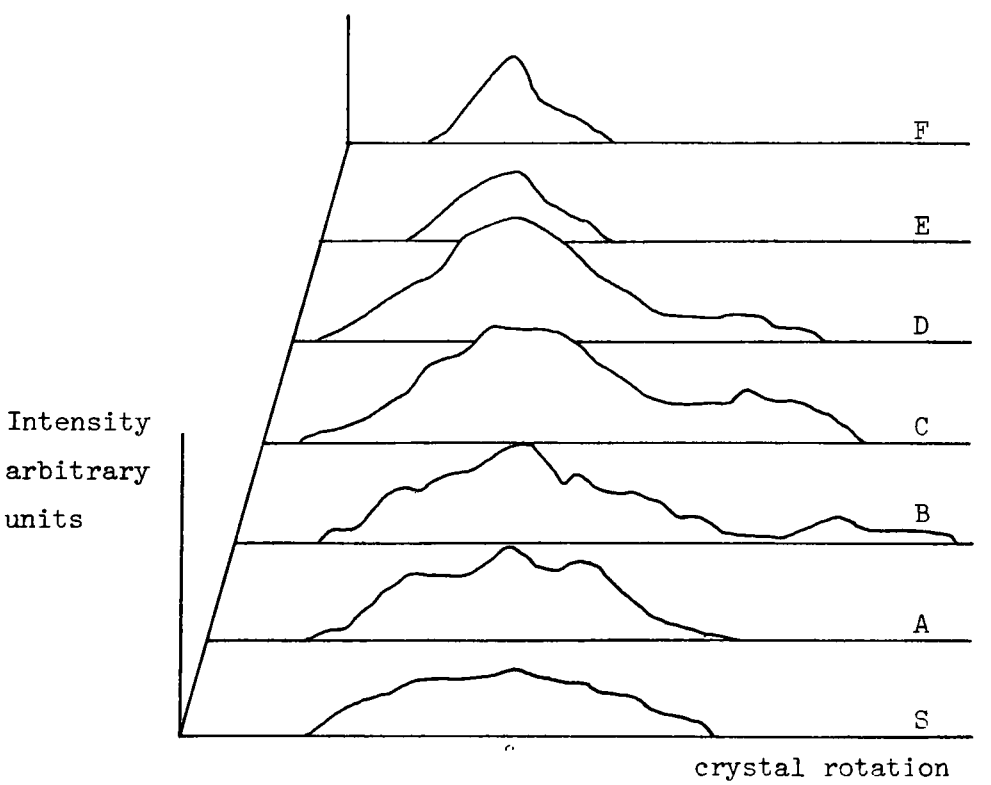


Figure 3.9b

These two figures represent rocking curves recorded in two adjacent rows in crystal PP3I using the reflection $0\bar{2}2$. The lettered positions correspond to those given in figure 3.8d.

of translational position in the crystal.

Figure 3.11 gives curves for the 200 reflection in PP3I, not to the same scale as the previous figures. Very broad single peaks were recorded in the 11.4mm region, and the peaks in the 2.5mm region were uneven single peaks. Double peaks were recorded in the remainder of the crystal. Similar shape curves were recorded in PP3II with the same reflection. The curves recorded in this crystal with the 200 reflection at two slightly different incident beam directions are given in figures 3.12 and 13, which are to the same scale. The measured parameters corresponding to these figures are in tables 3.6 a and b. From these it can be seen that the peak height, width and separation, in the case of double peaks, vary with such a rotation. The absolute angular position was not the same in both cases so it was not possible to determine any angular variation of the centre of gravities with incident direction, which was not far from [011] for all measurements.

## 3.2 Rectangular block crystals

A large rectangular block was machined from one large single crystal, and sectioned to give four equivalent rectangular blocks of dimensions 24 x 24 x 54 $mm^3$, each with long axis $[\bar{1}11]$ and faces (110) and $(1\bar{1}2)$. The blocks were finished simultaneously by mounting them in low-temperature-setting resin in a steel cylinder with a close-fitting piston which could be adjusted to expose the end faces of the crystals. The faces were then spark-planed and polished with silicon carbide suspensions and diamond pastes down to 1μm before the crystals were reversed and the opposing faces planed and polished. The end faces were parallel to within ~2mrad, and the long axes were within 25mrad of $[\bar{1}11]$. The crystals were mapped with γ-ray rocking curves

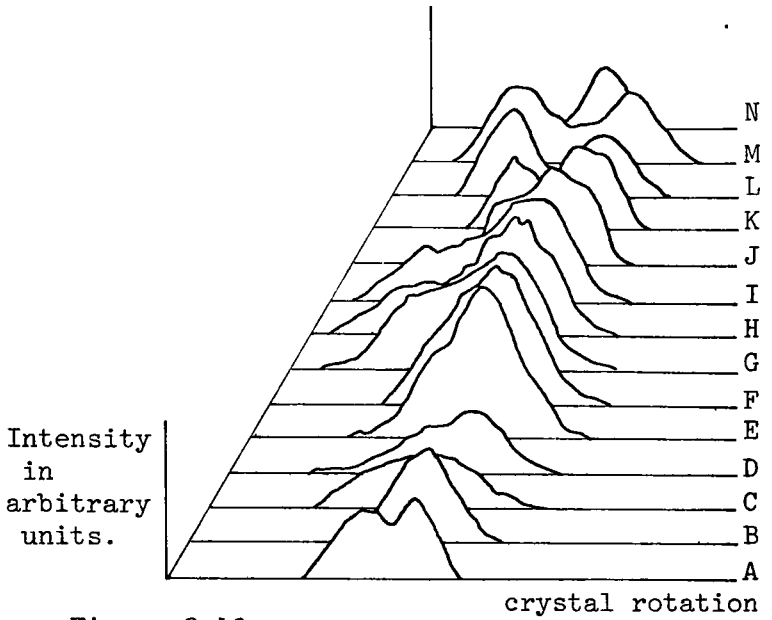


Figure 3.10

The rocking curves shown here were recorded using the $\bar{1}11$ reflection in the positions of figure 3.8e, in crystal PP3I.

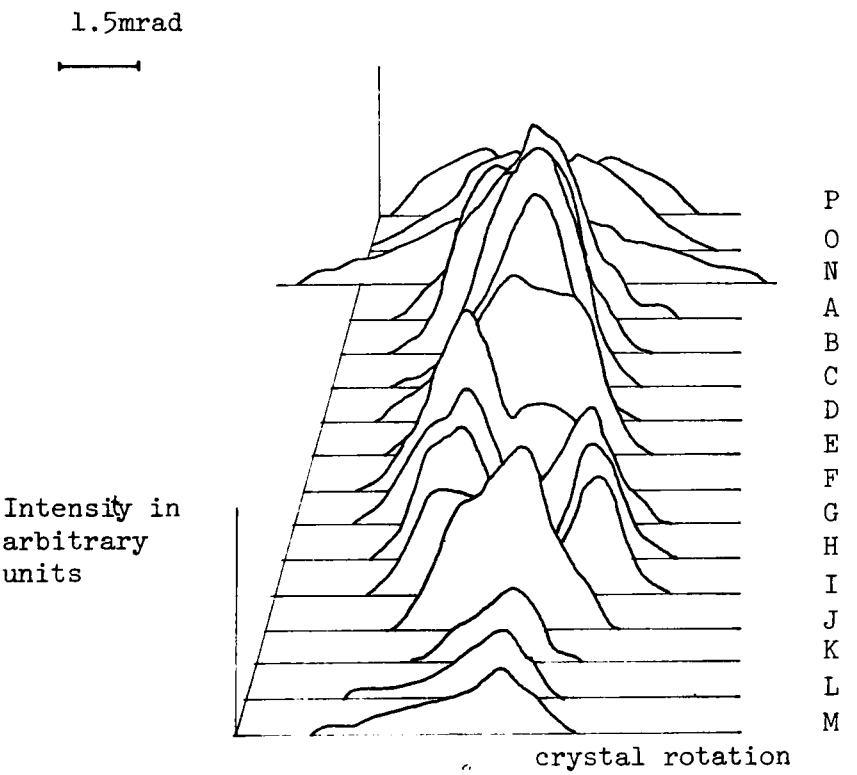


Figure 3.11

γ-ray rocking curves recorded in crystal PP3I using the 200 reflection in the positions shown in figure 3.8f. They are to the same scale as figure 3.10.

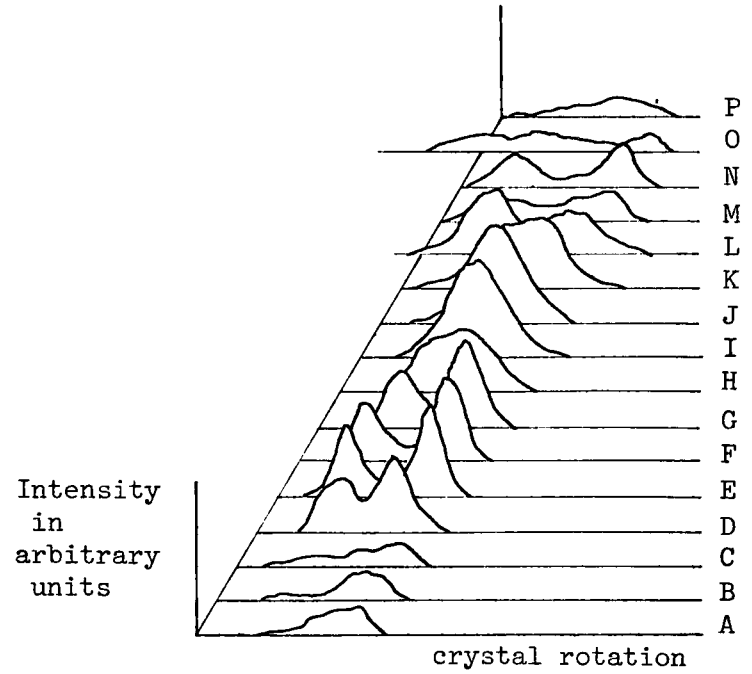


Figure 3.12

The variation in peak shape with translational position in crystal PP3II. The peaks are all referred to the same angular origin, and are for the 200 reflection.

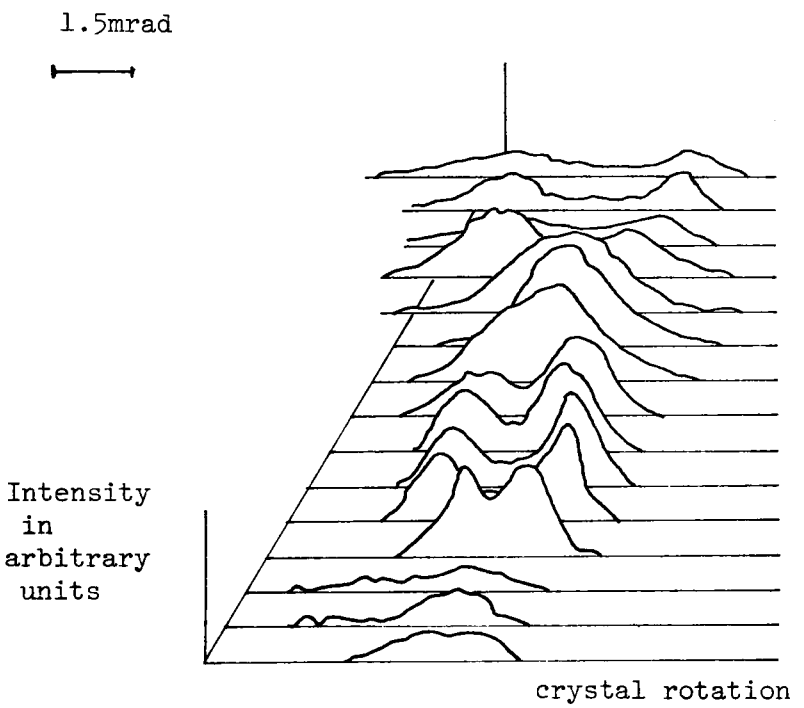


Figure 3.13

These peaks were recorded in the same positions and with the same reflection as those of figure 3.12, in PP3II, but following a rotation about the scattering vector. The measured parameters relating to these figures are given in Appendix I.

before the blocks were deformed in compression along $[\bar{1}11]$, two at room temperature and two under liquid nitrogen. Details of these tests, with the results from the mapping before and after deformation, are given in tables 3.7, 3.8 (Appendix). A difficulty with the evaluation of the chart recorder plots arose from the low effective hardness of the Instron for squat specimens. The curves on loading and unloading without a specimen were not always coincident with each other and with the initial portion of the actual stress-strain curve. The most clearly defineable parameter was the final change in height of the specimen measured externally and it is this value of strain which is quoted in the tables. Frictional effects were evident from a slight barrelling of the block sides during compression.

Immediately prior to compression the block faces were electropolished in 60% orthophosphoric acid and water for a few minutes. The slip lines on the crystal faces indicated strong end effects extending over at least half the crystal volume. The crystals were sufficiently deformed for the three most highly stressed slip systems to be active in all four crystals. In block B4 there were very fine, uniform slip lines on $(1\bar{1}1)$, and fine slip with a tendency to form widely spaced, irregular bands of slip on $(11\bar{1})$ and $(111)$. For crystal B1 fine slip lines were evenly distributed on $(111)$ and $(11\bar{1})$, and more difficult to resolve on $(1\bar{1}1)$. Coarse bands of slip lines were formed in blocks B2 and B3 on $(11\bar{1})$ with very irregular spacing between bands. Similar but narrower, widely spaced bands formed on $(1\bar{1}1)$ in B2, but slip on these planes in B3 was fine and did not show a band structure. The $(1\bar{1}2)$ faces developed a textured, cloth-like finish.

| Crystal | Slip plane | Average slip line spacing within band. | Average coarse slip band width. | Average coarse band spacing. |
|---|---|---|---|---|
| | | μm | μm | μm |
| B1 | 111 / 11$\bar{1}$ | - | - | 465 |
| | 1$\bar{1}$1 | - | - | 430 |
| B2 | 111 / 11$\bar{1}$ | 5 | 160 | 460 |
| | 1$\bar{1}$1 | - | 30 to 90 | 225 |
| B3 | 111 / 11$\bar{1}$ | - | 140 | 130 |
| | 1$\bar{1}$1 | 40 | - | - |
| B4 | 111 / 11$\bar{1}$ | 11 | 65 | 88 |
| | 1$\bar{1}$1 | 3 | - | - |

Table 3.9

Approximate slip line spacings from the block crystals. Due to non-uniformity of the deformations these figures are only a guide to the observed dimensions. Where no values are given the spacings were too irregular for an average value to be meaningful.

Rocking curves were recorded for each of the undeformed blocks using the $\bar{1}$11 and 220 reflections. With the $\bar{1}$11 reflection the measurements were made at five 10mm intervals along the centre of the large crystal faces in approximately the same volume for both the (110) and (1$\bar{1}$2) faces of each crystal. Rocking curves for the 220 reflection were recorded consecutively along the centre of the blocks. The mappings were repeated for the same volumes after deformation. Results from these sets of measurements are given in tables 3.7, 3.8 (Appendix I) and figures 3.15, and 3.16. Figure 3.14 shows the change in form of one of the recorded 220 curves for each deformation. The peaks for

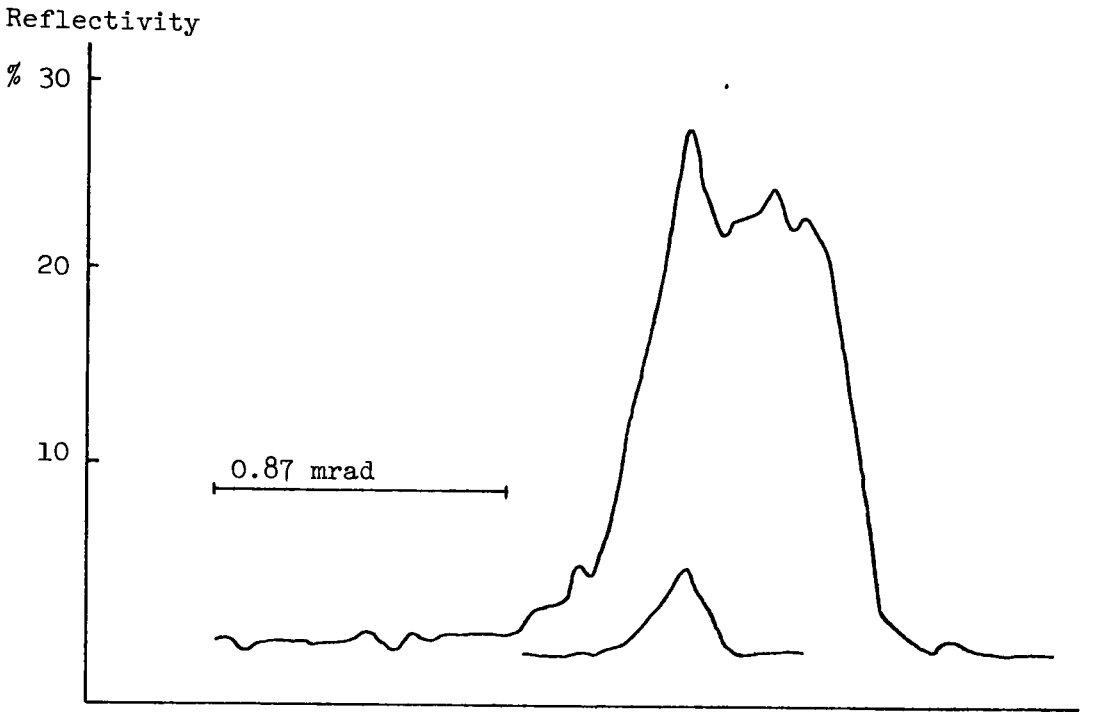


Figure 3.14a

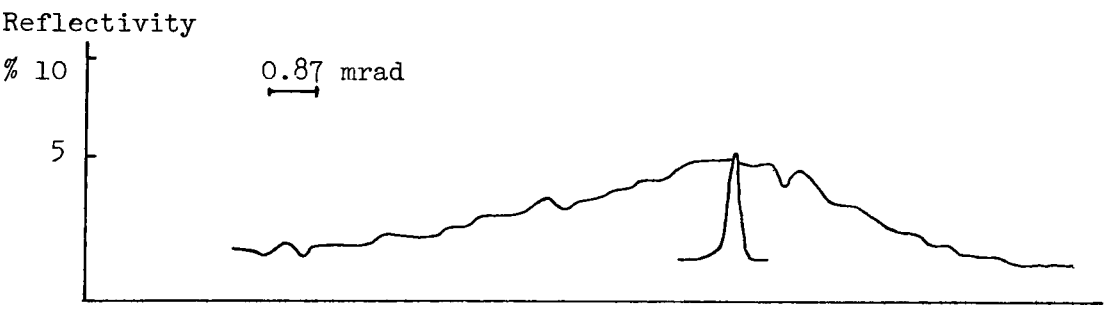


Figure 3.14b

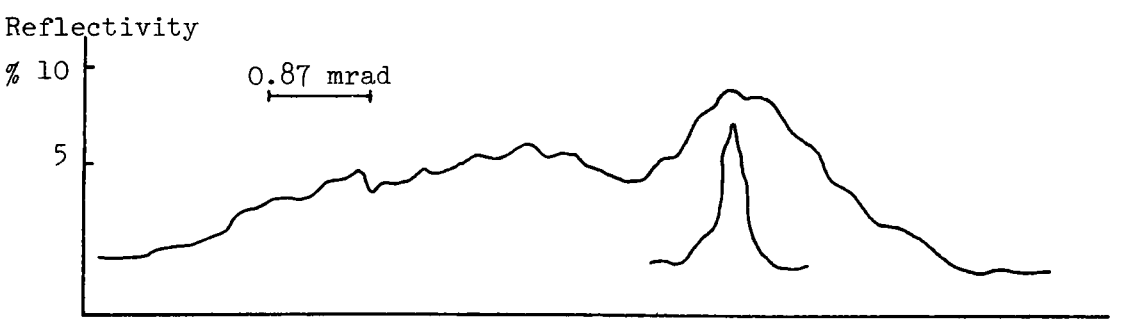


Figure 3.14c

Figure 3.14

Typical rocking curves using the 220 reflection before and after deformation in crystals B1 (top), B2 (middle), and B4 (bottom). The vertical scales are the same, but the horizontal scales differ and the peaks are not to the same angular origin.

B3 are not shown, but for the deformed crystal were similar to those for B2 only much broader. The results given in tables 3.7, 3.8 are averaged over the five measurements in each set. There was a significant difference in the measured peaks on rotation about the scattering vector but they followed the same trend in each volume element. Figures 3.15 and 3.16 show the variation in half-width and angular position of the rocking curves as a function of position in the crystal, recorded using both the $\bar{1}11$ and 220 reflections before and after deformation. All angular measurements are referred to the same origin and the angular peak position varies with translational position in the crystal.

The rocking curves recorded before deformation of the blocks showed no variation with translational position in the crystal, and only small differences in shape between the blocks. After compression all crystals gave double or multiple peaks at the ends, and even the curves from the central region of the least deformed block, B1, were multiple peaked. The rocking curves recorded with the $\bar{1}11$ reflection were narrower and more intense than the 220 curves. Blocks B2 and B3 had single peaks in the central region for both reflections; B4 had a well-defined single peak with the $\bar{1}11$ reflection, but an untidy multiple peak with the 220.

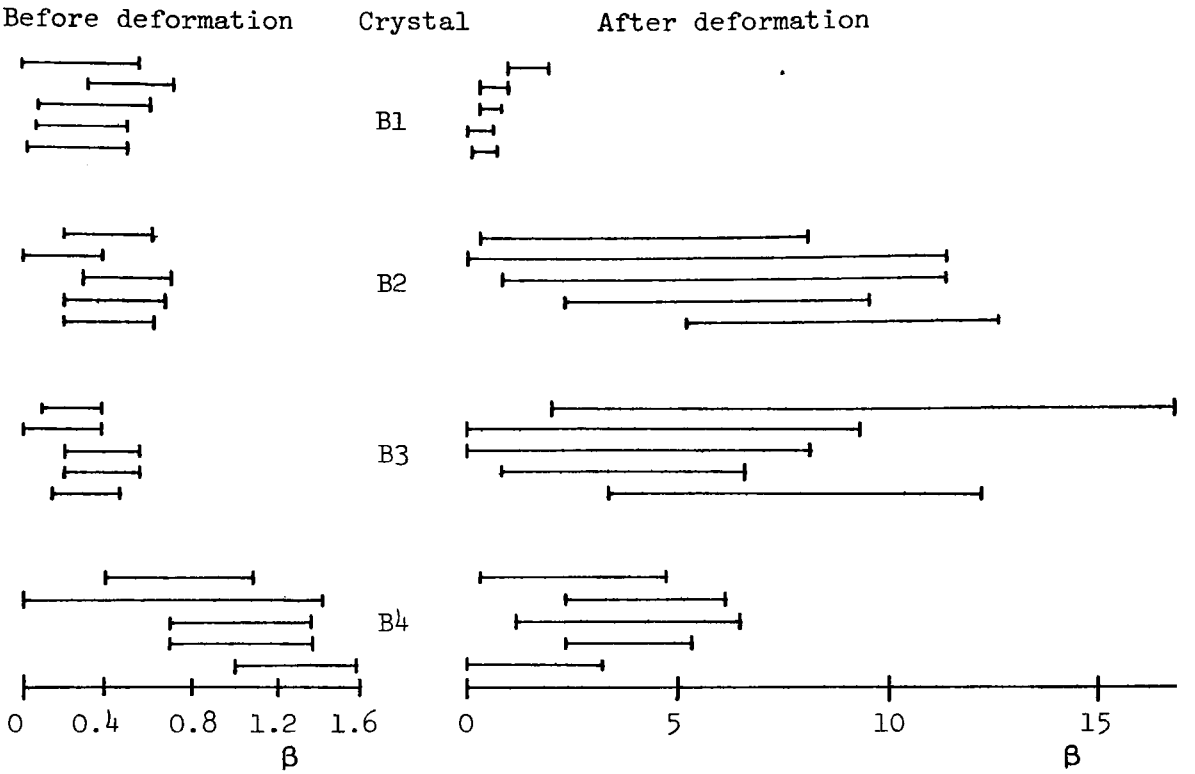


Figure 3.15

The FWHM's in adjacent regions of each B crystal before and after deformation, using the $\bar{1}11$ reflection in figure 3.15 and the 220 reflection in figure 3.16. The horizontal scales are different for measurements before and after deformation.

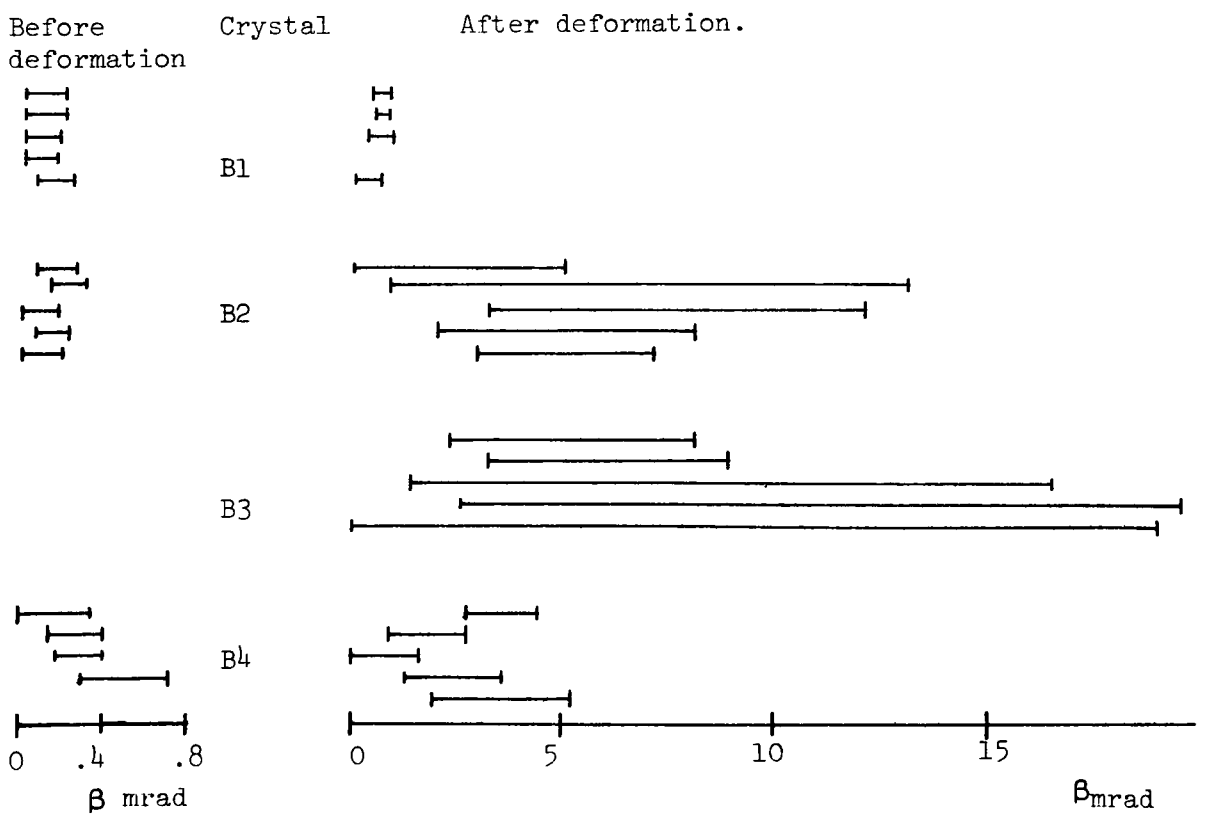


Figure 3.16

## 3.3 Small plate crystals

The rectangular block crystals were halved across their long axes, perpendicular to $[\bar{1}11]$, and from one half of each block pairs of small flat plate crystals, with dimensions 20 x 10 x 3 mm, were cut. These plates were spark-machined from the central region of each half-block to avoid structural inhomogeneities due to end effects during deformation. The plate faces were cut parallel to the primary slip plane (111). Dental wax was used to mask the plate edges during chemical thinning to 2mm in nitric acid to remove machining damage, since the edges are preferentially reduced by acid attack.

The $0\bar{2}2$ reflection was used to map the entire crystal volume by recording rocking curves at 1mm intervals in two overlapping rows (fig. 3.17), using a beam of cross-section 10 x 1 mm. Some details of these measurements are given in figures 3.18 to 3.20 in terms of peak reflectivity and half-width as functions of translational position in the crystal. The horizontal bars representing the FWHM's are centred

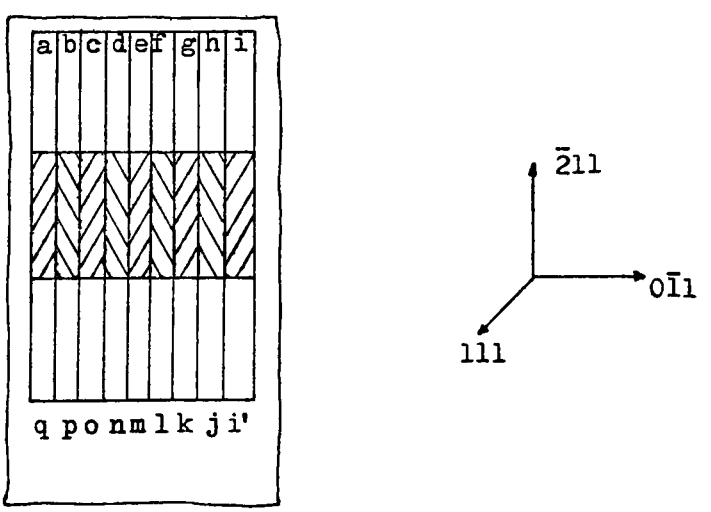


Fig.3.17

A small flat plate crystal showing the volume elements a to i overlapping elements q to i'. The lower region of the crystal was used as a support during measurements.

above the crystal position in which they were measured. The figures show the variability of these parameters over small volumes of crystal. The form of the rocking curves for three representative crystals is also shown in figures 3.18 to 3.20. The angular position in these figures are not referred to in the same origin in each case, but the intensity scales are identical. The curves in figure 3.20 show the appearance of a parasitic reflection on translation of the crystal, indicating a curvature of the crystal planes. The parasitic reflection is a 200 type. The broadening of the peaks i and i' in crystal B11 was due to the measurements being made on the edge of the plate face. The curves for the B3 small plates were of lower intensity and much broader than those for the B2 plates, but were of otherwise similar form. It may be seen in figures 3.18 to 3.20 that even when the half-widths and peak heights are relatively similar in several positions, e.g. fig. 3.18 positions c, e, g, the form of the peaks may vary.

One of each pair of plates was used for an investigation of the effect of rotation about the scattering vector. In each case the beam was aligned with the centre of the crystal face and rocking curves recorded at intervals of $5^{\circ}$ in the range $\pm 25^{\circ}$ to the direction [111], the plate normal, rotating about the vector $0\bar{2}2$. The results from these measurements are given in table 3.10 (Appendix).

The plates were electro-polished in a saturated solution of orthophosphoric and chromic acids for two hours at 10V, 3A and $20^{\circ}C$, to highlight the slip planes. Coarse bands of slip were observed in proportions corresponding to the amounts of slip observed in the block crystals, but the traces were not sufficiently clear for accurate measurements. Various chemical etches, based on hydrochloric acid,

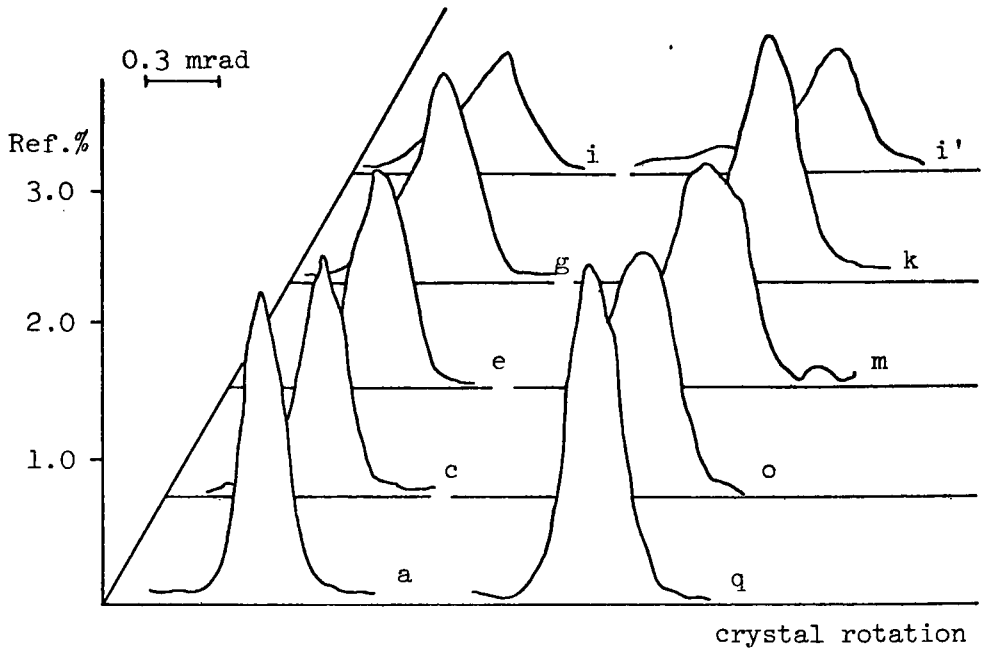


Figure 3.18a

Rocking curves for crystal B11 showing the variation in form. The curves correspond to the positions shown in figure 3.17.

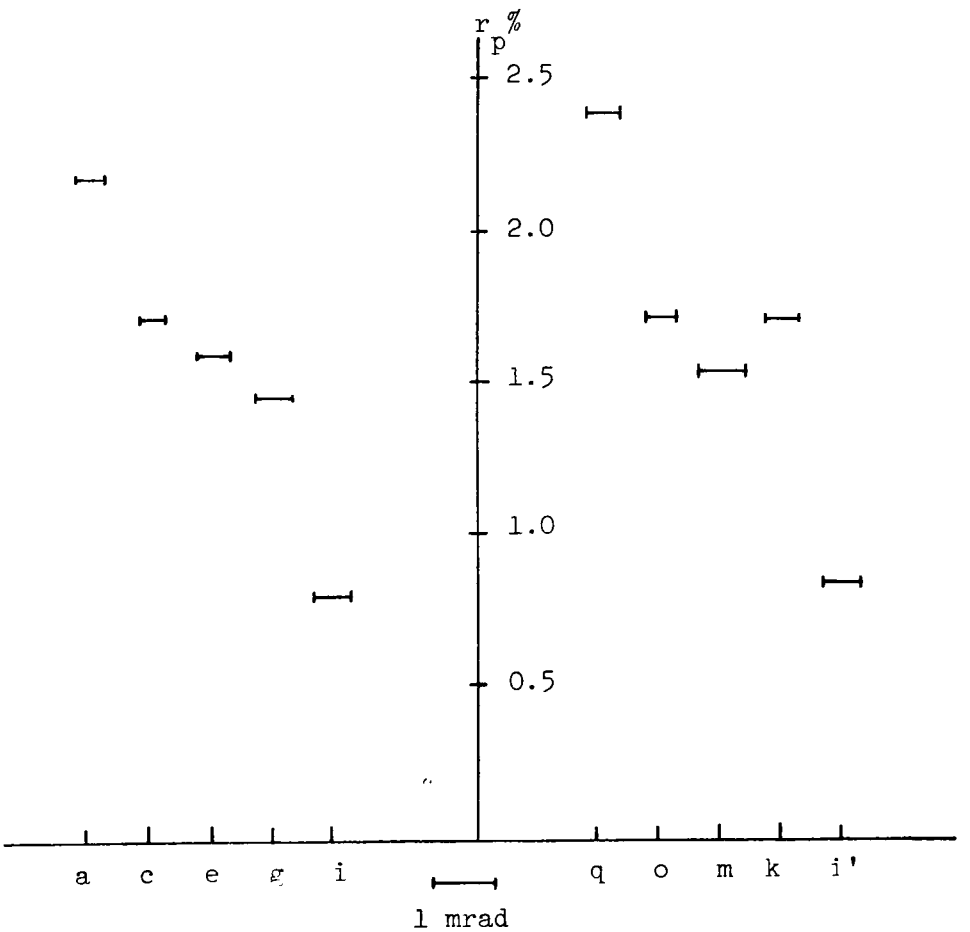


Figure 3.18b

The FWHM's for each of the curves shown above as a function of peak reflectivity for the $0\bar{2}2$ reflection.

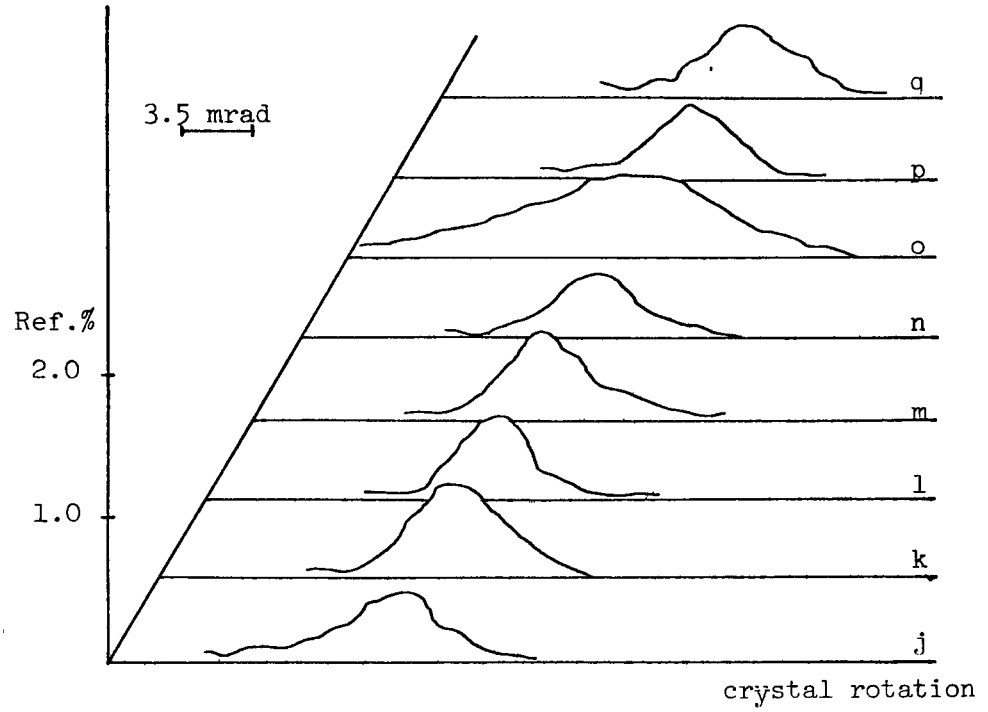


Figure 3.19a

Rocking curves for crystal B21. The lower case letters correspond to the translational positions of figure 3.17. Figure 3.19b shows the half-widths as a function of peak reflectivity for each volume element of B21 using the $0\bar{2}2$ reflection.

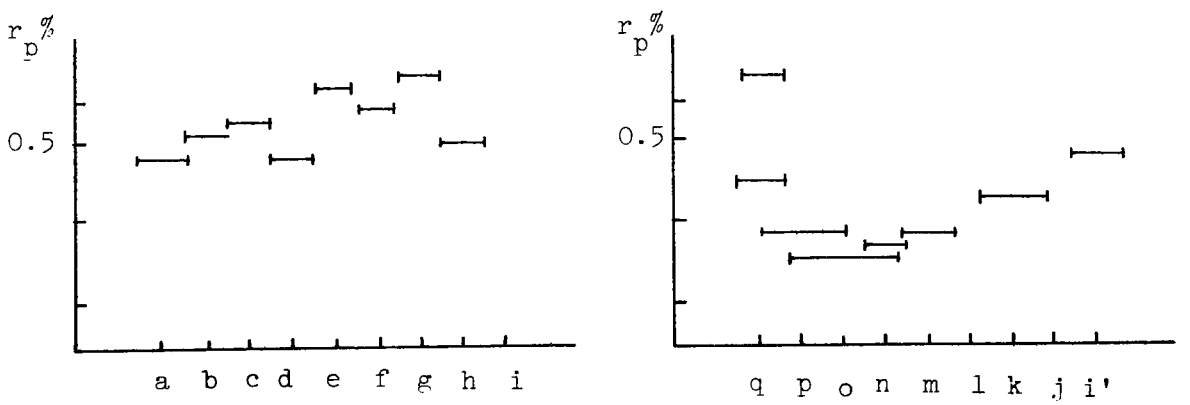


Figure 3.19b

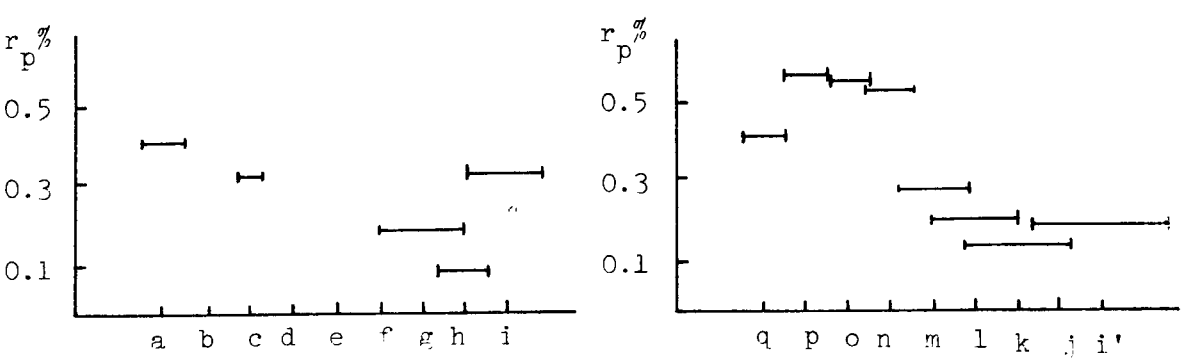


Figure 3.19c

These are the FWHM's for volume elements a to q(fig. 3.17) in plate B31 as a function of peak reflectivity using the $0\bar{2}2$ reflection.

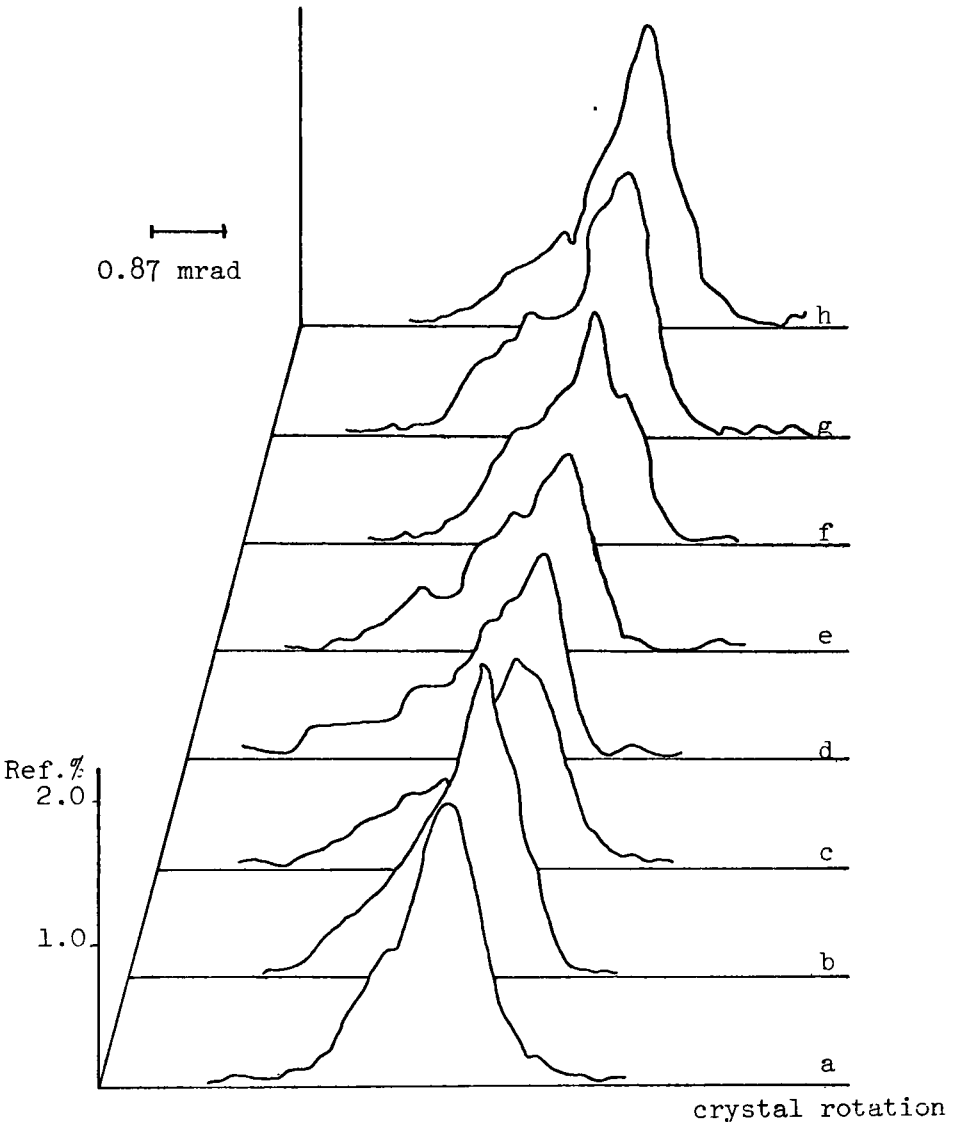


Figure 3.20a

The form of $0\bar{2}2$ reflection rocking curves for positions a to h (figure 3.8) in crystal B41.

Figure 3.20b

This shows the measured FWHM's versus peak reflectivities for the translational positions.

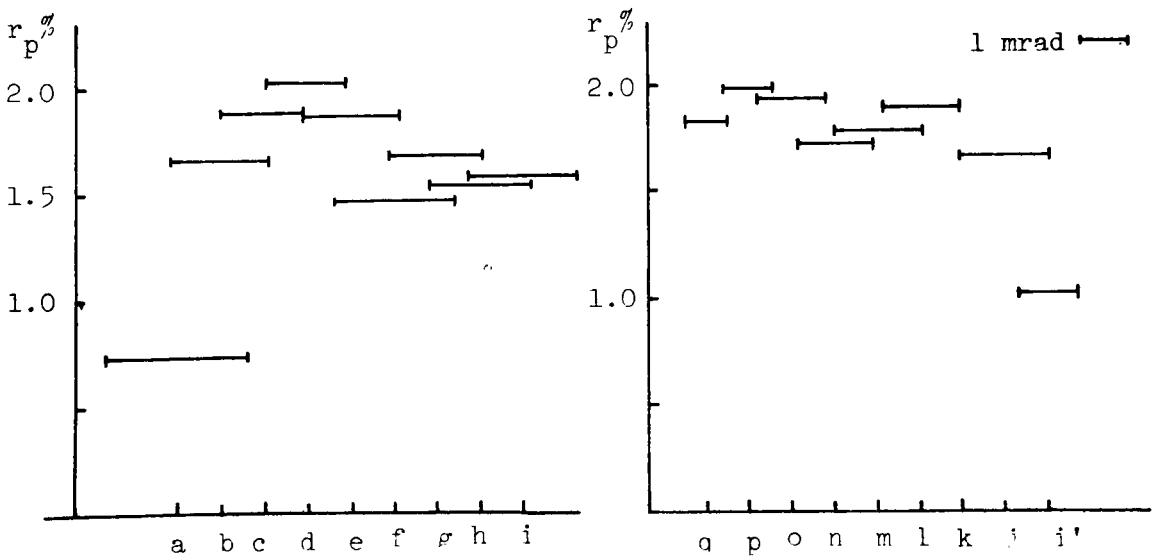

ferric chloride and bromine, failed to improve the optical quality for measurements. Pitting occurred more heavily on the coarse bands than in the adjacent regions of crystal.

## 4. Electron diffraction

To determine the microstructure of the deformed crystals, the flat plate PP4, and the small flat plates from the rectangular block crystals were sectioned to provide thin foils for transmission electron microscopy, (TEM). The electron microscope used was a J.E.M. 100C, (JEOL), fitted with a double tilt holder and operated at 100kV.

### 4.1 Preparation of foils

One of the most common procedures for preparing thin foils for transmission electron microscopy is to produce discs of the appropriate diameter from thin sheets of material using a cylindrical spark-machine tool. The discs are then electropolished until a small region is electron transparent, usually around a perforation. It has been shown that spark-machining copper introduces considerable damage to a depth of about 300μm from the cut surface[69]. For this reason it was decided to use an acid saw to produce slices 500μm thick and a masked etch in acid to produce the discs.

The acid saw consisted of 110μm diameter stainless steel wires strung taut across a trolley, which had one dimensional horizontal motion controlled by an electric motor and pulley system. Concentrated nitric acid dripped onto the wires traversing the crystal against which they were carefully balanced to concentrate the flow of solution into the cut without mechanical sawing. It was possible to make six cuts simultaneously, with a cutting rate of less than a millimetre per hour for a 10mm block of copper. Despite acid-resistant protective coatings there was considerable attack from the acid atmosphere and back-etching due to the length of time necessary to complete a cut.

An alternative method was to use 110μm stainless steel wire and the finest setting on a Wickman spark machine to produce slices between 700 and 1000μm thick. The slices were then electro-thinned to between 350 and 400μm in a solution of orthophosphoric acid saturated with chromic acid, polishing one side at a time by glueing the slice to a glass slide. With this technique a cutting rate of 2mm per hour was achieved and no loss of material since during thinning the slice edges were protected by adhesive. The disadvantages of this method were that the wire eroded during cutting and required renewing every second cut, and that the quality of the cut was very sensitive to the uniformity of the winding of the wire on the bobbins.

A comparison of foils from an undeformed single crystal prepared by each method showed no apparent difference in density or distribution of dislocations, so most of the slices were prepared by spark erosion. The dislocation arrays resulting from deliberate mis-handling were significantly different from those observed in actual specimens, and appeared to have little interaction with the deformation structure. There was, however, some loss or rearrangement of dislocations in the very thin area around the hole, most noticeably for foils with a <111> foil normal. For this reason most measurements were made at least 15μm from the hole.

Discs were prepared from the slices by masking with 3mm diameter discs of pvc adhesive tape. The excess copper surrounding the discs was dissolved in 75% concentrated nitric acid. The pvc tape was removed in acetone. Where it was desirable to know the position of each foil with respect to the slice, the slices were glued to glass slides with an adhesive which dissolved in acetone more slowly than

the adhesive on the pvc tape. Thus it was possible to remove the pvc tape leaving the separated discs in their original positions. A thorough wash in acetone removed all trace of adhesive.

For the final stage of foil preparation, a jet electropolishing unit with a photocell controlled cut-off was used. Of the more common electrolytes used for the preparation of copper foils, nitric acid with methanol proved unsuitable for use with this unit (Struers Tenupol), and combinations of orthophosphoric acid, an alcohol and water gave better results. The solution used was 25% orthophosphoric acid, 25% ethanol and 50% distilled water, at 15°C. This electrolyte had the advantages of being relatively insensitive to changes in temperature and concentration, but too low a flow rate caused the foil to be attacked at the edges rather than dishing in the centre. The optimum voltage was 2.4V, and the current range was 10 to 25mA according to foil size. The polished foils were left with a gelatinous coating which was removed by rinsing in dilute ammonium hydroxide, then ethanol and methanol cyclically, and finally ether.

Crystal PP4 was sufficiently large for 1mm thick slices of several different orientations to be prepared from each thickness. The slices were cut parallel to planes (011), ($\bar{1}$10), ($\bar{1}$11) and (111). The (011) slices were taken from the external surfaces of the crystal. The small flat plates cut from the rectangular blocks had their large faces parallel to the primary slip planes, (111), and foils were prepared with 111 foil normals. Each small plate was cut into two slices 1mm thick by spark machining, and the foils prepared from these slices.

The deformation axis for PP4 was [ 011 ] so the primary and conjugate slip systems were assumed to be equivalent, i.e. primary slip occurred on (111) in the [ $\bar{1}$01 ] and [ $\bar{1}$10 ] directions, and on ($\bar{1}$11) in the

[ 101 ] and [110] directions. For the large plates the term conjugate slip is used to refer to the remaining two slip systems. The small plates cut from the block crystals had deformation axes [ $\bar{1}11$ ] and at least two of the most highly stressed systems operating. The Burgers vectors for the active slip systems are [ $\bar{1}01$ ] and [$\bar{1}10$] on (111), [011] and [ $\bar{1}10$ ] on ($\bar{1}\bar{1}1$), and [011] , [$\bar{1}01$] on ($1\bar{1}1$). Low order Bragg reflections were the most effective for determining dislocation Burgers vectors and densities. The reflections used were of 111, 200, 220 and 224 types.

## 4.2 Interpretation of the electron micrographs

An estimate of the foil thickness, f, was obtained from the projected length, $L_p$, of a line feature known to pass from top to bottom of the foil. If the beam direction is parallel to the foil normal this is given by

$$f = L_p \tan\theta \qquad 4.1$$

where $\theta$ is determined from the line direction. When the foil normal is not parallel to the beam direction, the following expression applies

$$f = \frac{L_p(h_1h_2 + k_1k_2 + l_1l_2)}{(h_3^2 + k_3^2 + l_3^2)^{\frac{1}{2}}} \left\{ (h_1^2 + k_1^2 + l_1^2) - \frac{(h_1h_2 + k_1k_2 + l_1l_2)^2}{(h_2^2 + k_2^2 + l_2^2)} \right\}^{-\frac{1}{2}}$$

where the line direction is $h_1k_1l_1$ , $h_2k_2l_2$ is the beam direction, and the foil normal is $h_3k_3l_3$ . The values obtained using this method were accurate to about 20%. All measurements were made in foil thicknesses of between 2500Å and 3500Å.

Dislocation densities were measured by counting the number of intercepts, $\nu$, of the dislocations with a set of randomly centred

circles and using Ham's equation[70]

$$\rho = \frac{2\nu}{L_c f} \qquad 4.3$$

where $L_c$ is the total length of the circles; f, the foil thickness; and $\rho$ the dislocation density. The densities were measured for each region containing a different type of dislocation structure and for the relatively dislocation free areas, and averaged over a number of micrographs. It was not possible to determine the dimensions of areas of heavy deformation since they were not uniformly distributed throughout the crystal, and were of such magnitude that only one or two would be partially visible in any one foil. For determining dislocation densities, the operating reflections were chosen to have all the primary or conjugate dislocations in contrast simultaneously. Densities for 2-dimensional structures were not obtained if their spacing in the third dimension was uncertain.

The orientation change, $\delta\vartheta$, across a band was measued by Kikuchi line shift, $L_k$, according to

$$\delta\vartheta = \frac{L_k \lambda}{x d_o} \qquad 4.4$$

where $\lambda$ is the electron wavelength, x is the distance of the reflecting spot from the centre of the diffraction pattern, and $d_o$ is the lattice spacing of the reflecting planes associated with the Kikuchi lines. Using the selected area aperture a diffraction pattern relating to the slip band and one relating to the adjacent dislocation free area could be obtained. $L_k$ is the difference in position of the Kikuchi lines between the two micrographs.

## 4.3. T.E.M. observations

4.3.1 The stability of thin foils in the electron beam

One effect of the electron beam on the specimen is to break down some of the hydrocarbon vapours which are continually being absorbed and desorbed on the foil surface, and hence build up a layer of carbon-rich contamination on the specimen. The film is formed in a state of stress and is partly relaxed by deformation during observation. This is clearly shown by the formation of extinction contour patterns, fig. 4.1a, on the image of the foil. The film has an effect on the movement of dislocations since the surface step of the crystal can either be accommodated by deformation of the film, or is trapped between the film and the crystal surface giving rise to slip trace contrast, fig.4.2. Interaction of the film and dislocations caused the jerky movement of dislocations observed in the thinner parts of some foils, and the wide splitting of partial dislocations which occurred frequently despite the relatively high stacking fault energy, fig.4.1b.

A variety of slip plane contrast effects were observed in the foils. Sometimes the whole visible part of the slip plane changed contrast, becoming uniformly lighter or darker than the background, (fig.4.2), and in other cases a black-white pair of lines remained along the traces of the slip plane on the foil surfaces. In figure 4.2 two sets of slip plane contrast are visible. These contrast effects were probably due to a surface layer of carbon either deposited by the electron beam, and/or remaining from the foil preparation. Since the effects were observed occurring in the microscope they are more likely to be due to the cracking of hydrocarbons than to a surface layer of oxide. The faults which

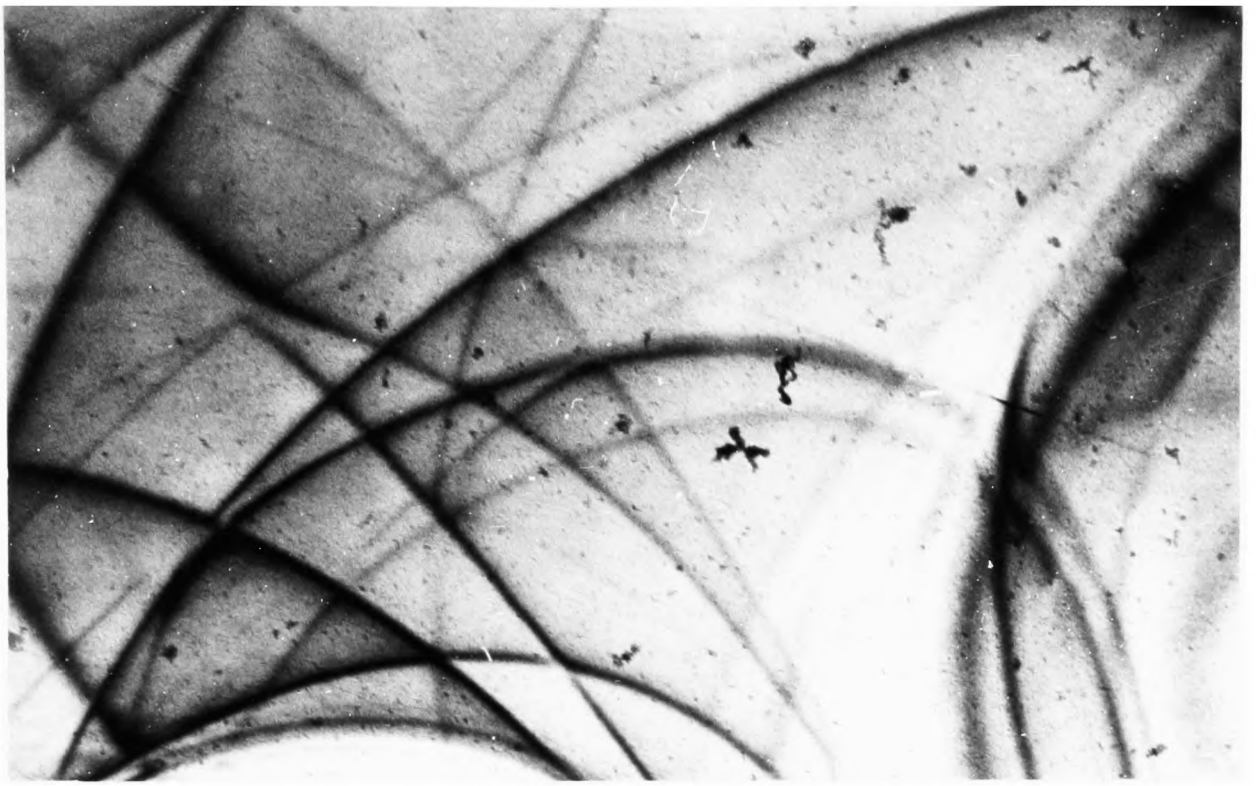

Figure 4.1a

Extinction contour patterns due to the formation of a thin film of hydrocarbon on the surface of the foil. The contours move under the influence of the electron beam.

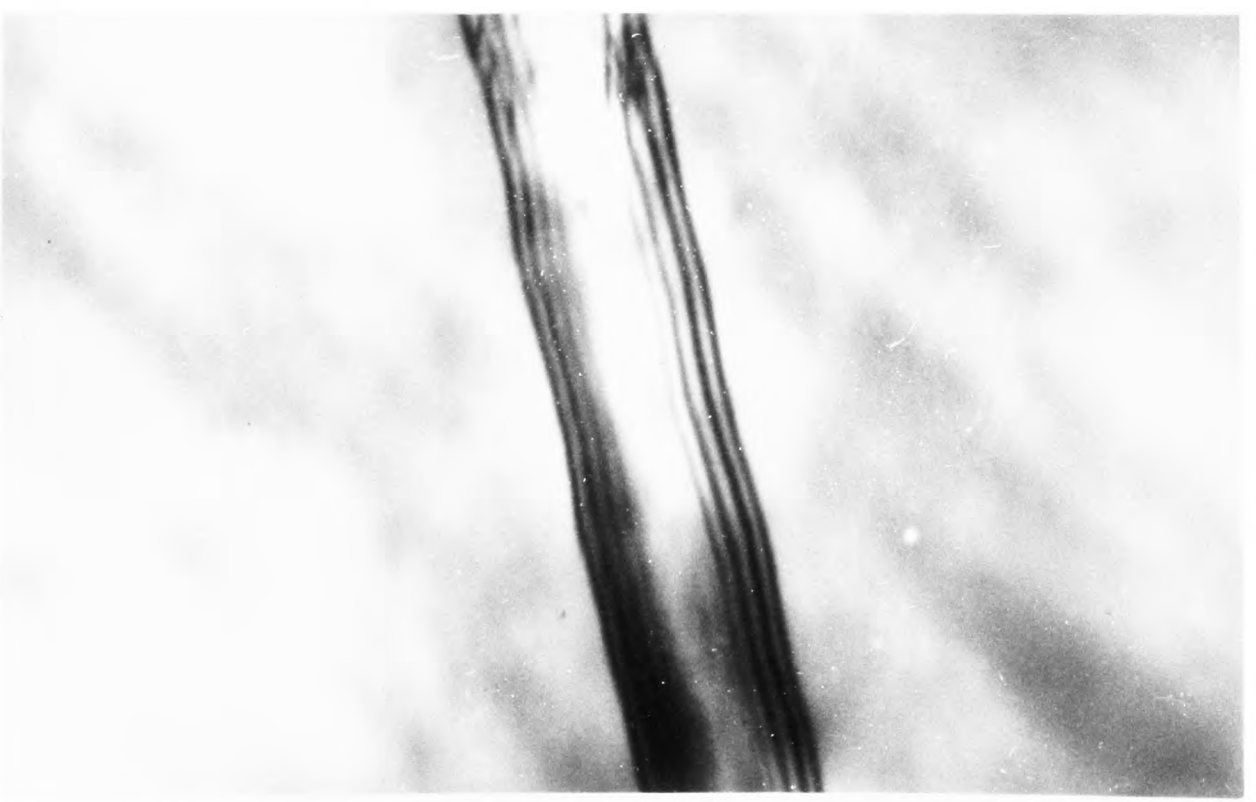

Figure 4.1b

Stacking fault fringes from a fault caused by surface contamination.

1μm

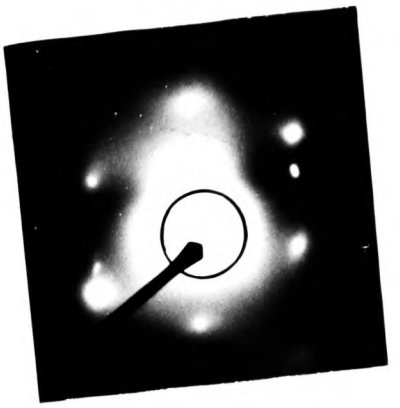

Figure 4.2a

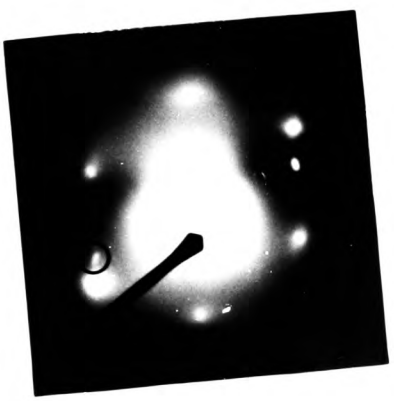

Figure 4.2b

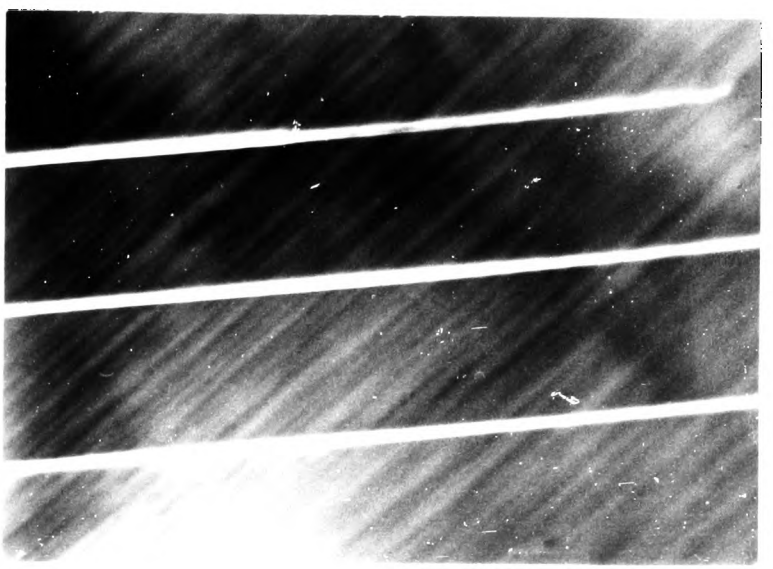

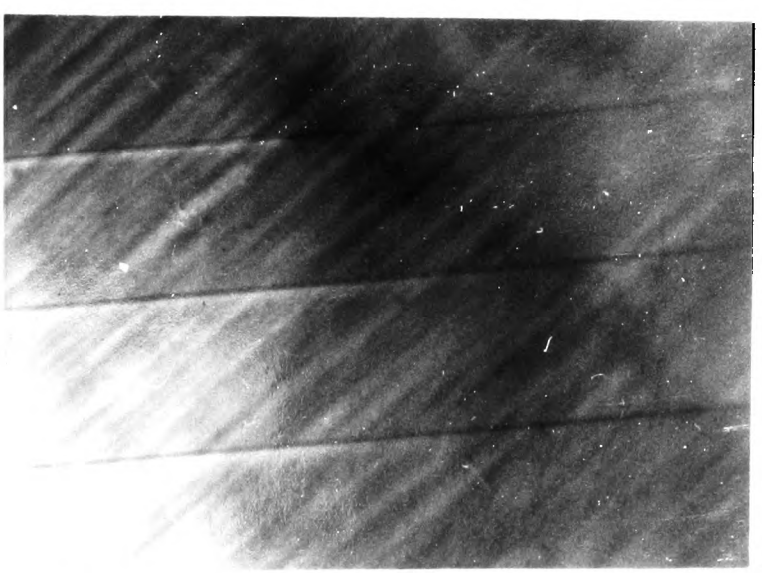

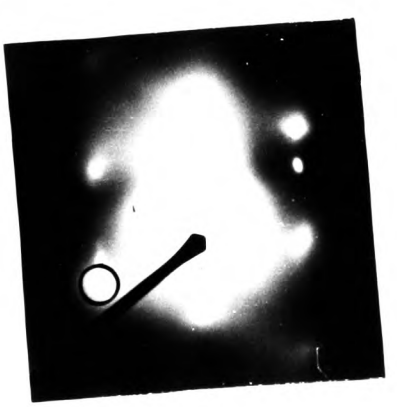

Figure 4.2c

Figures 4.2

Two sets of slip plane contrast are visible in these micrographs, and one set has given rise to double diffraction spots, as is shown by imaging the relevant spots. The spot ringed on the diffraction pattern was used to give the adjacent image. $\underline{B}$ = [022].

formed were, in some cases, large and numerous enough to give strong double diffraction spots, fig. 4.2. The surface contamination could be reduced, but not eliminated, by careful washing of the foils in cold ether, then drying in air, before putting them in the microscope.

4.3.2 Glossary of terms used to describe the dislocation structures

primary dislocations : dislocations on the most highly stressed slip system, or on the two equally highly stressed systems in the large flat plates.

secondary dislocations: all other dislocations.

wall : 3-dimensional arrangement of dislocations inclined to the plane of the foil.

bundle: a bunch or group of dislocations approximately parallel to each other.

braid : a 2-dimensional arrangement of dislocations on a slip plane
or
carpet which in projection onto the plane of the foil appears as a linear structure of narrow width.

tangle: an irregular and inhomogeneous structure containing roughly equal numbers of primary and secondary dislocations.

cells : relatively dislocation free regions irregularly bound by walls, forming areas completely enclosed in two dimensions.

mesh : 2-dimensional network of dislocations of uncertain extent on the primary slip plane.

These definitions are not identical to those found in published articles.

Referring to the flat plate PP4 -

circumference : the curved surface surrounding the plate.

surface : the flat faces of the plate before cutting to step configuration or the surfaces parallel to these

faces after cutting.

central region : the entire thickness corresponding to the middle of the faces.

central layer : a layer parallel to and equidistant from the original unstepped faces.

4.3.3. Crystal PP4

The variation of the structure through the thickness of the crystal was from a very densely-walled cell structure at the surface, to an arrangement of ill-defined coarse bands and dislocation free areas. The dislocation density changed by a factor of six from surface to centre. The dislocation arrangements in the bands took the form of cells, the walls of which decreased in thickness and density of dislocations towards the centre of the crystal.

The foils taken from the surfaces of the thicker regions were very heavily deformed, showing an irregular cell structure with walls composed of tangled dislocations (figure 4.3). The tangles were so dense that it was not possible to analyse the component dislocations. The dense walls were aligned roughly parallel to {111} planes. Under the diffracting conditions for figure 4.3 all primary and most secondary dislocations were visible. The 'dislocation-free' regions between cell walls had dimensions of less than 0.5μm.

Foils taken from a few millimetres below the outer surface of the plate showed a more open, but still very irregular, cell structure. In this type of structure the cells had diameters of about 5μm, and had thick walls of dislocations in tangles or braids. The thicknesses of these walls varied from about 1.5μm to 4μm depending on whether they were composed of single braids of dislocations, tangles or a cell structure. The walls aligned parallel to the primary slip planes were

Figure 4.3 1μm

The cell structure in the surface of the thickest region of PP4, with walls composed of heavily tangled dislocations.

Figure 4.4 0.5μm

This shows an area of thick cell wall in a foil taken from near the surface of the 8.7mm region of PP4.

more densely populated with dislocations, and showed a tendency to form cell structures within the wall. Some areas of wall appeared to be formed of dense bundles of dislocations, (figure 4.4), and had groups of dislocations which were fairly straight and parallel to each other, while other areas of wall contained mixtures of dislocations in various orientations, forming loose tangles. The cell walls were aligned both along the slip plane intersections and perpendicular to them, forming a closed structure in three dimensions.

In some regions of the foils the cell structure opened out and the walls became finer, containing less-tangled dislocations in the form of dislocation braids, (figure 4.6). The braids in these regions tended to be less than 1 μm wide and the dislocations appeared almost randomly distributed within them. The angular misorientation on passing from the dense structure to the more open arrangement was, on average, of the order of 4mrad. Figure 4.7 shows the remains of a cellular structure on a micrograph taken in an adjacent foil under the same diffracting conditions as figure 4.6. Distinct misorientations were observed across dislocation braids in foils taken from the vicinity of the plate circumference in the 8.7mm region. The rotations were up to 40 mrad and typically of the order of 7mrad about <211> axes, as shown in figure 4.8. The dislocation densities in such regions were approximately $3 \times 10^{7} mm^{-2}$, and in regions like that of figure 4.7 the densities were of the order of $1 \times 10^{7} mm^{-2}$. Figure 4.7 shows the effects of surface contamination.

Braids of tangled dislocations were aligned parallel to the traces of the primary slip systems, and the nature of these braids varied widely throughout the foils, c.f. figures 4.4 to 4.12. Figure 4.10

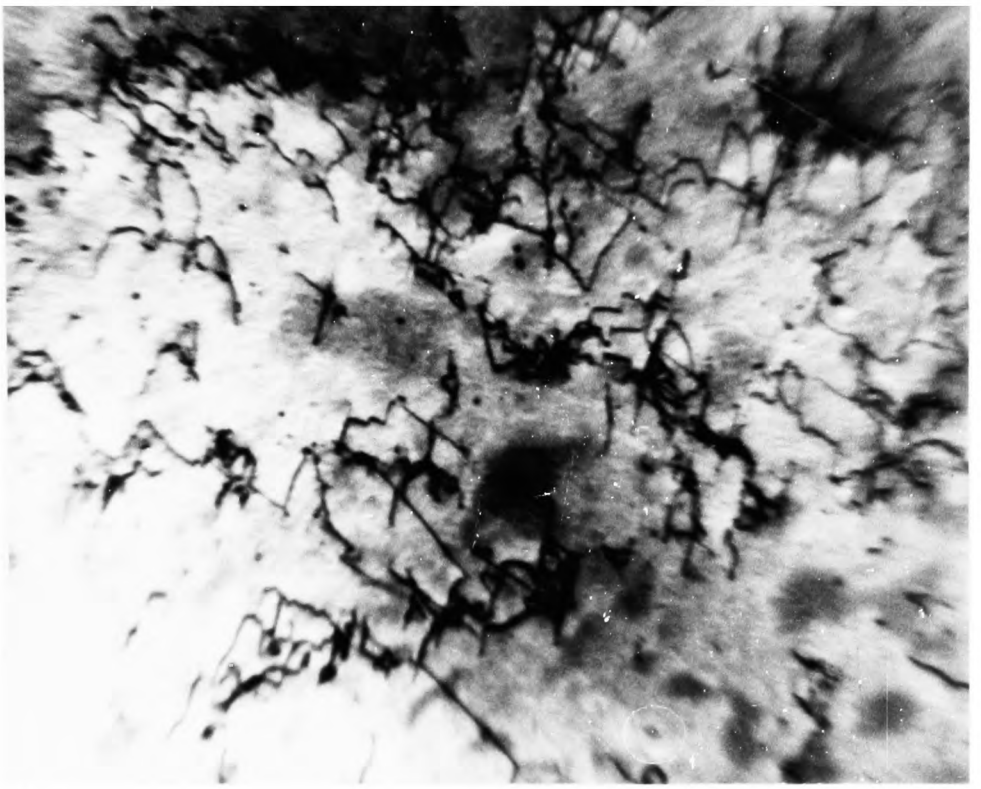

Figure 4.5 1μm

Loose tangles of dislocations in cell walls in an area from the central layer of PP4 near the circumference. All primary dislocations are in contrast.

Figure 4.6 1μm

Micrograph showing dislocation braids in an area of foil taken from a few millimetres below the surface in the centre of the 8.7mm region of PP4. Primary dislocations with [101] and [1$\bar{1}$0] Burgers vectors are out of contrast.

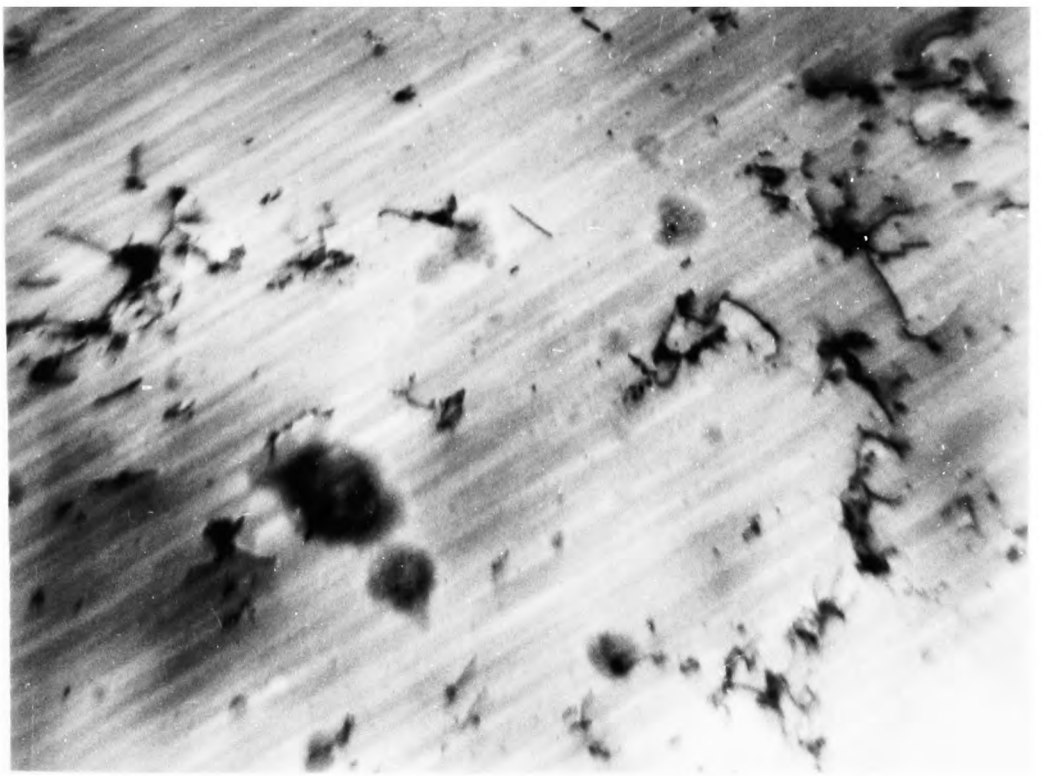

Figure 4.7

A micrograph from a foil adjacent to that of fig. 4.6 but nearer the centre, and imaged under identical diffracting conditions. The striations are due to slip plane contrast.

1μm

Figure 4.8 1μm

This shows a region strongly misoriented across bands of dislocations. The foil was taken from the 8.7mm region of PP4, near the circumference.

shows part of a cell wall containing two parallel bundles of dislocations aligned nearly parallel to {111} planes, and is a micrograph from an area similar to that shown in figure 4.12, which shows the cell structure near the surface of the central region of the plate.

Towards the centre of the crystal the structure took the form of bands containing a fairly dense, tangled structure adjacent to relatively dislocation-free areas tens of microns across. Part of one such dislocation-free area is shown in figure 4.9, in which the double images are single dislocations not dipoles. Figure 4.11 shows the transition from coarse slip band to 'dislocation-free' area. The coarse slip bands had a roughly cellular structure which became more dense towards the centre of some bands. It was not possible to determine dimensions of either slip bands or 'dislocation-free' areas because the electron-transparent regions in the foils were not greater than 60 x 60 μm in most cases. In all foils from the central layer the widths exceeded 20μm. The tangles in these bands contained a mixture of primary and secondary dislocations and the cell structures varied considerably so it was not possible to define an average cell size. The largest cells in the coarse bands had dimensions of about 1μm. The larger 'dislocation-free' areas often contained a scattering of extremely short dislocation lengths, which could be due to rearrangement during thinning. An average dislocation density in the bands, from several foils, was about $3.0 \times 10^{7} mm^{-2}$ 'dislocation-free' areas an approximate density was $0.9 \times 10^{7} mm^{-2}$. This compares with about $5 \times 10^{7} mm^{-2}$ for the denser walls nearer the crystal surface, and $1.5 \times 10^{7} mm^{-2}$ for the finer walls in a similar position with respect to the crystal surface. These values are quoted to give an order of

Figure 4.9

An example of a relatively dislocation free area from the central layer of the crystal PP4. Most primary dislocations are in contrast and the double images have $\underline{g}.\underline{b} = 2$.

1μm ⊢————⊣

Figure 4.10

A cell wall containing a pair of dislocation bundles in a foil taken from a few millimetres below the surface of the 11.2mm region of PP4.

0.5μm ⊢————⊣

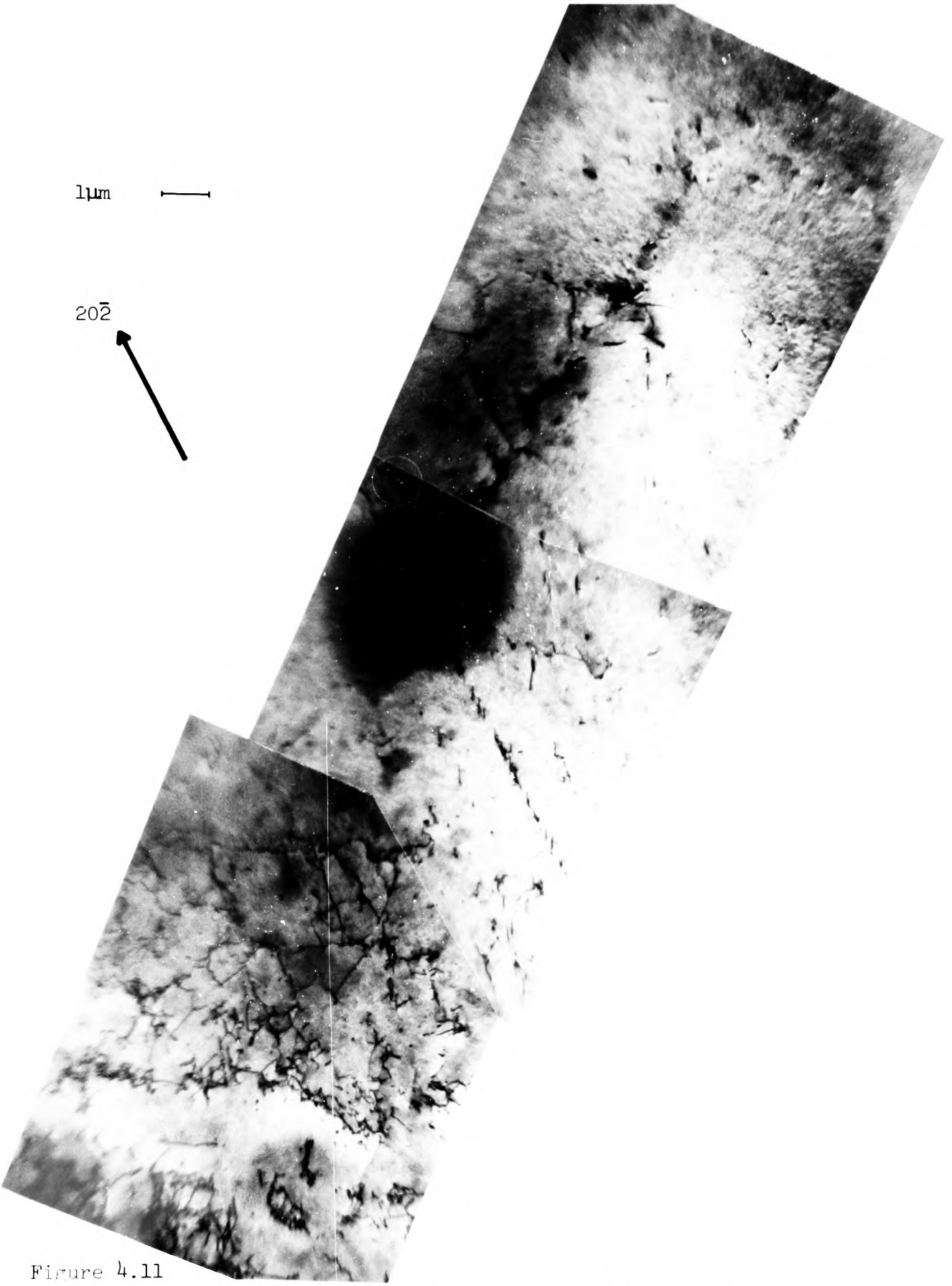


Figure 4.11

This micrograph shows the edge of a coarse slip band and the adjacent 'dislocation free' area in a foil from the 2.5mm thickness of PP4.

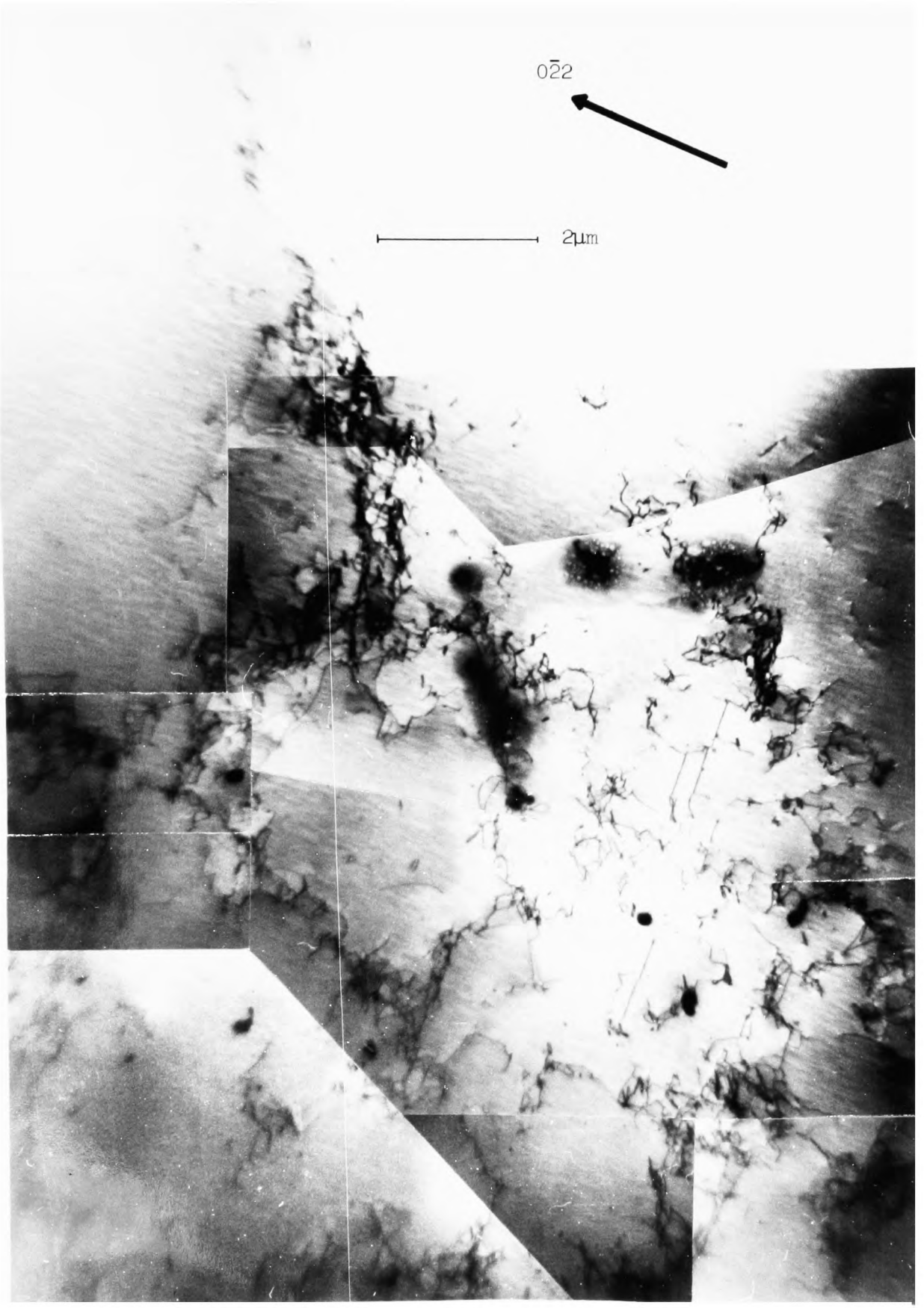


Figure 4.12

Micrograph from near the surface of the 11.2mm region of PP4, under diffracting conditions for which all primary dislocations are visible.

magnitude for the dislocation densities and show the degree of variation over the various parts of the crystal. The degree of misorientation across the coarse bands was of the order of 3mrad.

Although the dislocation arrangement varied considerably within the crystal, the dislocation density did not have a wide range of values. The centre of the plate showed the least deformation, with fairly short dislocations arranged in braids, whereas the edges and surfaces had cell structures of greater or lesser complexity.

4.3.4 The small flat plates

The microstructures observed in these crystals were significantly different in the plates from blocks B1, B2 and B4, but plates from B3 were similar to those from B2. The foils taken from the plates of B1 contained so few dislocations that estimates of density were unsatisfactory. Foils were cut normal to (112) planes in order to reduce any loss of dislocations during preparation by presenting a free surface less favourably oriented for cross-slip. However there was no obvious difference in the number of dislocations or their arrangement between foils of either (112) or (111) orientation. Slip appeared to have occurred predominantly on two of the three equally stressed systems in both the plates prepared from this block. Where dislocations were observed there was no evidence for the formation of any kind of extensive structure in two or three dimensions, and often the dislocations that were found had projected lengths of less than 0.2μm. Figure 4.13 shows some of the longer dislocations observed in plate B11.

Two different dislocation structures were found in the plates from B2, although they did not show a well-defined band structure. There were regions of large open cells with dimensions of 2μm and

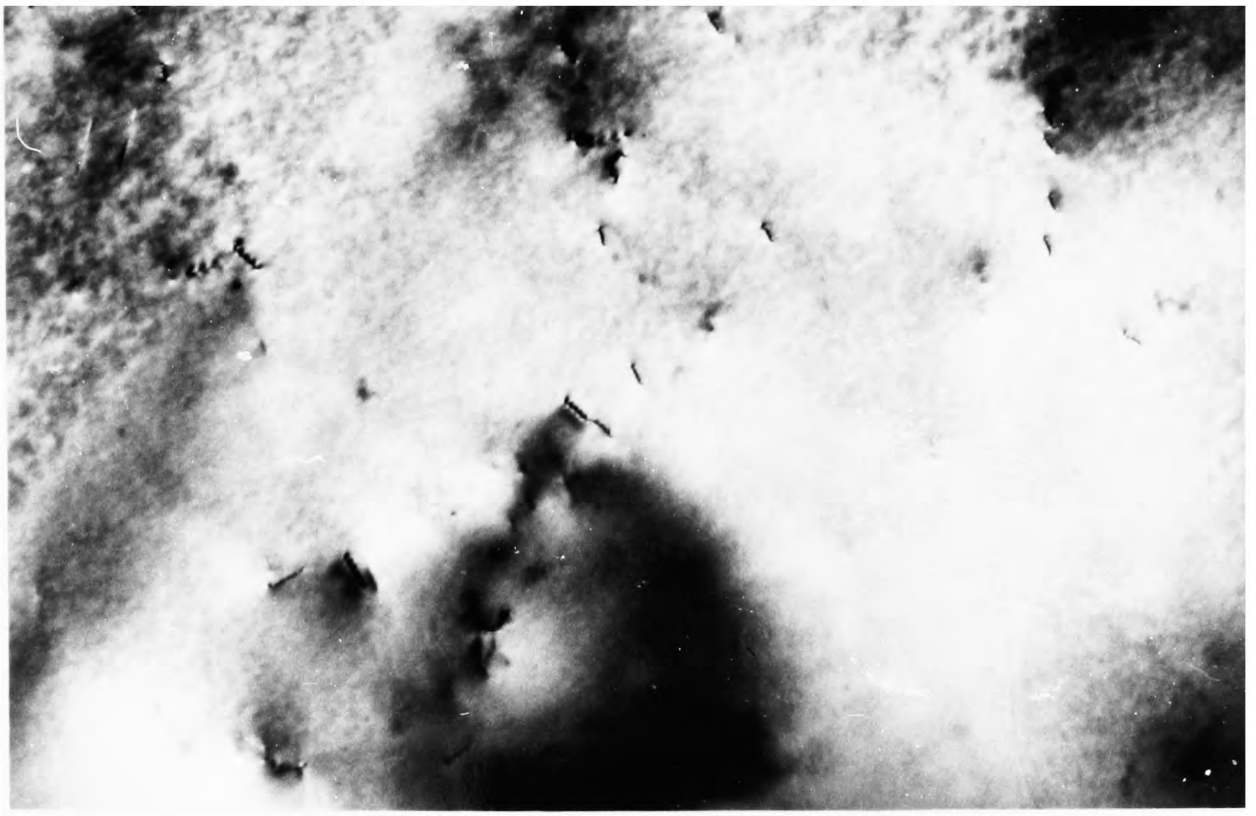

Figure 4.13
This shows a region of high dislocation density from plate B11. Not all dislocations are in full contrast; some are only showing residual contrast.

2μm

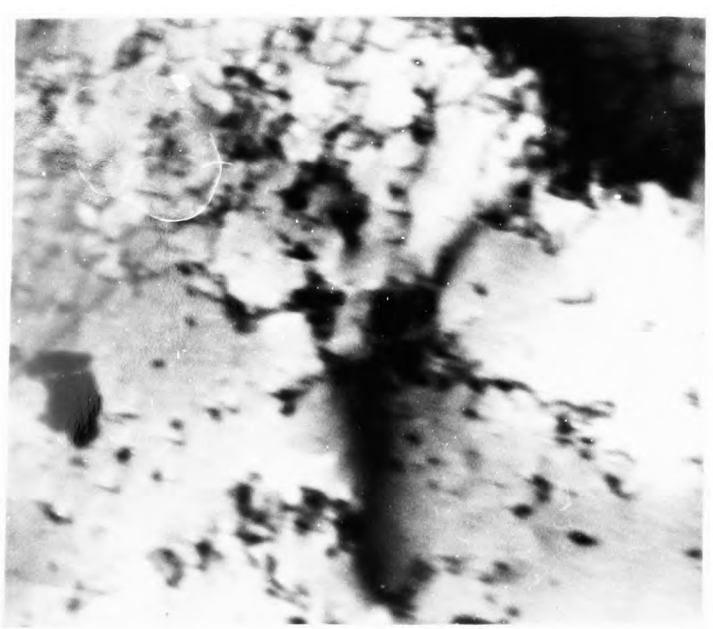

Figure 4.14
Micrograph from a B2 platelet showing a misoriented region (top right), and the transition from a mesh structure to a relatively dislocation free area.

1μm

a fine irregular mesh of tangled dislocations enclosing extremely small dislocation free areas. Both types of structure covered large areas and their full extent was beyond the dimensions of the electron transparent regions of the foils even at the lowest magnification. In some foils the transition from large cell to mesh structure was marked by a lattice misorientation of about 5mrad. The cell structure had an approximate dislocation density of $2 \times 10^{8} mm^{-2}$. There was no particular Burgers vector prevalent in any part of the foils. In parts of the crystals the dislocations and braids in the mesh-type structure tended to align parallel to one particular set of {111} planes, whereas in the large cell structure the dislocations in walls took the orientation of the walls. These walls were less rigorously parallel to {111} planes. The mesh arrangement showed a greater tendency to paired bundles of dislocations than in the larger cell walls. Figure 4.14 shows the edge of a mesh region opening into an area of large cells, and in the top left corner is a band of mesh structure misoriented with respect to the rest of the foil. The large cell structure and the mesh are shown more clearly in figures 4.15 and 4.16. The black spots and stains are caused by a film of hydrocarbon on the foil which condenses under the influence of the electron beam.

The microstructure of B3 was intermediate between the large cells and mesh arrangements of the plates from B2. Where the structure was composed of cells with fairly dense walls, the cells were smaller than in B2, but the mesh in B3 was generally more open. Dislocations of all possible Burgers vectors were found in approximately equal numbers, and equally distributed on each set of planes. The overall dislocation density was about $6 \times 10^{10} mm^{-2}$, which was greater than that in the B2

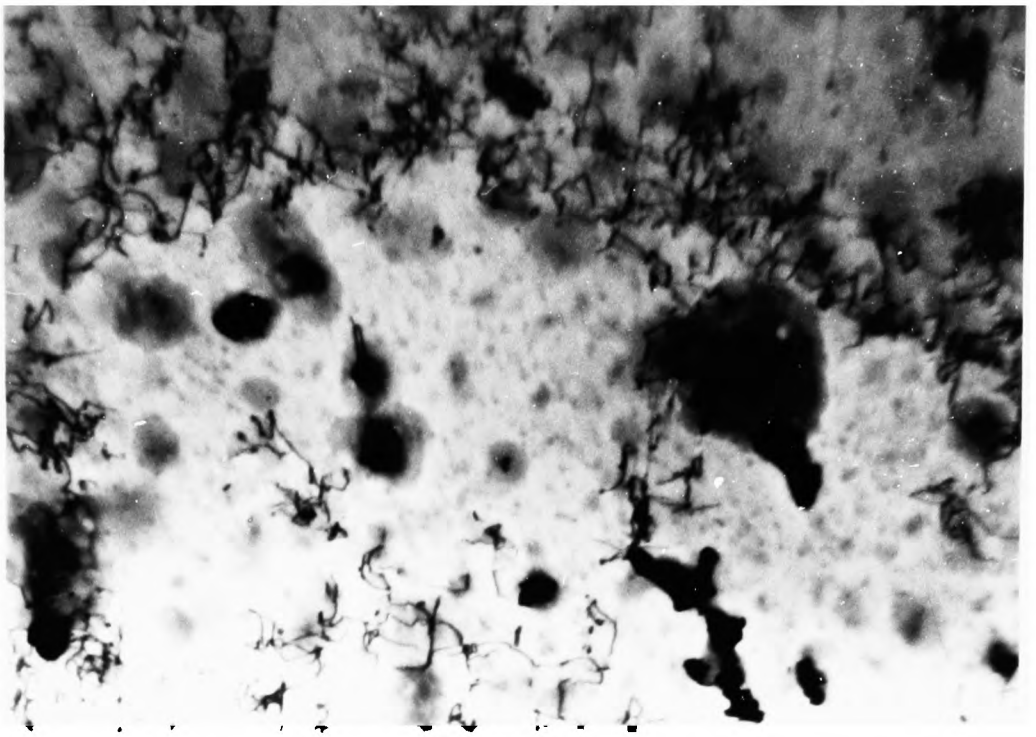

Figure 4.15

Large scale dislocation free cells in an area of plate B21.

1μm ⟵⟶

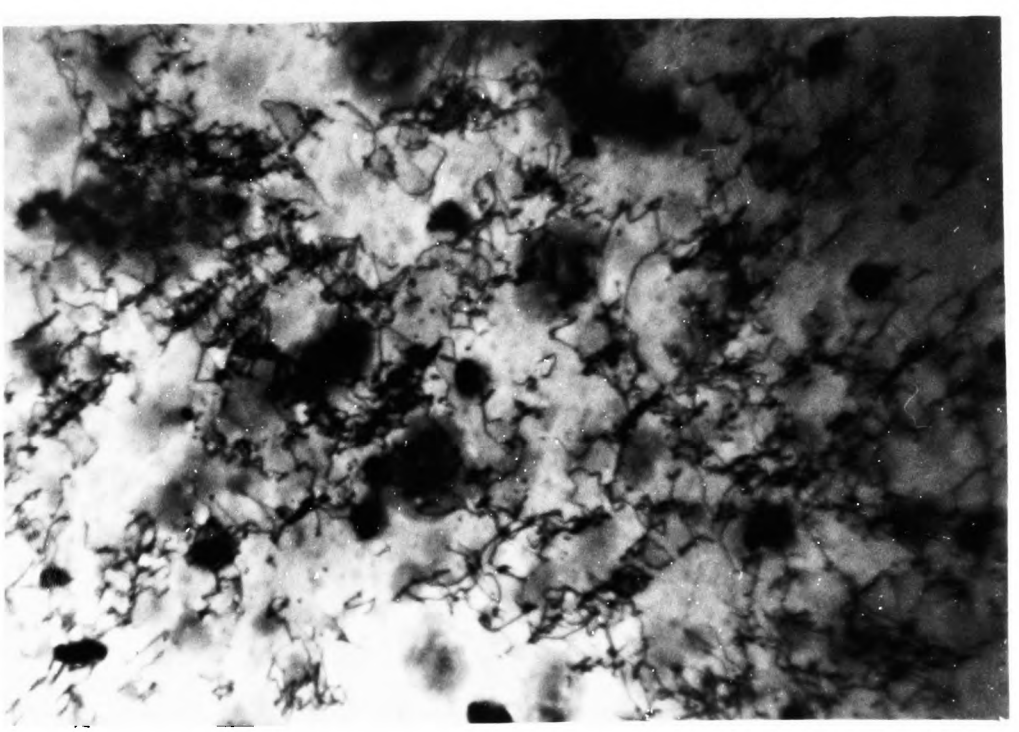

Figure 4.16

A different area in the same foil as for fig. 4.15, showing the mesh structure.

1μm ⟵⟶

plates, but considering the accuracy of the determinations the difference is small. There were no abruptly misoriented regions as in the B2 plates, but the deviation parameter, $s_g$, varied over an area of a few microns, indicating small local lattice tilts. Figure 4.17 shows a region of B31 for which the deviation parameter was varying sufficiently for the dislocations at the top to be out of contrast. The lower part of the micrograph shows the cell structure.

Plates from B4 showed a distinctive structure with broad bands of dislocation network separated by areas with no network structure. These intermediate areas contained loops, small isolated tangles and dislocation debris, as shown in figure 4.19, and had approximate dislocation densities of $3 \times 10^6 mm^{-2}$. The network structures were similar to the dislocation meshes observed in the B2 and B3 crystals, but were more open. The dislocation density in these regions of B4 was lower than in the other blocks, having an approximate value of $7 \times 10^6 mm^{-2}$. An area at the edge of such a band of dislocation network is shown in figure 4.18. Faint striations across the field of view are due to slip trace contrast. It was impossible to determine the full extent of each type of structure since the electron transparent areas of the foils were not sufficient to image a complete band. Because of the size of these 'thin' areas with respect to the dimensions of the foil and of the volumes investigated with γ-diffraction it was not possible to obtain a precise description of the dislocation structure responsible for each rocking curve.

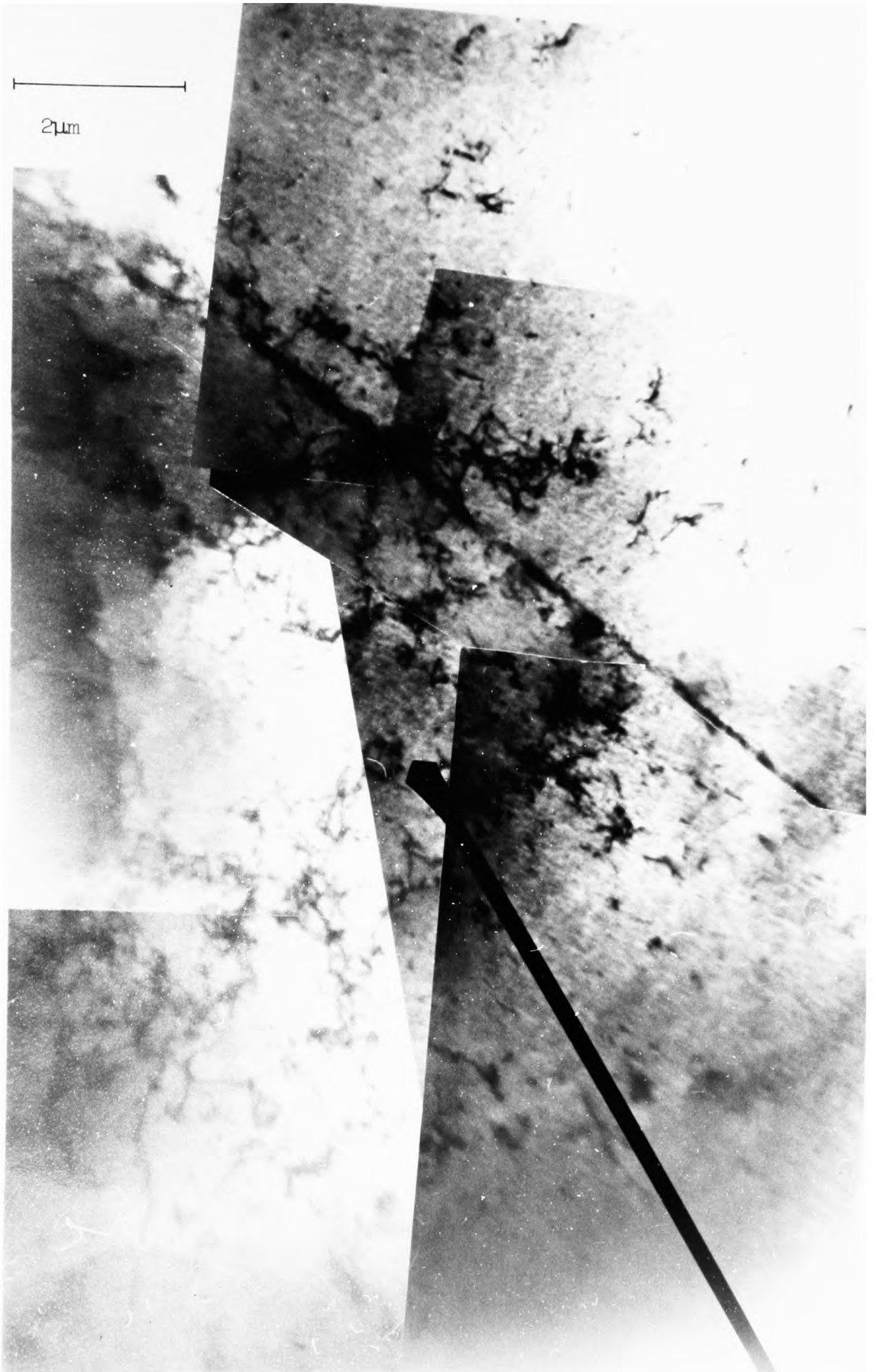


Figure 4.17

An area of B31 showing the cell structure and the variation in the deviation parameter across the foil.

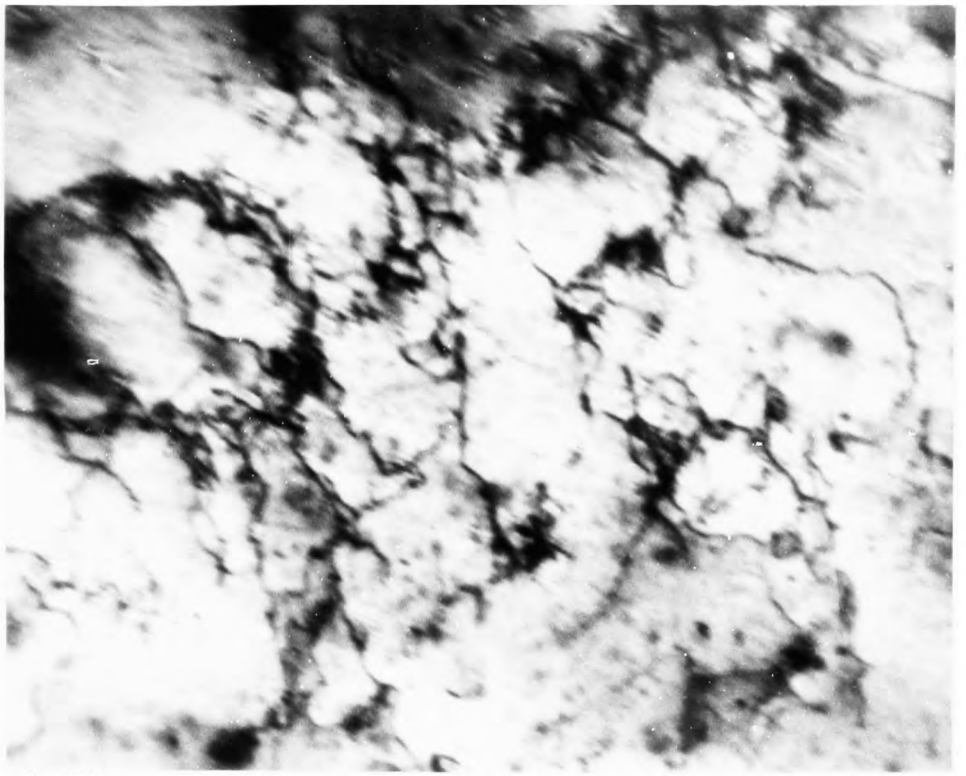

Figure 4.18

An area of mesh structure in platelet B42. The striations are due to slip plane contrast.

1μm

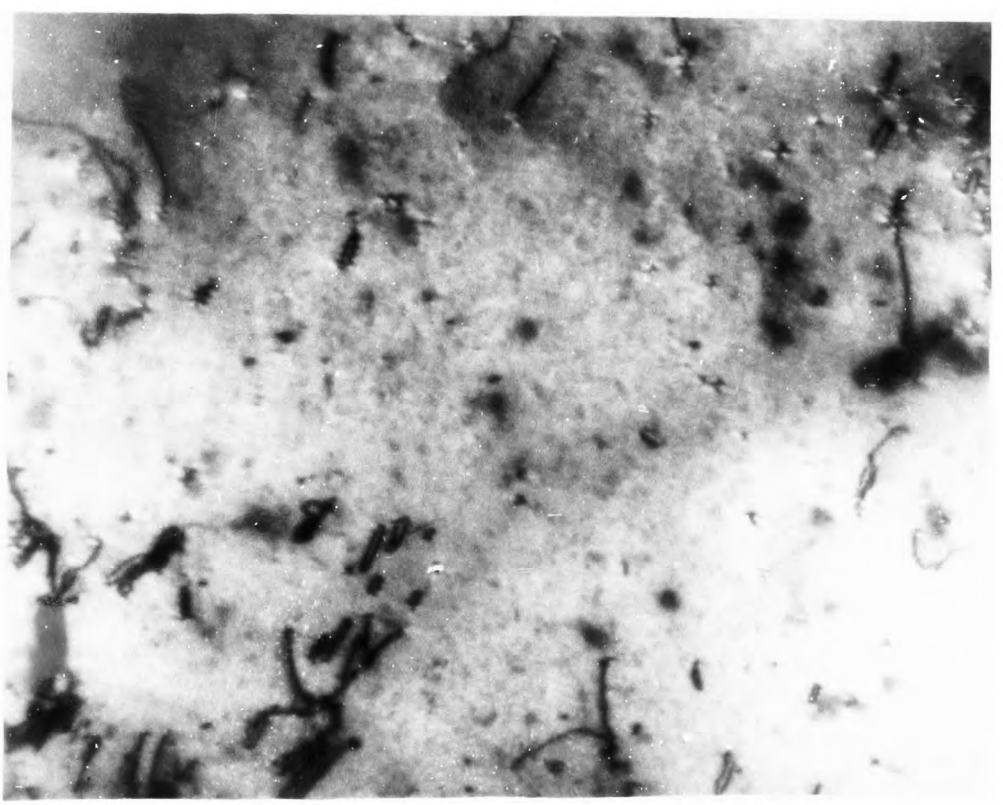

Figure 4.19

This shows a region adjacent to a band of mesh structure, and containing an assortment of short dislocations and loops. The foil was taken from platelet B42.

0.5μm

## 5. Neutron diffraction

The flat plate crystal PP4 described in chapter 3 was used for a series of measurements using the neutron diffractometer D13 at the Institut Laue Langevin (section 2.2). The results from these experiments were used to attempt predictions of the neutron diffraction properties of the crystal and also to test an equation describing the wavelength dependence of neutron absorption[71].

### 5.1 Experimental neutron measurements

The 111 and $0\bar{2}2$ reflections were used to record rocking curves in the central portion of each thickness of Crystal PP4, according to figure 5.1 with a beam of 5mm square section. Measurements were made at four wavelengths with the $0\bar{2}2$ reflection and five wavelengths with the 111 reflection, in the range 0.6 to 2.3Å. For each of the wavelengths the intensity of the transmitted beam, away from the Bragg reflecting position, was recorded as well as the intensity of the incident beam and the diffracted and transmitted rocking curves. In

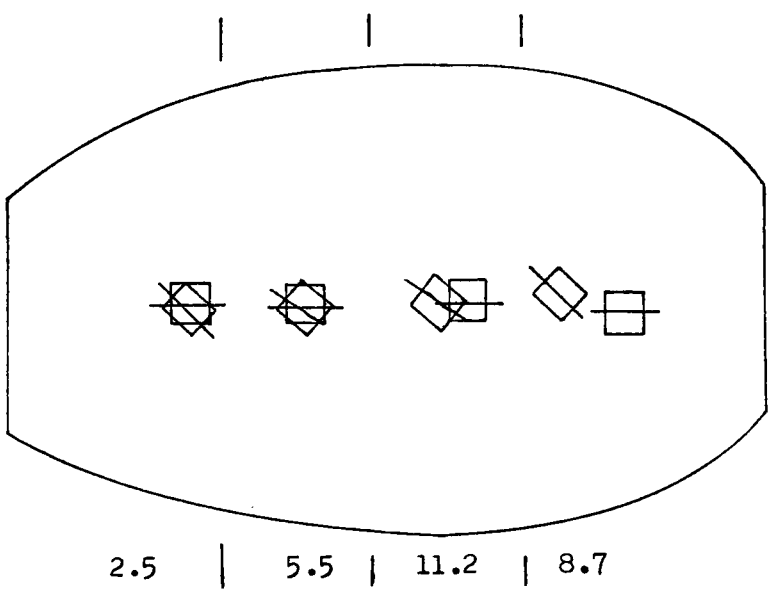


Fig. 5.1

The positions used for neutron measurements on PP4; for the 111 reflection (◇) and the $0\bar{2}2$ reflection (□). The bars are the positions of the γ-ray measurements (section 5.2)

some cases it was not possible to avoid exciting multiple reflections for which the tabulated data have been corrected. The peak and integrated reflectivities, the half-widths and the mosaic spreads derived from them are listed in tables 5.1, 5.2 (Appendix I).

Theoretical rocking curves calculated using these mosaic spreads in equation (2.24) are compared with the measured peaks for the $0\bar{2}2$ reflection, at wavelengths of 0.683, 1.08, 1.69, and 1.97 Å in a crystal thickness of 2.5mm, in figs. 5.2a and 5.2b which are both to the same intensity scale. Various attempts at fitting theoretical curves were made, but none was completely successful. The model used in deriving equation (2.24) is based on a Gaussian distribution for the orientation of mosaic blocks and this is not an accurate description of typical defect structures in deformed copper crystals. The data were not collected in a form readily adaptable to a computer analysis based on an anisotropic mosaic distribution, e.g. that of Becker and Coppens[31].

The peak reflectivities follow the general trend with increasing wavelength shown in fig. 2.10. The peak heights at about 2Å were smaller than those at wavelengths between 1.0 and 1.5Å for both reflections. The measured values showed an increase to a maximum peak reflectivity then decreased with increasing thickness as in fig. 2.8. However it was not possible to verify the thickness dependence since it depends on a constant mosaic spread throughout the crystal. It was found from a comparison of measured values with the theoretical predictions that the experimental reflectivities were about 20% greater than the values given by equation (2.24).

Theoretical reflectivities calculated using mosaic spread parameters derived from the neutron measurements were smaller than

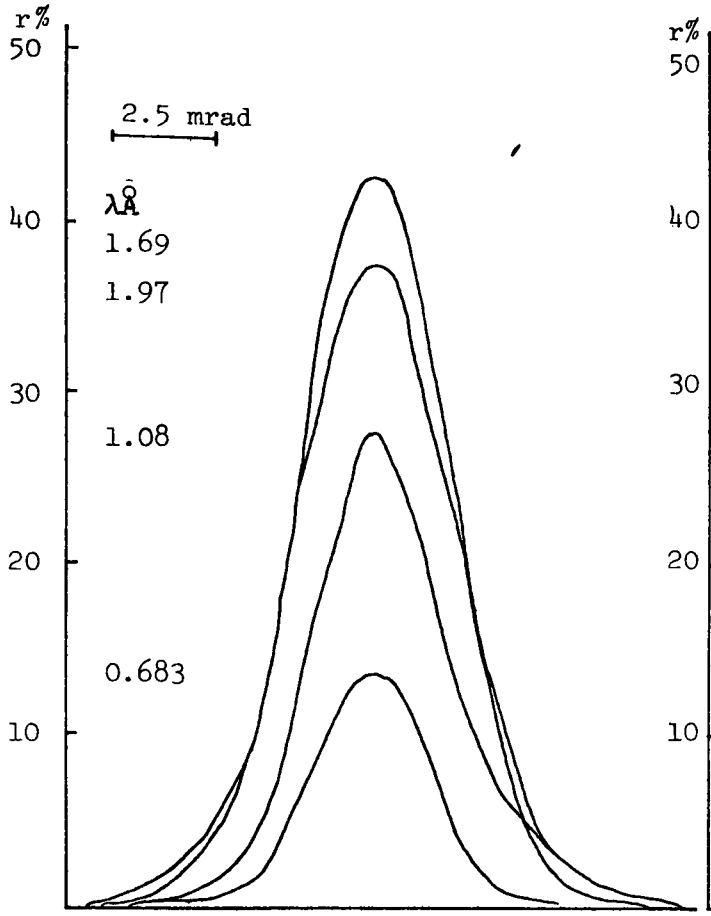


Fig. 5.2a

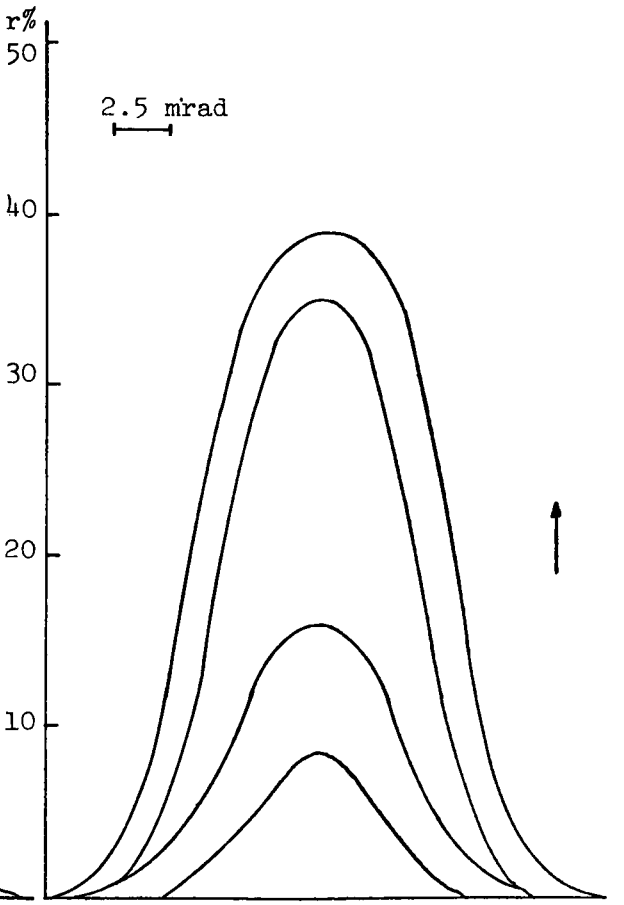


Fig. 5.2b

These figures compare theoretical and measured profiles for the $0\bar{2}2$ reflection in a 2.52mm crystal at wavelengths of 0.68, 1.08, 1.69, and 1.97Å. The wavelength increases in the sense of the arrows, except in fig. 5.2a where the peak height at 1.97Å is less than that at 1.69Å.

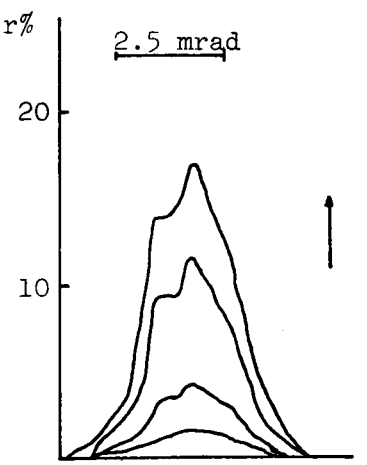


Fig. 5.2c

Fig. 5.2a gives the experimental curves, and fig. 5.2b was calculated using values of $\eta$ derived from these measurements. Fig. 5.2c shows theoretical profiles derived from $\gamma$-ray rocking curves recorded in approximately the same crystal volumes as used for the neutron experiments. The scales in figs. 5.2a and 5.2c are identical.

the measured values in all cases except the longest wavelengths. The half-widths of the calculated curves were greater, and the integrated intensities were about 5% smaller, than those measured. Matching peak intensities of experimental and theoretical curves gave theoretical half-widths narrower than measured. The form of the measured curves suggests larger mosaic blocks with less misorientation than would be consistent with the calculated profiles. The assumption of a Gaussian mosaic distribution implies a random distribution of dislocations and the nearest approximation to this in terms of a copper defect structure would be the cell structure observed in crystals deformed into stage III of the single crystal work hardening curve (section 1.5). Any more regular dislocation arrangement, e.g. slip bands, would restrict the validity of the Gaussian model.

The electron microscopical examination of PP4 showed that the surfaces of the thicker regions were more heavily deformed than the inner, or thinner, regions. This was caused by compressing the crystal in the form of a flat plate, since the large area of contact between the anvils and the crystal gave a highly constrained deformation with localised instabilities. On a microscopic scale this caused an inhomogeneous, non-random dislocation distribution.

In the 111 measurements, the secondary extinction coefficients increased to a saturation value with increasing wavelength. The saturation value was reached at a wavelength of about 2.5Å in all thicknesses. This behaviour is in agreement, qualitatively, with theoretical predictions of the wavelength dependence of secondary extinction[72].

## 5.2 Gamma diffraction measurements

γ-ray rocking curves were recorded in approximately the same crystal volumes as for the neutron measurements, using an incident beam of dimensions 10 x 1 $mm^2$ and the reflections 111 and $0\bar{2}2$. The results from the $0\bar{2}2$ measurements are shown graphically in fig. 5.3, and both sets of data are tabulated in table 5.3. The mosaic spread parameter was derived according to equation (2.4), and the theoretical integrated reflectivity is the kinematical value, proportional to QT. The secondary extinction coefficient, $E_s$, is a measure of the deviation from kinematical theory as given by equation (2.20). The Ewald sphere for radiation of 0.03Å wavelength is sufficiently large to satisfy several reflections simultaneously, especially when the diffraction profile is broadened due to deformation. The curves in fig. 5.3 show a subsidiary peak, possibly 200, to the left of the peak maxima. Normally parasitic reflections are eliminated by rotating the crystal about the scattering vector, but in this case the crystal shape made this impossible. The short wavelength of the γ-radiation makes the diffraction process more sensitive to small lattice distortions than the neutron wavelengths usually used, and the irregularities in the shape of the rocking curves are due to regions of crystal oriented to reflect strongly in that direction. The volume elements used for these measurements did not coincide with the volume used for the $0\bar{2}2$ mapping of section 3.1.1. The integrated intensities for the mapping curves were marginally smaller than those given here, and this was due to the parasitic reflection broadening the curves in the neutron-measured positions. The peak heights in the neutron measured positions were about 2% smaller than those recorded in section 3.1.1.

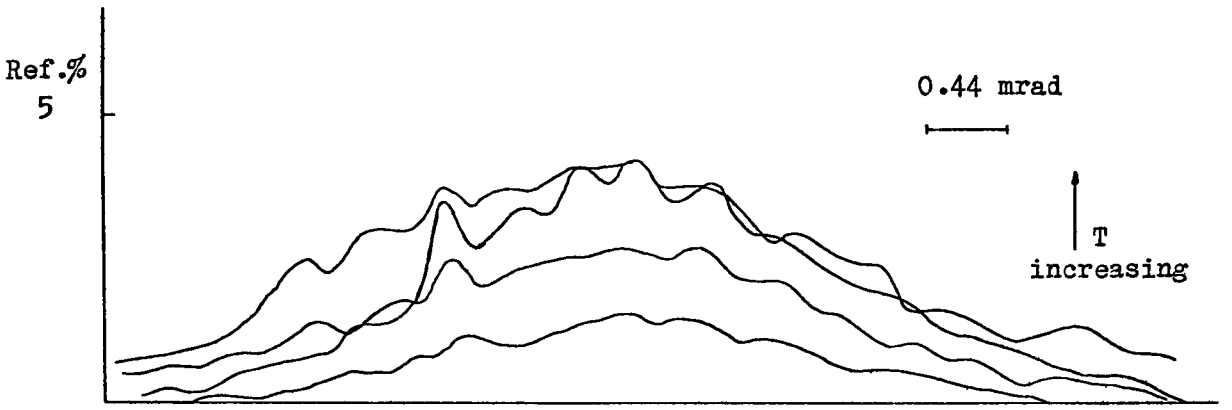


Fig. 5.3

$\gamma$-ray rocking curves recorded for the volumes in fig. 5.1 with the $0\bar{2}2$ reflection. The subsidiary peak is probably a parasitic reflection.

Table 5.3a

| T mm | $r_p$ % | $\beta$ mrad | $\eta$ mrad | $R_\Theta$ $10^{-5}$ | $R_k$ $10^{-5}$ | $E_s$ % |
|---|---|---|---|---|---|---|
| 2.5 | 1.59 | 2.18 | 0.926 | 3.553 | 3.931 | 9.59 |
| 5.5 | 2.80 | 2.84 | 1.20 | 8.232 | 8.518 | 3.35 |
| 8.7 | 4.34 | 2.91 | 1.23 | 10.55 | 13.60 | 22.42 |
| 11.2 | 4.34 | 3.34 | 1.42 | 13.78 | 17.52 | 21.33 |

Table 5.3b

| T mm | $r_p$ % | $\beta$ mrad | $\eta$ mrad | $R_\Theta$ $10^{-5}$ | $R_k$ $10^{-5}$ | $E_s$ % |
|---|---|---|---|---|---|---|
| 2.5 | 2.55 | 4.51 | 1.91 | 1.195 | 1.195 | - |
| 5.5 | 5.57 | 4.36 | 1.86 | 2.408 | 2.629 | - |
| 8.7 | 5.23 | 7.56 | 3.21 | 3.528 | 4.159 | - |
| 11.2 | 10.20 | 2.18 | 0.93 | 2.497 | 5.354 | - |

Table 5.3

Measured parameters from $\gamma$-ray rocking curves recorded in the volumes of PP4 used for neutron measurements. Table 5.3a has data for the $0\bar{2}2$ reflection and table 5.3b for the 111 reflection.

## 5.2.1 The use of γ-diffraction to determine neutron diffraction profiles

Within the limits of kinematic theory, the γ-diffraction measurements may be used to derive the mosaic distribution function numerically[73], and this may be substituted in the expression giving theoretical neutron reflectivities. In this way the detailed mosaic structure is included in the theoretical calculations. Rearranging equation (2.24) gives an expression for the mosaic distribution

$$W(\omega) = \frac{\gamma}{2QT} \ln\left(\frac{1}{1 - 2r_m(\omega)}\right) \qquad 5.1$$

which, since $W(\omega)$ is a probability function, leads to

$$\frac{2QT}{\gamma} = \int_{-\infty}^{\infty} \ln\left(\frac{1}{1 - 2r_m(\omega)}\right) d\omega \qquad 5.2$$

If equation (5.2) is satisfied to within a few percent (at most 30%) using measured reflectivities, $r_m(\omega)$, and replacing the integral by summation over all the steps in $\omega$ performed by the goniometer, then equation (5.1) gives the crystal mosaic function. The numerical values for $W(\omega)$ may then be used in equation (2.24), with the values of Q and γ applicable to neutron diffraction, to calculate neutron reflectivities.

$$r_n(\omega) = 0.5\exp\left(-\frac{\mu T}{\gamma}\right)\left(1 - \exp\left(-\frac{2QTW(\omega)}{\gamma}\right)\right) \qquad 2.24$$

The γ-ray measurements with the 111 reflection failed to satisfy equation (5.2); the profiles were broad and irregularly shaped, and the integrated reflectivity was significantly greater than the kinematical value. This was due to parasitic reflections, and such was the form of the curves that no corrections for multiple reflections were attempted. Neutron reflectivities were calculated using the γ-diffraction measurements of section 5.2 with the $0\bar{2}2$ reflection. The reflectivities were used in equation (5.1) to give $W(\omega)$, which

was substituted in equation (2.24) with the wavelengths and thicknesses used for the neutron measurements of section 5.1. The curves thus predicted are shown in figure 5.2c for a 2.5mm thickness. The order of magnitude of the disagreement between measured and calculated neutron curves was the same for all thicknesses. Inclusion of the parasitic reflection would adversely affect the predicted intensity of the neutron curves. The γ-diffraction measurements were not free from extinction, and the use of a reduced γ-reflectivity in equation (5.1) leads to a lower predicted neutron reflectivity.

Although γ-rays have similar penetration depths to those of neutrons, the volume examined by γ-rays is typically 20% of that irradiated by neutrons. The wavelength differences mean that the beam paths are different for a given reflection and, unless the crystal has a very homogeneous defect structure, the incident beams will be diffracted differently.

## 5.3 The wavelength dependence of neutron absorption

The total attenuation, $\mu_T$, of a neutron beam traversing a crystal is a function of nuclear absorption (neutron capture), coherent and incoherent scattering. As a first approximation to experimental results from the transmission of neutrons by perfect silicon crystals, Brugger[74] found

$$\mu_T = \mu_C + \mu_{FA}(1 - \exp(-2G)) \qquad 5.3$$

$$\mu_T = \mu_C + \mu_{FA}\left(1 - \exp\left(-\frac{Y\tau}{\gamma}\right)\right)$$

where exp(-2G) is the Debye-Waller factor describing thermal diffuse scattering and $\mu_C$ is the capture cross-section which is directly proportional to wavelength. $\mu_{FA}$ is the free-atom cross-section per unit volume and a material property. The factor Y is a material

constant including the Debye parameter, $B_D$, which describes the thermal vibrations of the lattice, and $\tau$ the absolute temperature.

$$Y = \frac{B_D}{\tau} \qquad 5.4$$

Using published values for $B_D$[75], theoretical curves for the variation of $\mu_T$ with increasing wavelength were calculated for beryllium, copper, silicon and germanium at room temperature. These are shown in figure 5.4a and were published with similar curves for various temperatures by Freund[71]. It can be seen from these curves that, for all but the shortest wavelengths, beryllium monochromators have much better transmission properties for neutrons than copper or germanium. Although silicon has better transmission than beryllium, the optimum thickness, as defined in section 2.2.2, is an order of magnitude greater than that for beryllium, and the optimum silicon monochromator would be very bulky.

Attenuation curves calculated for copper, using values of $B_D$ from International tables[75], at 93K and 20K are given with the room temperature curve in figure 5.4b (curves $\mu_{93}$, $\mu_{20}$ and $\mu_{290}$ respectively). The curve for copper at room temperature, $\mu_{290}$, was calculated using a value for the Debye parameter, $B_D$, of 0.573[76]. The curve $\mu_M$ was calculated using a value of Y derived from the measurements of section 5.1. The results from the transmission measurements are shown as open circles on the curve $\mu_M$, and the values of Y used for the curves are given in table 5.4. When a monochromator has been selected for its d-spacing and mosaic spread, there may be some advantage in maintaining it at low temperatures to improve the intensity of the monochromatic radiation.

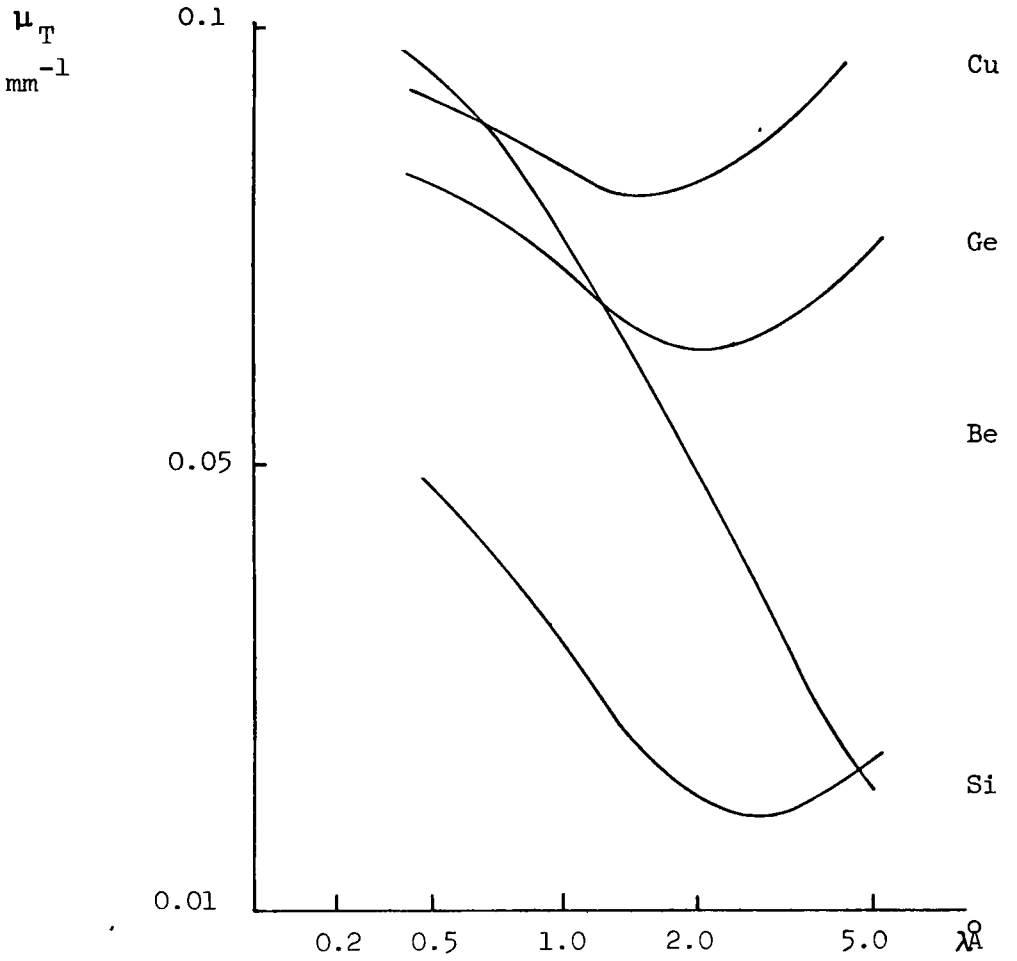


Fig. 5.4a.- Theoretical absorption curves as a function of wavelength for copper, germanium, silicon, and beryllium at room temperature.

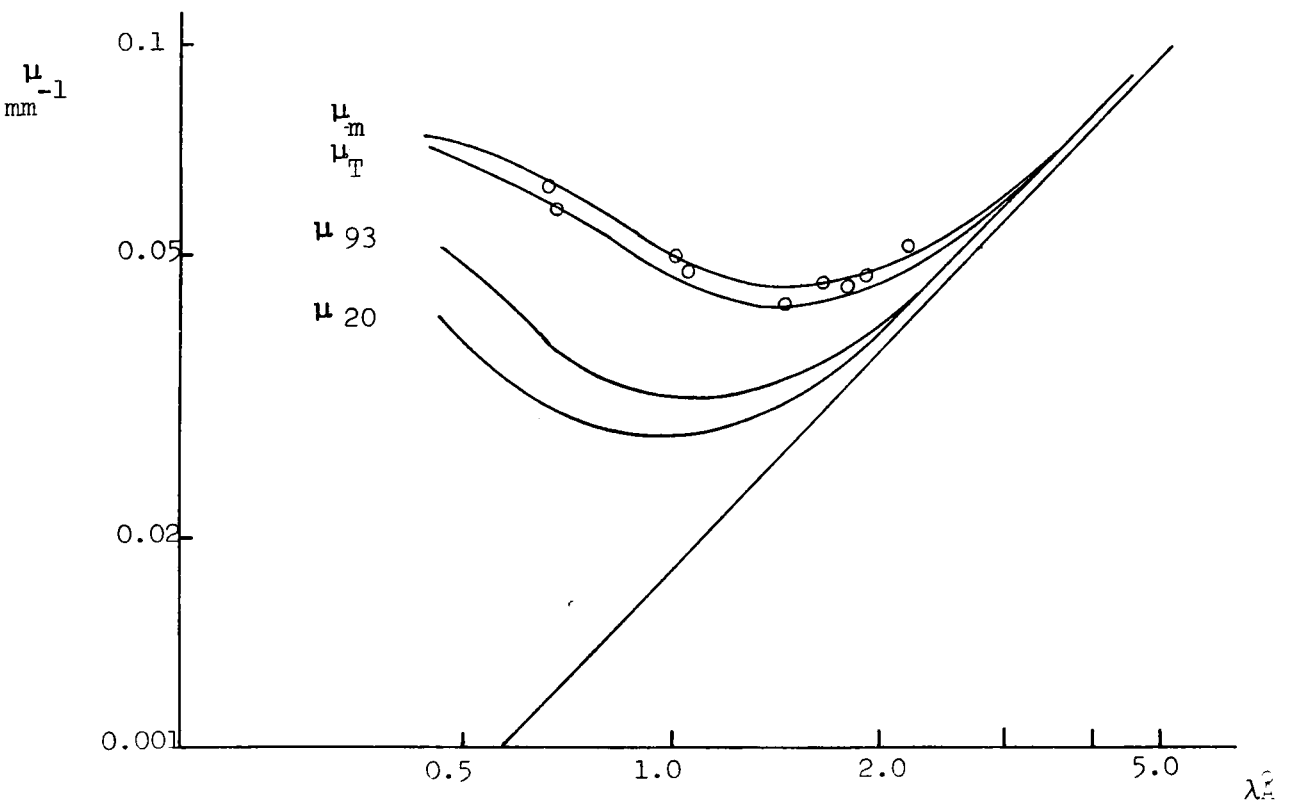


Fig. 5.4b. Theoretical absorption curves as a function of wavelength and temperature for copper.

| Material | Be | Si | Ge | Cu | Cu | Cu | Cu measd. |
|---|---|---|---|---|---|---|---|
| $\tau$ K | 290 | 290 | 290 | 20 | 93 | 290 | 290 |
| $Y / 10^{-3}$ | 1.31 | 1.18 | 2.32 | 0.51 | 0.78 | 1.97 | 2.30 |

Table 5.4

The range of published values for the Debye temperature and parameter for copper is considerable, and taking the average value from this range gave a worse fit at lower wavelengths since it led to higher theoretical absorption factors. A better fit is not dependent entirely on adjustment of the parameter Y; at longer wavelengths a large part of the total attenuation is due to inelastic scattering processes which have a direct wavelength dependence.

## 6. Discussion

Although many possibilities have arisen from this research, the discussion has been restricted to the interaction of the defect structure in deformed copper single crystals with γ-rays and neutrons, with particular reference to neutron monochromators.

The original intention was to use typical flat plate monochromator crystals to test the neutron diffraction equations of Bacon and Lowde[17], so the expressions for optimum crystal thickness and reflectivity were derived from them. In designing a monochromator for a given system it is useful to know the optimum theoretical performance of a particular material and the degree to which this may be achieved in practice. The γ-radiation has similar absorption coefficients to neutrons, and with its shorter wavelength, frequently complies with the assumptions of kinematical theory. Being more sensitive than neutron radiation to small crystal lattice defects, γ-ray diffraction made a convenient way of studying the crystal defect structure. However it was necessary to attempt a definition, in terms of defect structure, of the diffraction theory parameters used to describe the deformed crystal.

Although in principle γ-ray diffraction may satisfy kinematical theory, the defect structure in all the flat plates examined was such that the criteria of this theory were not well satisfied. However in some cases with the weaker reflections the measured integrated reflectivities had values within a few percent of the kinematical value. The value of $T_o$ in Zachariasen's parameter A, (equation (2.1)), should be interpreted as the depth at which the intensity of the incident radiation is totally transferred to the diffracted beam. A primary extinction length may be defined as that thickness of crystal for which

A is unity, which in copper with γ-rays is about 180 μm for the 220 reflection and about 130μm for the 111 reflection. The electron microscopy examination of the crystals revealed relatively dislocation free areas of dimensions large with respect to these extinction lengths, so the diffraction was not free of primary extinction. Assuming values of A between 0.2 and 0.8 in the primary extinction correction factor, (equation (2.18)), it was possible to calculate integrated intensities approximately equal to the measured values using kinematical equations. These values of A correspond to mosaic block dimensions of between 15μm and 75μm depending on reflection and degree of extinction. Where the discrepancy between measured and uncorrected kinematical integrated intensities was greatest, the necessary correction factor yielded mosaic block dimensions of 50 to 75μm. Dislocation free areas with dimensions of at least 50μm were observed in the central regions of the plates and areas of dimensions from a few microns up to this value were observed throughout the plates. Averaging the observed dimensions over the plate thickness would give a value within the range of mosaic block dimensions derived from the correction factors necessary to equate kinematical and measured integrated reflectivities.

The use of more explicit expressions, e.g. theoretical equations derived from the basic assumptions of kinematical theory and including the effects of extinction and experimental parameters such as incident beam divergence[72], gave better agreement with measured values in some cases and worse agreement in others. A unified theoretical approach giving reasonable agreement in all, or most, cases was not found. The theoretical equations tested were all based on Gaussian mosaic

distributions, but gave slightly different behaviour of the integrated reflectivity as a function of thickness and mosaic spread. Figure 6.1 shows integrated reflectivities calculated according to an expression given by Bogdanov and Menshikov[72] and those calculated from equation (2.15) for the 220 reflection.

In all theoretical calculations relating to Y-ray measurements the measured half-width, $\beta$, was taken to be the standard deviation, $\eta$, of the mosaic spread function. This was not strictly justified since the diffraction process did not satisfy the 'thin crystal' approximation of kinematical theory. Also since the recorded rocking curves were irregularly shaped and often had more than one distinct peak, the definition of $\beta$ in each case was open to error.

The effective absorption coefficient, $\mu_e$, can be determined from the slope of a graph of $\ln(^R/T)$ versus T, and from the effective absorption coefficient an estimate of the secondary extinction coefficient, jQ, may be obtained. A straight line relationship between $\ln(^R/T)$ and the crystal thickness depends upon a constant mosaic spread at all thicknesses, and in the stepped plates this was not the case. The estimate of secondary extinction, $E_s$, given in the tables of results was obtained from the deviation of the measured integrated intensity from the kinematical value for each volume element. An average value for each thickness of crystal was not obtained, although some regions were more uniform than others.

The failure of the flat plate crystals to conform to theoretical predictions was due to the defect structure not having a Gaussian orientation distribution about a mean value, and not being uniform throughout the crystal. This was because the crystal was deformed

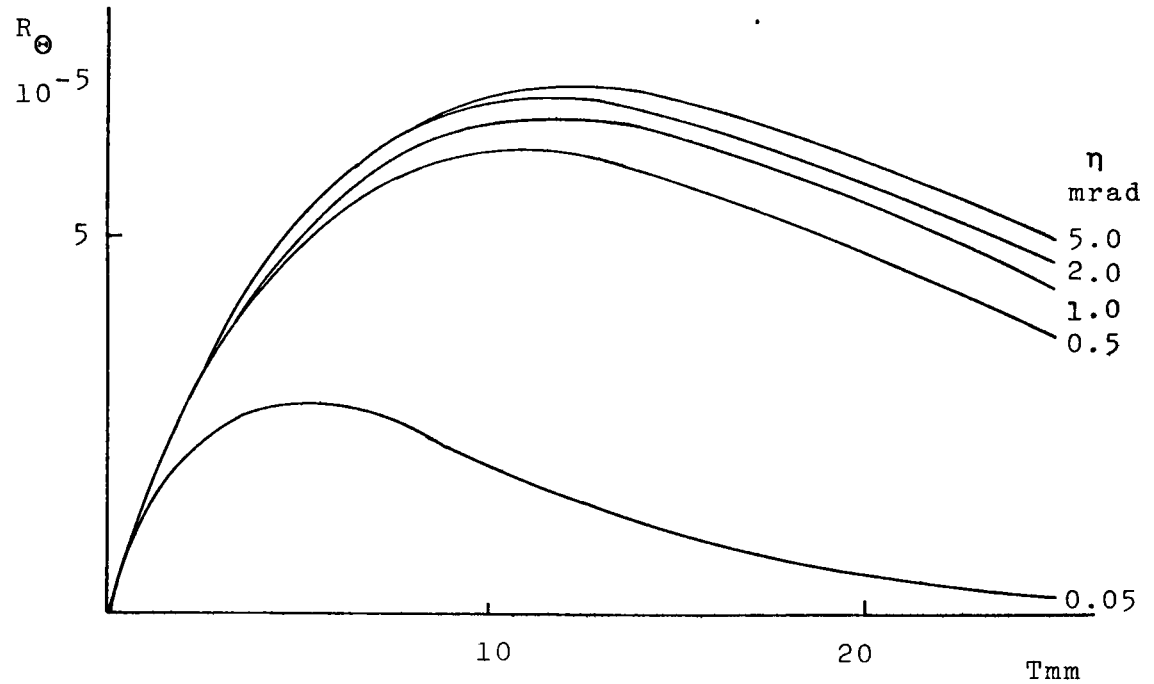


Figure 6.1a

γ-ray integrated reflectivities for a selection of mosaic spreads and the 220 reflection, calculated using equation (2.15).

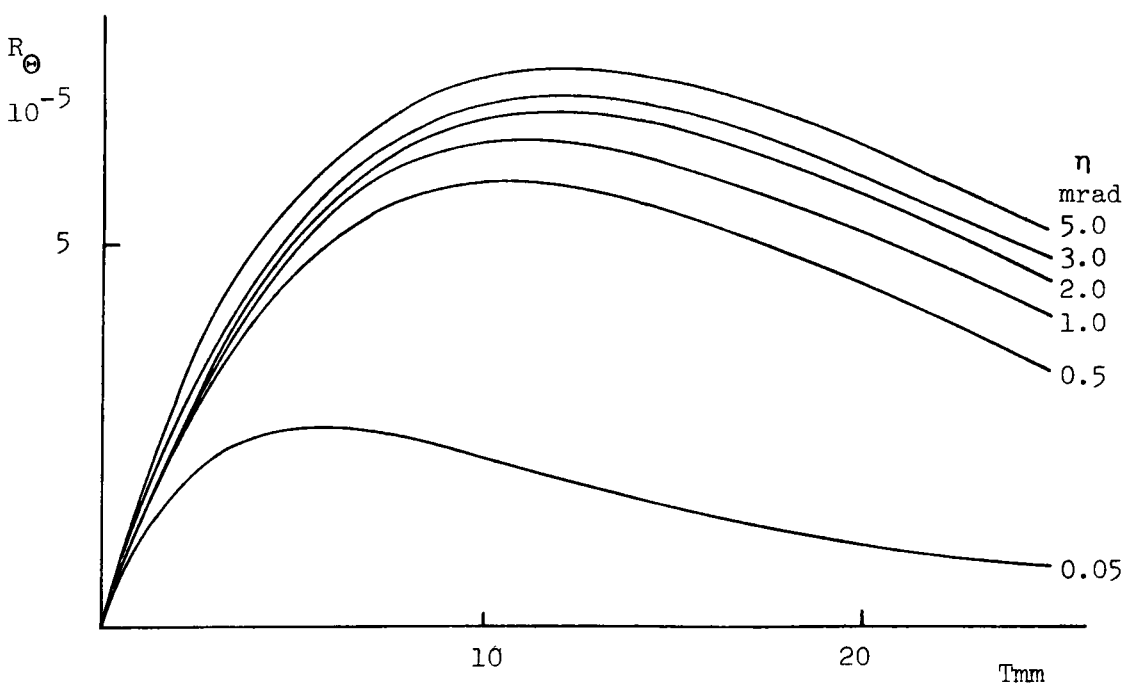


Figure 6.1b

The variation of integrated reflectivity with thickness for several mosaic spreads, calculated for the 220 reflection and γ-rays using an expression published by Bogdanov and Menshikov[72].

as a flat plate in compression along the shortest axis, which is geometrically a worst case since crystal-anvil contact causes considerable frictional effects transmitted through the plate. As none of the crystal plates had a uniform structure throughout, and even in individual volumes the mosaic spread could not be described by a Gaussian function, it was not possible to verify the figures of sections 2.1 and 2.2.

The conclusions drawn from the theoretical study were, that to have a large integrated intensity and a high peak reflectivity simultaneously the mosaic spread, $\eta$, for $\gamma$-rays would need to be of the order of 2 or 3mrad to give satisfactory results with the stronger reflections. A crystal thickness of about 10mm would be suitable for both $\gamma$-ray and low wavelength ($<1\mathring{A}$) neutron diffraction. However a thickness of about 5mm is better for a range of longer neutron wavelengths while still being adequate for $\gamma$-ray work. This is assuming $\eta$ is the absolute value of mosaic spread, i.e. dependent only on the defect structure and not on the means of measuring it.

Taking the values of mosaic spread parameter derived from the $\gamma$-ray measurements, the corresponding measured peak reflectivities were frequently greater than the theoretical values calculated using equation (2.21). This tendency was also observed in the results from the neutron experiments. (Tables 5.1, 5.2 - Appendix). The explanation rests with a non-Gaussian distribution of mosaic blocks, which in the case of these crystals has the physical interpretation that regions of perfect crystal constitute a larger proportion of the total volume than is consistent with a Gaussian function. This would imply a certain amount of primary extinction as well as

secondary extinction. The optical and electron microscopical observations of coarse slip bands forming boundaries to relatively dislocation free areas would fit this description.

Assuming an optimum mosaic spread to be between 2 and 3mrad, of the plates with step configuration, PP3I and PP3II were insufficiently deformed and PP4 was overdeformed. The discrepancy between the average FWHM measured for the whole crystal after the final loading and the values measured after cutting into step configuration is probably due to a surface layer of damage caused by crystal-anvil contact. When the crystal had been cut approximately 0.5mm was removed from the entire surface to eliminate spark machine damage. Even when this had been done, electron microscope foils taken from the surface of the thickest regions showed a dense cellular dislocation structure corresponding to heavy deformation. The γ-maps recorded in the unstepped plates included a broadening due to this damaged layer which was absent in the cut crystals.

It was hoped to establish a correlation between γ-ray and neutron experiments, following a theory by Schneider[73], as outlined in sections 5.2 and 5.2.1. However the theory only holds for crystals which satisfy kinematical diffraction requirements, and among the copper crystals available at the I.L.L. such crystals were infrequently found. Schneider was able to show qualitatively[35] that due to the size of typical neutron-irradiated volumes, spatial averaging occluded the effects of double or multiple peaks, i.e. the monochromatic neutron beam could be 'missing' components corresponding to the angular positions of the reduced intensity between multiple peaks. This was shown in figure 5.2a and 5.2c where the irregularities of the γ-measured curves

are smoothed out in the neutron case. In all cases of a double peaked γ-ray rocking curve the corresponding neutron curve had a single peak.

No conclusions with respect to the reflectivities or extinction effects of neutron diffraction could be drawn because it was not possible to obtain a set of measurements at constant mosaic spread. Sets of measurements on other copper crystals were equally unsatisfactory for the same reason. However the measured transmitted intensities, recorded at position away from the Bragg reflection, gave linear plots of $\ln(P_T/P_o)$ against thickness, from which absorption coefficients were obtained. These were used to test Bruger's equation (5.3) which was originally derived for thermal neutron filters of single crystal silicon, which would reduce the size of instrumental shielding by absorbing fast neutrons and gamma radiation while passing neutrons of thermal energies. The measured values were in reasonable agreement with this expression, which was also used with published values of the relevant parameters to predict the absorption behaviour of other possible monochromator materials, and to estimate the effects of temperature on them. Some reasonably successful experiments were performed using copper crystals in a cryostat of liquid nitrogen.

Table 6.1 lists values of total absorption coefficient, $\mu_T$, parameter Q (a measure of the scattering power), optimum thickness $T_{opt}$, (ch.2) and the peak reflectivity corresponding to this thickness, for a mosaic spread of 2.5mrad in copper, silicon, germanium and beryllium at various wavelengths. The table was prepared using the equations of chapters two and five for Laue geometry.

| material & reflection | | A | 0.5 | 1.0 | 1.5 | 2.0 | 2.5 |
|---|---|---|---|---|---|---|---|
| Be | | | 0.731 | 0.298 | 0.147 | 0.086 | 0.057 |
| Cu | | $\mu$ | 0.700 | 0.470 | 0.412 | 0.436 | 0.490 |
| Ge | | $mm^{-1}$ | 0.398 | 0.250 | 0.184 | 0.170 | 0.175 |
| Si | | | 0.084 | 0.036 | 0.021 | 0.016 | 0.015 |
| Be | 002 | | 3.881 | 16.0 | 38.1 | 74.1 | 134.0 |
| Cu | 200 | $Q$ | 1.870 | 7.71 | 18.3 | 35.6 | 64.1 |
| Ge | 220 | $10^{-4}$ | 0.651 | 2.667 | 11.93 | 11.93 | 20.68 |
| Si | 220 | $mm^{-1}$ | 0.200 | 0.822 | 1.94 | 3.72 | 6.534 |
| Be | 002 | | 7.92 | 5.45 | 3.31 | 1.97 | 1.11 |
| Cu | 200 | $\bar{t}_{opt}$ | 10.2 | 7.15 | 4.24 | 2.42 | 1.33 |
| Ge | 220 | $mm$ | 20.10 | 16.9 | 7.49 | 7.17 | 4.32 |
| Si | 220 | | 8.78 | 7.78 | 5.08 | 3.11 | 1.80 |
| Be | 002 | | 17.5 | 39.9 | 46.8 | 43.8 | 49.5 |
| Cu | 200 | $r_p$ | 11.2 | 29.6 | 38.6 | 42.4 | 44.6 |
| Ge | 220 | % | 7.67 | 25.0 | 41.1 | 41.6 | 44.2 |
| Si | 220 | | 10.3 | 32.9 | 43.1 | 44.3 | 46.7 |

Table 6.1. Theoretical neutron diffraction parameters for beryllium, copper, germanium and silicon at reflections corresponding to similar lattice spacings and for a mosaic spread of 2.5mrad.

From figure 5.4a and table 6.1 it can be seen that silicon appears to have many advantages as a monochromator material. It is relatively inexpensive to obtain and is available as large perfect single crystals. The major disadvantage is that the optimum thickness at low wavelengths requires a lot of material. Beryllium combines high reflectivity

with relatively small monochromator dimensions and especially good behaviour at short wavelengths. The disadvantages lie in the availability of suitable crystals and in the health hazards of handling them. If the problems of producing a controlled and uniform mosaic spread could be overcome, it could be an ideal monochromator. Germanium shows no advantages over silicon as a monochromator and is used for the values of its d-spacings. Copper is on a par with beryllium at low wavelengths, and has better reflecting properties than germanium and silicon at all wavelengths, but relatively large crystals are required and the absorption is high. Large copper crystals are readily available in a nearly perfect state, but practical difficulties remain in producing the required mosaic spread.

6.1. The large flat plate crystals

Since a common monochromator geometry is a flat plate, the investigation of monochromator behaviour began with such crystals. Given this restriction on shape and the physically large scale required for neutron experiments, an obvious way of introducing a defect structure throughout the crystal was by compression along the plate normal. The inhomogeneities in the defect structure were due primarily to this means of introducing defects. Such was the size of the crystals that even in tension rectangular plates would not produce a uniform microstructure. Optical micrographs of small flat plates of copper (45 x 5 x 2mm), deformed in tension to various degrees at multiple slip orientations by Takeuchi[48] indicated that the microstructure varied through the crystal.

The initial plate thicknesses were cut to approximately the

optimum thickness for γ-ray measurements. The mapping was intended to set standard values of $R_\Theta$, $r_p$, and η for the crystal, but due to the inhomogeneity of the deformation structure approximate values for given volume elements had to be established instead. The majority of flat plate crystals deformed as potential monochromators showed similar γ-maps, i.e. a good monochromator was a chance event using these techniques. The γ-ray experiments on the step-configuration crystals indicated that the structural inhomogeneity was a function of depth as well as translational position in the crystal.

The average FWHM measured in the deformed plates increased linearly with applied load up to about 50MPa. This was observed in most of the flat plates deformed in the same way, but the gradient of the line varied from crystal to crystal. Since there was some evidence for a linear relationship between applied stress and the square root of the dislocation density, ρ, it was hoped that crystals deformed within the linear relationship, i.e. having a $\rho^{\frac{1}{2}}$ dependence might have uniform mosaic spreads. However it was obvious from the γ-maps that this was not the case, the double peaks appeared with the first loading. Such rocking curves indicate that two distinct orientations satisfy a particular reflection at very slightly different angular positions. With an [011] deformation axis the primary, (111), and conjugate, $(\bar{1}11)$, slip systems are equally stressed, with active slip directions $[\bar{1}01]$, $[1\bar{1}0]$ on (111), and [101], [110] on $(\bar{1}11)$. The dislocations on these slip systems cause tilts on the scattering planes, and the net result of these tilts is an angular spread around two distinct scattering directions which are both close enough to the Bragg angle to satisfy the conditions for reflection. The characteristics of

the double peaks and their separations are dependent both on the amount of slip on the two systems and on the incident beam direction. Various combinations of slip on the two systems may thus give rise to double peaks, peaks broadened to one side or uniformly broadened peaks. Inhomogeneities of this type, known as deformation textures, are found in cold-rolled or compressed metals, and are due to local instabilities in slip. A significant contribution to the instabilities is caused by frictional effects between the platen and the crystal being deformed.

The defect structure observed by electron microscopy were consistent with observations of dislocations in copper single crystals deformed in tension and compression [eg.55,49,51,54] by various experimentalists. The dislocation arrangements found in the plate crystals agreed well with those observed in copper crystals deformed into stage II of the tensile work hardening curve. The structures in the central layer of the crystal corresponded to lower strains than those nearer the surface, in agreement with stress fields proposed for materials deformed as plate or sheet[68]. Published micrographs of crystals deformed into stage III[55] show a much denser arrangement of dislocations than observed in the flat plates, with the exception of the cells in the surface layers of the thickest regions. There are two possible causes of this denser structure; the frictional crystal-anvil contact and/or the remains of spark machine damage. The plates were cut from the parent crystal using a coarse setting which may have resulted in more damage than the 0.5 mm layer removed in acid. The frictional contact during compression would have exacerbated the damaged surface layer.

Dislocation braids containing bundles of dislocations aligned parallel to slip plane traces are a common feature of deformed copper single crystals. Kawasaki[55] reported pairs of parallel bundles in braids in crystals oriented for double slip, and cell structures with walls more or less parallel to slip planes. In experiments with crystals oriented for multiple slip, Gottler[52] observed cell structures without preferred orientation separated by walls which contained dislocations of all Burgers vectors with equal frequency. Those were very similar to the microstructures of the more deformed rectangular blocks. In double slip crystals deformed into stage III, Steeds[54] reported very strongly misoriented bands, rotated with respect to the matrix by $25^{\circ}$ to $30^{\circ}$ about a $[1\bar{2}1]$. These misorientations were considered to be due to grip effects since the rotation was in the opposite sense to that which rotates the crystal axis to the tensile axis. They correspond to the effect in compression causing the multiple peaks recorded by $\gamma$-diffraction, although the rotations in the flat plates were less.

In order to make a more direct comparison with work hardening theories various workers [53,66], used irradiation with fast neutrons to pin dislocations in the stress-applied state. For foils with <111> normals, dislocations with Burgers vectors inclined to the plane of the foil may slip out, leaving networks with predominantly Lomer-Cottrell dislocations. Evidence was also found[51] for the loss of dislocations during the preparation of foils from crystals which had received no, or low, doses of irradiation. Arguments against the need for pinning were put forward[54], based on the similarity and repeatability of dislocation densities and arrangements in various foils of different

orientations. In all the {111} oriented foils examined from the flat plates and rectangular blocks there was an almost complete absence of dislocations in regions of foil less than 2500Å thick, and frequently on passing from thicker to thinner areas the network structures 'thinned out'. Thus there may be a case for pinning dislocations in foils which are to be cut parallel to the primary slip planes.

6.2 The rectangular block crystals

Investigations on the compression of f.c.c. crystals[50] indicated that the heterogeneity of deformation occurring during easy glide was dependent on the height to width ratio of the specimens, since as this ratio was decreased so did the amount of easy glide until, for cubic specimens of all pure materials, it was entirely absent. Thus for the flat plate crystals, in which this ratio had a value of 0.15, an inhomogeneous defect structure would be expected. To obtain a more regular defect structure rectangular blocks with various multiple glide orientations and height to width ratios in the range 2 to 2.5 were deformed in compression. In terms of a suitable defect structure for a monochromator, the best axial orientation was <111> in crystals with a height to width ratio of 2.25, and these are the crystals described in this text.

The block crystals were deformed to a range of applied loads which gave a small, an intermediate, and two very large strains. The lowering of the temperature at which the blocks were deformed caused a very rapid increase in the measured rocking curve half-width for a given load at a given strain rate, and such sensitivity to applied load is a disadvantage in preparing controlled mosaic spreads. The dislocation density and arrangement in the block strained by 2.7% at low temperature did not show any better reflecting properties for γ-rays or neutrons than the crystal receiving the same strain at room temperature. Neutron

measurements on the block deformed under liquid nitrogen were virtually impossible due to the low reflectivity. Consequently all other blocks were deformed at room temperature. There appeared to be an approximately linear relationship between strain and the γ-measured FWHM, the slope of which was dependent on the block dimensions and the reflections used.

In terms of an optimum mosaic spread of 2.5mrad, the 0.48% strain received by one block was insufficient. Since the measured FWHM depends on the reflection used, a small range of values around the optimum value is required, and a strain of about 1.5% seems to satisfy this for these blocks. The highest strain was too great and resulted in very broad rocking curves with a low peak reflectivity, which are of no use as monochromators.

The angular position of the FWHM in the deformed crystals did not appear to depend on that in the undeformed crystals, as shown in figures 3.15 and 3.16. In symmetrical Laue geometry the angular position of the maximum intensity occurs at the exact Bragg angle for a perfect crystal. The angular origin of the measured peaks was taken at a given distance to one side of the maximum intensity of one rocking curve recorded in each crystal, and this value was set for that reflection in that crystal. Although the absolute position of the peak maximum could not be recorded, the relationship between the angular positions of the peaks, and the variations in this on deformation, were obtained. The centres of gravity of the measured curves may be derived from the data, and where the deviation of this parameter follows a regular deviation from its initial angular position, in a sequence of rocking curves, a simple curvature of lattice planes may be defined. However for the block crystals the centres of gravity oscillated about a mean value which indicated no smooth bending had resulted from the deformation.

The γ-ray rocking curves recorded in the ends of the blocks after deformation showed similar irregularities in shape as those observed by other workers in smaller blocks of copper using x-rays[66]. Again this is due to frictional effects between crystal and anvil as described earlier. The barrelling of the block sides indicated that these effects were not negligible, and analysis of the slip lines on the faces of the blocks showed that strongly inhomogeneous slip had taken place in about two thirds of the crystal volume. Only a small central region appeared to show relatively uniform slip lines. From the slip line analysis it was only possible to say which slip systems were operating since the lines were of irregular length and spacing. As the central regions of each block appeared to have the most uniform defect structure, the small plates were cut from these parts. The FWHMs in these small plates had the same values as in the blocks, allowing for some rotation about the scattering vector between the sets of measurments. This suggested a degree of uniformity in the dislocation arrangements throughout the central volume of the blocks which was not observed on the scale of the electron microscope investigations. The γ-ray rocking curves measured in adjacent volumes of the B1 plates were extremely sensitive to localised arrangements and densities of dislocations. The major drawback with TEM studies is the extremely small volume of crystal examined, and where the dislocation density is low, the accuracy of any correlation between density or arrangement of dislocations and measured diffraction properties is negligible. The correction necessary to give agreement between measured and kinematical integrated intensities predicted areas of perfect crystal with dimensions of greater than 85μm.

This was not the distance between dislocations in the B1 plates, but there were very large regions of low dislocation density. In a qualitative sense this agrees with the theory if perfect is not synonymous with dislocation-free. In all the small plates such qualitative agreement could be found; broad profiles corresponded to mesh or cell structures in the dislocation arrangement, but there was no obvious relationship between FWHM and dislocation density. Nor was there an average cell size to which the diffraction properties could be related. The implications of the electron microscopy and γ-diffraction measurements were that the FWHM is not only sensitive to the dislocation density per se, but to its arrangement in a larger scale structure than is readily observeable on the electron microscope.

The possibility of γ-ray topography, using the same γ-ray source as the diffractometers, was investigated, but the resolution would be, at best, 10μm. Although much larger crystals could be used than with x-ray topography, the overlap of images in the deformed crystal would make interpretation of topographs difficult. X-ray topography in conjunction with electron microscopy may be a better approach to determining the structure responsible for the various diffraction parameters. X-ray topography has already been applied[79] to extended regions of nearly uniform lattice curvature produced by a local excess of dislocations of the same sign, and two dimensional arrays parallel to a slip plane or perpendicular to a slip direction. Details were obtained of the crystallographic orientation of dislocation layers, their lateral extension and their mean separation. Also it was possible to identify lattice rotations localised at these

layers. Bulk specimens can be examined in reflection geometry by removing layers of material to expose fresh surfaces, and these layers may then be used to prepare foils for TEM which would give information on the dislocation arrangements within the macroscopic structure.

6.3 The effect of rotation about the scattering vector

The variation in the γ-measured FWHM on rotation about the scattering vector, when expressed as a polar plot with the FWHM as radial ordinate and the angle of incidence with respect to a fixed direction in the scattering plane (**figure 2.1**) as angular ordinate, traces a peanut-shell shape. Work published by Schneider and Lehmann[36] using a small cube of copper, (2 x 2 x 2mm$^3$), gave measurements at 15° intervals for 360° of rotation about the scattering vector, using three reflections. Their curve for rotation about the $2\bar{2}0$ vector is reproduced in figure 6.2a. The FWHM's measured for the small plate crystals as a function of (section 3.3) using the $0\bar{2}2$ reflection, correspond in shape to this curve for the angular ranges measured.

The angular dependence of the FWHM on the direction of incidence may be explained in terms of the volume of deformed crystal traversed by the incoming radiation for a given angle of incidence. The characteristic peanut-shell shape is a linear sum of the effect of deformation on each slip system, projected onto the scattering planes. The peanut is generated theoretically by considering, for a perfect unieformed f.c.c. crystal, the number of slip planes of one system crossed by the incident beam as a function of angle of incidence, rotating about the scattering vector, (i.e. this number of planes

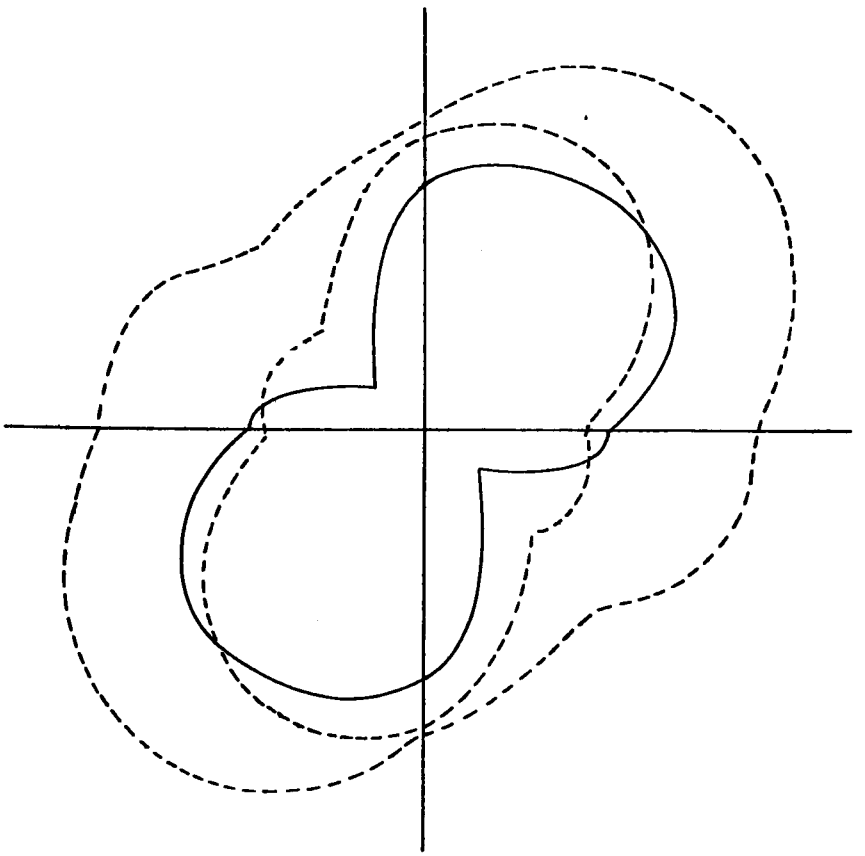

Figure 6.2a. Theoretical approximations (broken curves) to Schneider and Lehmann's measured values of FWHM (solid curve) rotating about the $\bar{2}20$ scattering vector in a small copper single crystal.

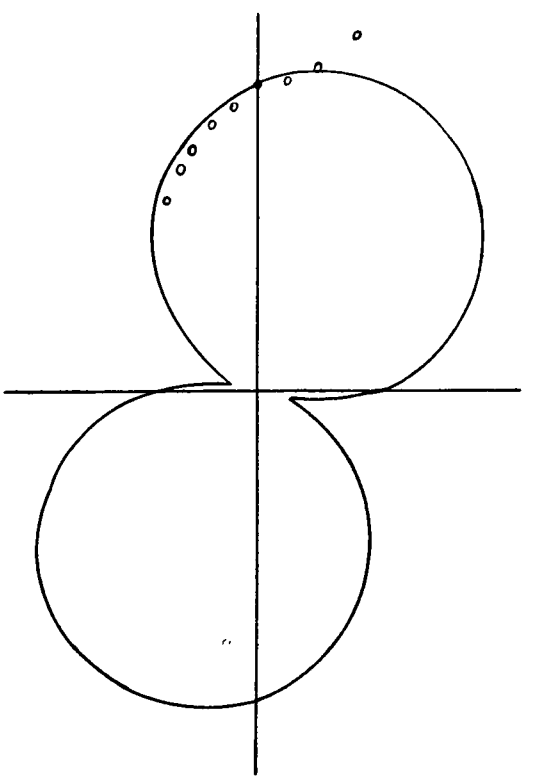

Figure 6.2b. The open circles represent FWHM's measured in crystal B42, and the full curve was calculated from equation (6.4) using measured slip band spacings for B42.

represents the radial ordinate of a polar plot). The (111) and ($\bar{1}$11) planes give rise to similar shapes which are at different orientations with respect to a reference direction in the (0$\bar{2}$2) scattering plane, (fig.6.3a). The (1$\bar{1}$1) and ($\bar{1}\bar{1}$1) planes give smaller peanuts, also identical to each other in size and shape but at different orientations with respect to the reference direction, (fig.6.3b). Figures 6.3a and b were calculated using lattice plane spacings projected onto the scattering plane to show the peanut shell shapes corresponding to each set of slip planes in an f.c.c. crystal. In deformed single crystals the number of bands of deformation per unit path length traversed by the incident beam accounts for the peanut-shell shape and the dislocation density within the bands contributes to the angular misorientation. The number of deformation bands per unit path length, m, is

$$m = \frac{|\underline{q} \times \underline{g}|}{d|\underline{q}||\underline{g}|} \cos\left(\arcsin\left(\frac{\underline{q} \times \underline{g} \cdot \underline{p}}{|\underline{q} \times \underline{g}|\,|\underline{p}|}\right) - \phi\right) \qquad 6.1$$

where $\underline{q}$ is the slip plane normal, $\underline{g}$ the scattering vector, $\underline{p}$ is a reference direction in the scattering plane, d the deformation band spacing in the direction of $\underline{q}$, and $\phi$ is the variation in the angle of incidence with respect to the scattering direction. The derivation of equation (6.1) is given in figure 6.4. Because the Bragg angles for the stronger Y-ray reflections are less than 20mrad the incident beam direction was taken to lie in the scattering plane.

It was possible, using expression (6.1), to fit theoretical curves the shapes of the polar plots determined experimentally for the small plates of section 3.3. An example of this fit is given in figure 6.2b for crystal B42. The empirical factor obtained from this had units of

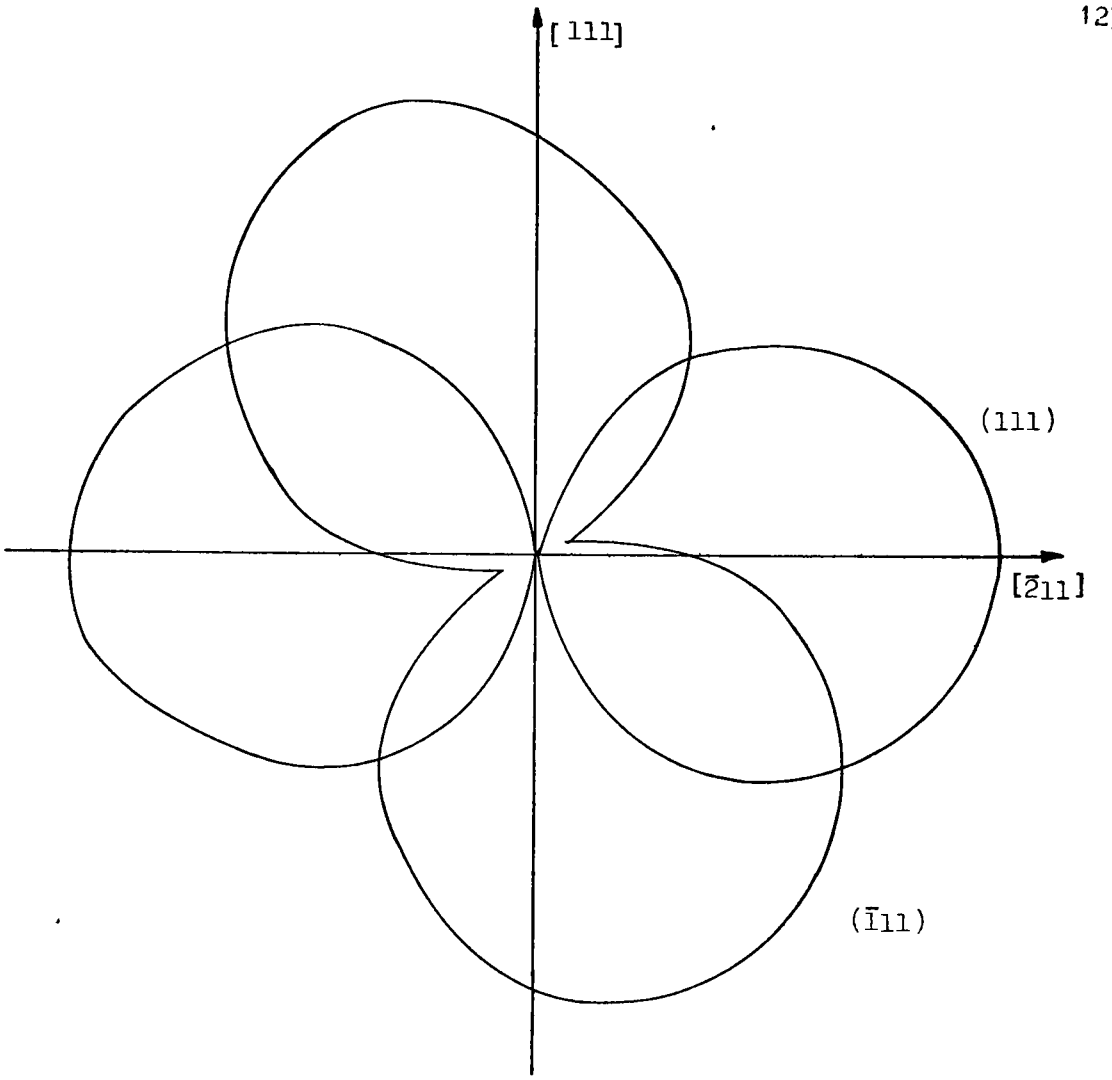


Figure 6.3a

Peanut-shell shapes for (111) and ($\bar{1}$11) slip systems on rotating about the 0$\bar{2}$2 vector.

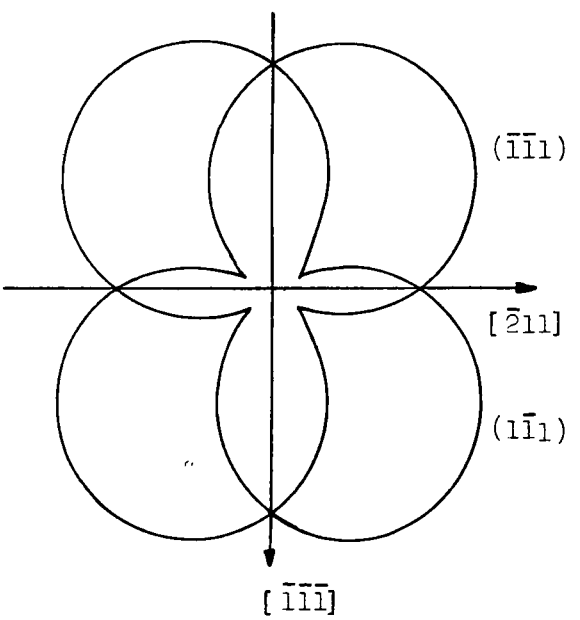


Figure 6.3b

Peanut-shell shapes for the (1$\bar{1}$1) and ($\bar{1}\bar{1}$1) slip sustems on rotating about the 0$\bar{2}$2 scattering vector.

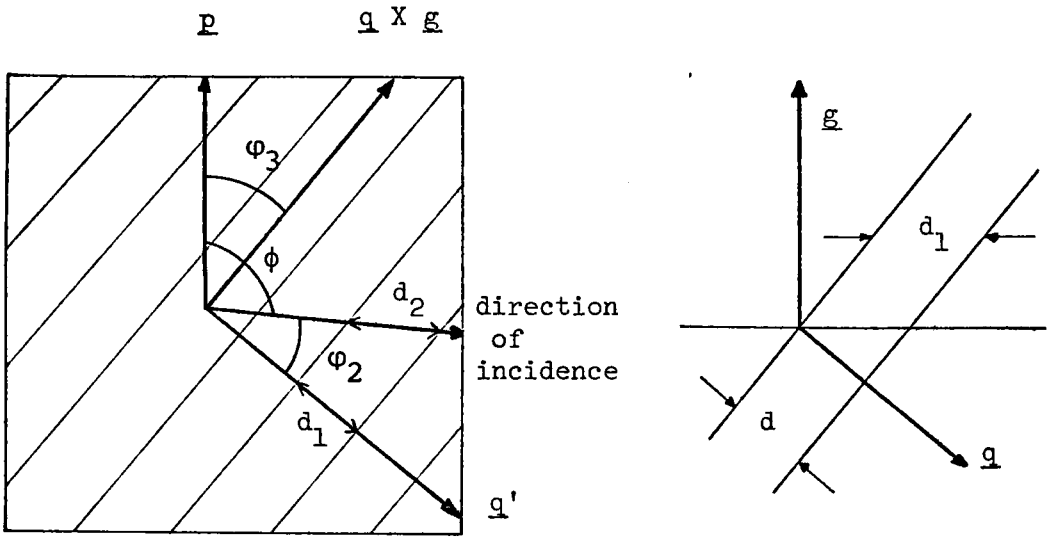


Figure 6.4a plan view of scattering plane. Figure 6.4b elevation.

The scattering vector $\underline{g}$ points out of the page, $\underline{p}$ is a reference direction, $\underline{q}'$ is the projection of $\underline{q}$ in the scattering plane; d is the slip plane spacing and $d_1$ is this spacing projected onto the scattering plane.

From figure 6.4b

$$d_1 = \frac{d}{\sin\varphi} = \frac{d\,q\,g}{\underline{q} \times \underline{g}}$$

From figure 6.4a

$$d_2 = \frac{d_1}{\cos\varphi_2} = \frac{d_1}{\cos(\ 90 + \varphi_3 - \phi)}$$

$$\text{where } \varphi_3 = \arccos \frac{\underline{q} \times \underline{g} \cdot \underline{p}}{q\,g\,p}$$

thus

$$d_2 = \frac{d_1}{\sin \arccos \dfrac{\underline{q} \times \underline{g} \cdot \underline{p}}{q\,g\,p} - \phi}$$

whence

$$m = \frac{1}{d_2}$$

Figure 6.4 The derivation of the expression for m, the number of slip planes traversed per unit path length of the incident beam.

length and could be reduced to a dimensionless quantity by considering such parameters as the dislocation density, the width of deformation bands in the crystal, and the cross-section of the incident radiation. Linear combinations of the values which were derived from the electron microscopy experiments gave factors which were several orders of magnitude different from the empirical fit parameters, and it must be concluded that the rocking curve half-width has a more complex dependence on defect structure.

Approximations to the shape of Schneider and Lehmann's polar plots were generated using equation (6.1) i.e. assuming equal amounts of slip in four {111} systems. These are shown for rotation about the $2\bar{2}0$ vector, for four and three active slip systems, with the measured curve in figure 6.2a. The units and scale of the theoretical curves are arbitrary and not equivalent to the measured values. Differing amounts of slip on the different slip systems alter the ratio of maximum to minimum radial ordinate, but does not significantly alter the orientation of the plot, i.e. by more than a few degrees. In the absence of more details of the deformation a better fit could not be attempted.

A possible explanation for the peanut-shell mosaic distribution offered by Schneider and Lehmann was that the minimum in the plot corresponded to an 'intrinsic mosaic spread' which is that of a perfect crystal. The larger values of W/W' were then that value plus a

contribution due to the curvature of lattice planes, which they measured as 4.1mrad over 2mm in one crystal. In terms of the model presented here, the minima correspond to an incident beam passing through the least amount of deformation, which in the case of a lightly deformed crystal may give a measured FWHM near that of a perfect crystal. Any dislocation arrangement with regular spacings on slip planes should satisfy equation (6.1).

Although this model requires a much more thorough investigation, the present results would seem to indicate that a geometrical factor needs to be considered in the mosaic spread determination. The type of defect arrangement assumed for the model is consistent with the pillbox dislocation structure observed by Steeds[54] in deformed copper single crystals, if slip occurs on four different {111} planes. For such cases in f.c.c. crystals the theoretical mosaic block would take the physical form of an irregular octahedron. The preferred orientation of such blocks would imply that extinction will also have a geometrical dependence. The effect of this would be particularly severe for neutron diffraction where the Bragg angles are large and several orders of the same reflection are being considered.

This geometrical effect has, to some extent, been included in a computer program to correct absorption and extinction in diffraction measurements[80]. Results similar to those discussed in this section were noted during an investigation[81] of the variation of diffracted intensity with azimuthal angle using a graphite crystal. This study of the homogeneity of the monochromatic beam made no reference to the defect structure of the crystal.

## 6.4 Application of x-ray theories to γ-ray measurements

The main difficulty in adapting x-ray theories for the diffraction profiles of crystals containing dislocations to γ-ray and neutron profiles stems from the high absorption of x-rays shown by most materials. This restricts x-ray experiments to Bragg reflection geometry for samples of significant dimensions, or to thin lamallae in Laue geometry. The penetration into the crystal surface by an x-ray beam is of the order of a few microns. Thus the probability of finding a uniform dislocation distribution over the volume irradiated by x-rays is much greater than in the γ-ray and neutron cases. Theoretical half-widths and integrated intensities for perfect and mosaic crystals indicate that the FWHM's should be more sensitive to an increase of defects than the integrated intensities. The theories relating half-widths and dislocation densities rely on Gaussian, Lorentzian or Cauchy distributions approximating random arrangements of dislocations. Various authors claim that these have been readily obtained by irradiating crystals in the stress-applied condition, since on unloading the dislocations relax forming dipoles and clusters, and the resulting degree of order reduces the applicability of the theory. Low dislocation densities are necessary to avoid the dislocation interactions forming network or layer structures. However for such low densities, and predominantly edge dislocations, Kaufmann[65] found that the half-width should depend mainly on distribution rather than the density of dislocations. This was assuming the half-width to be composed of two components, due to the lattice tilts and the lattice strains. The theoretical treatment indicated that the tilt broadening was independent of Bragg angle, whereas the strain

contribution was a function of $\tan\Theta_B$. The experiments of Bachmann et al[66] with small rectangular copper single crystal blocks deformed along [$\bar{1}$01] in compression, were analysed on the basis of this model. These experiments were similar to γ-ray measurements on block crystals, some of which are described in section 3.2. Apart from the differences in absorption coefficients for x-rays and γ-rays, the other major difference was in the range of dislocation densities in the deformed crystals used in each set of experiments. Bachmann's annealed crystals had a dislocation density when deformed of the order of that in the undeformed blocks used for the γ-ray measurements. Empirical relationships from the x-ray results indicated a dependence of the measured half-widths for the 111 reflections on the cube of the applied stress. This dependence was observed with the 220 reflections in larger copper single crystals of similar orientation and shape in γ-ray rocking curves. However γ-ray measurements in the larger crystals with 111 reflections indicated an approximately linear relationship. The multiple peaks reported by Bachmann were recorded in areas which were affected by crystal-anvil frictional effects and could well be analogous to the multiple peaks recorded in similarly deformed regions using γ-rays. Bachmann made no attempt to analyse such curves, which were recorded in crystals for which the dislocations had not been pinned in the stress-applied state. Transmission electron microscopy and Bormann x-ray topography identified the presence of primary and secondary dislocation Burgers vectors in the regions of more homogeneous deformation structure used for the x-ray experiments. The scatter in the measured x-ray rocking curve half-widths about a mean value

was attributed to the accumulation of dislocations of the same sign.

The Krivoglaz and Ryaboshapka theory[62] was based on a cylindrical crystal containing a large number of straight, parallel dislocations randomly distributed over the cross-section. This results in a diffraction profile which is represented by a Gaussian function with a half-width proportional to the square root of the dislocation density, and which depends logarithmically on the radius of the model crystal. The physical identity of this latter parameter was clarified by Wilkens and Bargouth[64] in terms of a characteristic spacing of the dislocation distribution, following which they developed a theory encompassing several sets of dislocations in a 'restrictedly random' distribution with an outer cut-off radius as an adjustable parameter which is determined, with the dislocation density, from measured diffraction profiles. The theory is applicable to dislocation densities of greater than $10^{8} mm^{-2}$.

Although it was derived assuming a model of a cylindrical crystal composed of equal sized sub-areas containing equal numbers of dislocations parallel to the cylinder axis, the Wilkens theory can be extended to dislocations in real crystals. The dislocation character enters the Fourier function only in the form of a constant, and this constant may be varied to include screw and edge components and an interaction term. Analysis of this theory[76] leads to an expression for the experimentally determined profile which is dependent only on the diffraction angle, $\omega$, the dislocation density and factors describing the dislocations, and the scattering vector.

$$I(S) = \frac{g^2 b^2 \bar{z} \bar{\rho}}{8 \pi S^3} + \ldots \qquad 6.2$$

where

$$S = \frac{2}{\lambda}(\sin \omega - \sin \Theta_3) \qquad 6.3$$

and $\bar{C}$ is an average value of the constant referred to above for all sets of dislocations present. The average dislocation density is $\bar{\rho}$, g is the scattering vector and b is the Burgers vector averaged over the types of dislocation. The expression (6.2) is independent of outer cut-off radius, which is derived from the elastic energy of a dislocated crystal and assumed to be approximately the radius of a sub-area. A graph of $I(S)\ S^3$ versus S tends to an asymptotic value at large S, from which $\bar{\rho}$ may be determined. The product of outer cut-off radius and the square root of the dislocation density, M, needs to be of the order of unity for this approach to be valid. M affects the shape of the function (6.2) at small S (fig. 6.5a) but not at larger values. The theory has been applied with reasonable success to x-ray profiles recorded in crystals containing up to $10^5$ dislocations per square millimetre, where the dislocations were not arranged in grain boundaries or concentrations of dipoles or multipoles.

Application of this theory to the γ-ray diffraction profiles led to predicted dislocation densities much higher than those measured by electron microscopy in equivalent volumes (c.f. $2.4 \times 10^{11} mm^{-2}$ from theory and $3 \times 10^{7} mm^{-2}$ measured). Neither dislocation losses during foil preparation nor the uncertainty in experimentally determined densities would account for this discrepancy. The theory does not cater for the possibility of dislocations being arranged in braids, networks or sub-structures of coarse slip bands, and such distributions as were present in the crystals examined by γ-rays invalidate the 'restrictedly random' model. The values of b and the line directions of the dislocations included in the parameter C were obtained from electron micrographs in the γ-ray case, but for the x-ray measurements

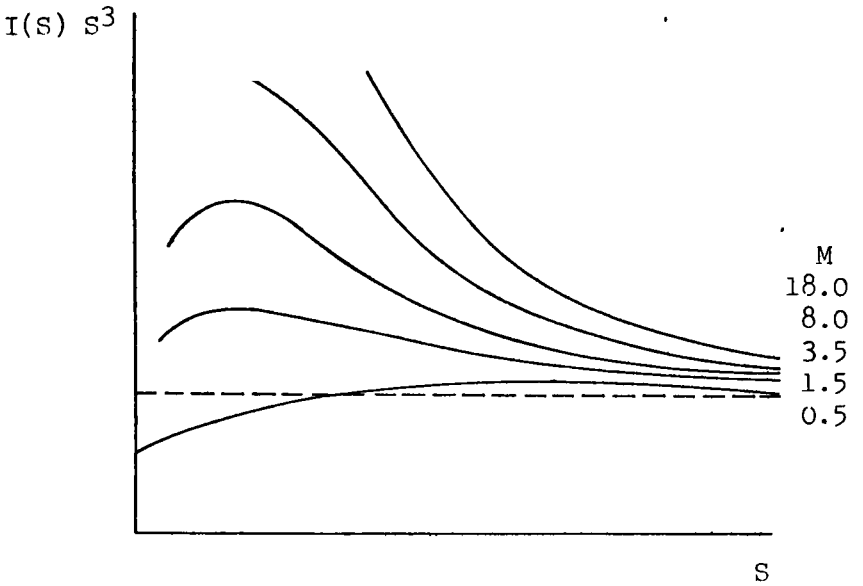


Figure 6.5a

The shape of $I(S)\ S^3$ versus S for increasing values of M. The broken line corresponds to the asymptotic slope for infinitely large S.

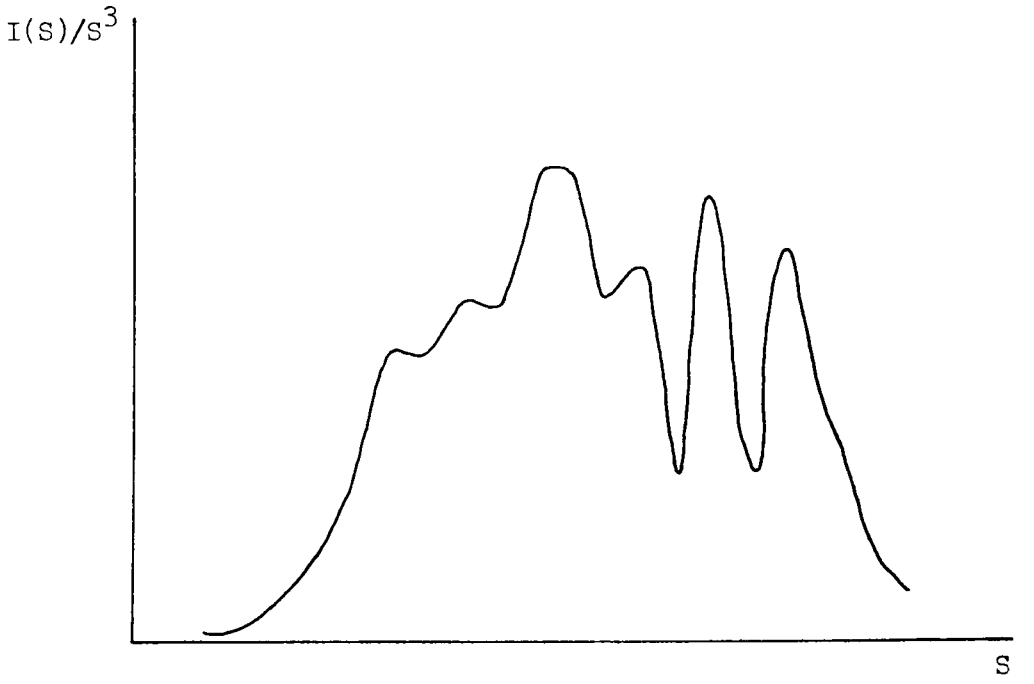


Figure 6.5b

The shape of the same function from $\gamma$-ray measurements of an irregularly shaped rocking curve.

were an average of all possible dislocations. Thus any errors in determining these values from the electron micrographs could lead to a bias in the theoretical prediction, but this would be to a lower dislocation density. The function $I(S)\ S^3$ varies smoothly with increasing S (fig. 6.5a), but the experimental version corresponding to irregular multiple peaks was jagged and frequently failed to converge to an asymptotic value within the measured range of S (fig. 6.5b). A comparison of these two figures indicates that for such γ-ray results M was not approximately unity, i.e. there was a considerable degree of interaction between dislocations. An alternative function for determining M and hence ρ was proposed by Tournarie[77] and Wilson et al[78] as being suitable for large values of M, but these were found by Wilkens to be very sensitive to experimental errors, and were not tested with γ-ray measurements.

It was not possible to test adequately the Warren and Averbach theory[67] which determines particle size and strain broadening effects because sufficient measurements for several orders of reflection in both undeformed and deformed crystals were not made. Since none of the γ-ray peaks could be said to be symmetrical, both halves had to be analysed separately, taking the centre of gravity of each peak as the origin for the Fourier analysis. No useful conclusions were drawn.

Although the principles of x-ray diffraction apply to the diffraction of γ-rays, the dislocation structure in compressed copper crystals, of the form used for this thesis, is far from the models necessary to the theories. The general result of all the attempted analyses, based on theories which are more or less satisfactory for x-rays, was that the defect structure did not follow a random or near random arrangement of dislocations. This fact was borne out by the

electron microscopy studies on the same crystals.

## Conclusions

This work represented a broadly-based study of copper as a monochromator material and of the various diffraction theories which may be applied to such crystals. The theoretical approach to neutron diffraction has been based on the equations for x-ray diffraction for the case of zero absorption. These equations have been investigated as a function of wavelength and thickness with both neutrons and Y-rays and qualitative agreement between theoretical and experimental parameters was obtained. The theoretical approach is dependent on an idealised defect structure in the crystals being investigated, and this type of structure, having a Gaussian distribution of lattice misorientations, is rarely found in deformed copper single crystals.

The crystals deformed as large flat plates, the ideal monochromator geometry, had an extremely varied microstructure, which was due to their being compressed along the shortest axis. To improve the microstructure copper single crystals were compressed along the length of large rectangular blocks (24 x 24 x 54mm). Although the defect structure was inhomogeneous at the ends of the blocks, sections with a more uniform structure were removed from the centres and used for diffraction measurements.

The Y-ray diffraction was extremely sensitive to variations in defect structure with position in the crystal, and this sensitivity was found to be dependent not only on dislocation density, but on the large-scale arrangement of dislocation structures. The dislocation densities and small-scale arrangements showed a qualitative agreement with the form of the Y-ray rocking curves. It was found that the width of a rocking curve varied with the crystallographic direction of

incidence, and a theoretical consideration of this has led to the suggestion that the diffraction of γ-rays is sensitive to regions of relatively perfect crystal, tens of microns in diameter, between bands of heavily deformed crystal. The shape of the experimentally determined function describing the variation of rocking curve width with azimuthal angle could be reproduced theoretically from this model.

X-ray theories were applied to the γ-diffraction data in order to determine defect densities and arrangements. It was found that these theories also require a uniform microstructure, which is more easily achieved for x-rays, since they only penetrate a few microns into the crystal, than for γ-rays which penetrate centimetres.

Neutron measurements on a flat plate cut to step configuration were used to determine the wavelength dependence of various diffraction parameters, but the inhomogeneity of the defect structure prevented a coherent analysis. However the microstructure did not appear to affect the neutron absorption, and the wavelength dependence of this was established. It was also shown that a relationship between neutron and γ-ray rocking curves is only feasible for very uniform defect structures. The diffraction of γ-rays is ideal for revealing irregularities in the defect structure which would impair the homogeneity of a monochromated neutron beam without being immediately obvious in the neutron diffraction profile.

References


1 Antonini M., Corchia M., Nicotera E., Rustichelli F.
Nucl.Inst.& Meth. 104, 147, 1972

2 Thomas P. J.App.Cryst. 5, 78, 1972

3 Kalus J., Gobert G., Schedler E.,
J.Phys.E 6, 488, 1973

4 Maier-Leibnitz H., Ann.Acad.Sci.Fenn.Phys.Ser. A6, 267, 1967

5 Rustichelli F. Nucl.Inst.& Meth. 74, 219, 1969
" Nucl.Inst.& Meth. 83, 124, 1970

6 Freund A., Guinet P., Marechal J., Rustichelli F., Vanoni F.
J.Cryst.Growth 13/14, 726, 1972

7 Boeuf A., Rustichelli F.,
Nucl.Inst.& Meth. 107. 429, 1973

8 Hohlwein D J.App.Cryst. 8,465, 1975

9 Rasmussen S.E., Schneider J.R.,
I.L.L. report 74F42S

10 Aldiner F., Freund A., Proc.of Be.Conf., Roy.Met.Soc.

11 Boeuf A., et.al. Nucl.Inst.& Meth. 152, 415, 1978

12 Zachariasen W.H. Theory of x-ray diffraction. Wiley. New York
" Act Cryst. 23, 558, 1967
" Acta Cryst. A24, 421, 1968

13 DeMarmes R.E., Hall W., Lehmann G.W.,
Bull.Amer.Phys.Soc. 11, 129, 1966

14 Goldberger M.L., Seitz F.,
Phys.Rev.71, 294, 1947

15 Darwin C.G. Phil.Mag. 27, 315 & 657, 1914
" Phil.Mag.43, 800, 1922

16 Dorner B. J.App.Cryst. 4, 185, 1971

17 Bacon G.E., Lowde R.D.,
Acta Cryst. 1, 303, 1948

18 Malik S. J.App.Cryst. 9, 273, 1976

19 Tagaki S. Acta Cryst. 15, 1311, 1962
" J.Phys.Soc.Japan 26, 1239, 1969

20 Taupin D. Bull.Soc.Franc.Miner.Cryst.LXXXVII, 469, 1964

21 Dietrich O.W., Als-Nielsen J.,
Acta Cryst. 18, 184, 1965

22 Kato N. Acta Cryst. 4, 526 & 627, 1961

23 Schlangenoto H. Z.Phys. 203, 17, 1967

24 Howie A., Whelan M. Proc.Eur.Reg.Conf.Elect.Mic.,Delft 1,194,1960

" Proc.Roy.Soc. A263, 217, 1961

" Proc.Roy.Soc. A267, 206, 1962

25 Hirsch P.B., Howie A., Whelan M.J.,
Trans.Roy.Soc. A252, 499, 1960

26 Wilkens M. Phys.Stat.Sol. 5, 175, 1964

" Phys.Stat.Sol. 6, 939, 1964

" Phys.Stat.Sol.13, 529, 1966

27 Penning P., Polder D., Phillips Res.Rep. 16, 419, 1961

28 Kato N. J.Phys.Soc.Jap. 18, 1785, 1963

" Acta Cryst. A32, 455 & 458, 1976

" Acta Cryst. A35, 9, 1979

29 Kambe K. Z.Naturforsch 20a, 770, 1965

30 Kuriyama M. Acta Cryst.A31, 774, 1975

Kuriyama M, Miyakawa T.,
Acta Cryst. A26, 667, 1970

31 Becker P.J., Coppens P.,
Acta Cryst. A30, 192 & 148, 1974

" " Acta Cryst. A31, 417, 1975

Coppens P., Hamilton W.C.,
Acta Cryst. A26, 71, 1970

32 Freund A. Nucl.Inst.& Meth. 124, 93, 1975

" I.L.L. report 74T42S

" ORNL report CONF 760601-P2 Oak Ridge .

33 Freund A. Ph.D.thesis, Technischen Universität München

34 Werner S.A. J.App.Phys. 45, 3246, 1974

35 Schneider J.R., J.App.Cryst. 7, 547, 1974

36 Schneider J.R., Lehmann M.S.,
Acta Cryst. A33, 789, 1977

37 Tuberfield K.C. A.E.R.E. report R5647 Harwell 1968

38 Modrzejewski A., Kobla J.,
Kristall und technik 4, 135, 1969

39 Dymond R.R., Brockhouse B.N.,
Instrumentation for neutron scattering research I.A.E.A. Vienna 1970

40 Barrett C.S., Meuller M.H., Heaton L.,
Rev.Sci.Inst. 34, 847, 1963

41 Dolling G., Niemann H., Nucl.Inst.& Meth. 49, 117, 1967
42 Schull C.G. M.I.T. report AFSOR TR 60-111 1960
43 Schneider J.R., Stump N., Nucl.Inst.& Meth. 125, 605, 1975
44 Sturm W.J. Phys.Rev. 71, 757, 1947
45 LeHazif R., Dorizzi P., Poirier J.P. Acta Met. 21, 903, 1973
46 Jazienski Z., Piatkowski A., Litwora A., Mem.Sci.Rev.Met.mai, 323, 1976
47 Vorbrugg W., Goetting H.Ch., Schwink C, Phys.Stat.Sol. (b) 46, 257, 1971
48 Takeuchi T., Trans.Jap.Inst.Met. 16, 629, 1975
" Trans.Jap.Inst.Met. 18, 97, 1976
" J.Phys.Soc.Jap. 40, 741, 1976
" J.Phys.Soc.Jap. 41, 490, 1976
49 Basinski Z.S., Basinski S., Phil.Mag. 9, 51, 1964
Essmann U. Acta Met. 21, 1305, 1973
" Phys.Stat.Sol. 17, 723, 1966
Essmann, Rapp H., Wilkens M., Acta Met. 12, 1468, 1964
" Acta Met. 16, 1275, 1968
Fourie J.T. Phil.Mag. 17, 735, 1968
Fourie J.T., Murphy M.J., Phil.Mag. 7, 1617, 1962
Hazzledine P.M. Can.J.Phys. 45, 765, 1967
Katajima S., Tanaka H., Kaieda H., Trans.Jap.Inst.Mets. 10, 12, 1969
Livingston J.D. Acta Met. 10, 229, 1962
" J.App.Phys. 31, 1071, 1960
Price W.J., Washburn J., J.Aust.Inst.Mets. 8, 1, 1963
Staker M.R., Holt D.L., Acta Met. 20, 569, 1972
Swann P.R. Acta Met. 11, 511, 1963
VanDrunen G., Saimoto S., Acta Met. 19, 213, 1971
50 Kocks U.F., Nakada Y., Ramaswami B., Trans.A.I.M.E. 230, 1005, 1964

51 Essmann U. Phys.Stat.Sol. 12, 707,& 723, 1965

52 Göttler E. Phil.Mag.28, 1057, 1973

" Phys.Stat.Sol. 9, 485, 1965

Göttler E., Ambrosi P., Schwink C.,
Scripta Met. 8, 1093, 1974

53 Mughrabi H. Phil.Mag. 18, 1211, 1967

" Phil.Mag. 23, 869, 1971

" Phys.Stat.Sol. 39, 317, 1970

54 Steeds J.W. Proc.Roy.Soc. A292, 343, 1966

" Proc.Int.Conf.Sci.Tech.Iron & Steel 1971

55 Kawasaki Y. J.Phys.Soc.Jap. 36, 142, 1974

56 Mecking H., Bulian G., Acta Met. 24, 249, 1976

57 Buck O., Essmann U., Phys.Stat.Sol. 4, 143, 1964

58 Bassim N.M., Kuhlmann-Wilsdorf D.,
Cryst.Latt.Def. 4, 9, 1973

" Phys.Stat.Sol. A15, 725, 1973

" Phys.Stat.Sol. A16, 241, 1974

" Phys.Stat.Sol. A17, 379, 197

" Phys.Stat.Sol. A19, 335, 197

59 Scoble W., Weissmann S., Cryst.Latt.Def. 4, 123, 1973

60 Wilkens M. Private communication

61 Krivoglaz M.A. Fiz.Metal.Metalloved. 12, 465, 1961

" Theory of x-ray & thermal neutron scattering
by real crystals. Plenum. New York

62 Krivoglaz M.A., Ryaboshapka K.P.
Phys.Met.Metall. 15, 14, 1963

63 Mittels M., Sherrill F., Young F.,
Phys.Letters 5, 183, 1963

64 Wilkens M., J.App.Cryst. 8, 191, 1975

" Phys.Stat.Sol. (a) 2, 359, 1970

Wilkens M., Bargouth M.O.,
Acta Met. 16, 465, 1968

65 Kaufman L., Kulin S.A., Trans.A.I.M.E. 215, 273, 1959

66 Bachmann K.J., Baldwin T., Young F.W.,
J.App.Phys. 41, 4733, 1970

67 Warren B.E., Averbach B.L.,
J.App.Phys. 21, 595, 1950
J.App.Phys. 23, 497, 1952

68 Backofen W.A., Deformation processing, Addison Wesley 1972

69 Hazzledine P.M. Inst.of Phys.Conf.Elec.Micr. Cambridge 1963

70 Ham R.K. Phil.Mag. 6, 1183, 1961

71 Freund A. HMI Bericht B273, Berlin 1978

72 Bogdanov S.G., Menshikov A.Z.,
Acta Cryst. A32, 869, 1976

73 Schneider J.R. J.App.Cryst. 8, 195, 1975

74 Brugger R.M. Nucl.Inst.& Meth. 135, 289, 1976

75 International tables for x-ray crystallography
Kynoch Press, Birmingham 1976

76 Wilkens M., Phys.Stat.Sol. 3, 1718, 1963

77 Tournarie C.R. Acad.Sci.(France) 242, 2016, & 2161, 1956

78 Wilson A.J.C. Proc.Phys.Soc. 78, 249, 1961

79 Wilkens M. Can.J.Phys. 45, 567, 67
Auer H., Obst B., Wilkens M.,
Mat.Sci.Eng. 3, 33 & 41, 69
Mughrabi H. Proc.4th conf. Strength of metals and alloys
3, 1404, 1976

80 Flack H.D. Acta Cryst. A30, 589, 1974
" " J.App.Cryst. 8, 520, 1975
" " Acta Cryst. A33, 890, 1977

81 Harkema S., Dam.J., van Hummel G.J., Reuvers A.J.,
Acta Cryst. A36, 433, 1980

# APPENDIX I

Tables giving examples of experimental and theoretical parameters relevant to the chapters on γ-ray and neutron diffraction.

| T mm | | $r_p$ % | β mrad | $R_\Theta$ $10^{-3}$ | E s |
|---|---|---|---|---|---|
| 2.5 | E | 2.8 | 0.7 | 0.023 | 51 |
| | F | 3.0 | 0.5 | 0.023 | 51 |
| | G | 2.6 | 0.7 | 0.022 | 54 |
| | H | 2.8 | 0.7 | 0.022 | 53 |
| 5.4 | T | 3.6 | 1.1 | 0.043 | 53 |
| | S | 2.6 | 1.8 | 0.044 | 52 |
| | R | 2.8 | 1.5 | 0.044 | 52 |
| 8.5 | C | 4.3 | 1.4 | 0.082 | 40 |
| | D | 4.9 | 1.2 | 0.075 | 45 |
| | I | 6.2 | 1.0 | 0.069 | 50 |
| | J | 5.2 | 1.2 | 0.071 | 48 |
| | O | 4.3 | 1.1 | 0.067 | 51 |
| | P | 4.4 | 2.0 | 0.068 | 51 |
| 11.4 | A | 3.5 | 3.1 | 0.106 | 42 |
| | B | 3.9 | 3.3 | 0.113 | 48 |
| | K | 5.0 | 1.3 | 0.095 | 48 |
| | L | 4.3 | 1.8 | 0.094 | 49 |
| | M | 3.1 | 3.3 | 0.094 | 49 |
| | N | 3.1 | 3.5 | 0.096 | 47 |

Table 3.3.

Data recorded from γ-ray measurements with crystal PP3I using the $0\bar{2}2$ reflection. The letters correspond to the positions indicated in figure 3.8

| T mm | | $r_p$ % | β mrad | $R_\Theta$ $10^{-3}$ | $E_s$ % |
|---|---|---|---|---|---|
| 2.5 | N | 6.7 | 0.8 | 0.060 | 59 |
| 5.4 | A | 8.6 | 1.9 | 0.147 | 45 |
| | B | 10.0 | 1.3 | 0.144 | 46 |
| | C | 6.1 | 2.6 | 0.160 | 40 |
| | D | 5.6 | 2.2 | 0.134 | 50 |
| 8.5 | J | 10.2 | 2.1 | 0.186 | 56 |
| | K | 9.0 | 2.5 | 0.183 | 57 |
| | L | 9.8, 6.9 | 1.2, 1.3 | 0.193 | 54 |
| | M | 8.2, 7.5 | 1.9, 1.4 | 0.211 | 50 |
| 11.4 | E | 16.1 | 1.8 | 0.292 | 48 |
| | F | 15.3 | 2.1 | 0.311 | 44 |
| | G | 12.5 | 2.8 | 0.324 | 42 |
| | H | 12.5 | 2.1 | 0.323 | 42 |
| | I | 11.2 | 3.0 | 0.308 | 45 |

Table 3.4a

Rocking curve data from γ-ray measurements in crystal PP3I using the $1\bar{1}1$ reflection in positions A to N (fig. 3.8c)

| T mm | | $r_p$ % | β mrad | $R_\Theta$ $10^{-3}$ | $E_s$ % |
|---|---|---|---|---|---|
| 2.4 | M | 4.1 | 1.7 | 0.074 | 20 |
| | L | 2.6 | 2.3 | 0.064 | 31 |
| | K | 3.5 | 1.2 | 0.061 | 34 |
| | J | 3.7 | 1.2 | 0.059 | 36 |
| 5.4 | P | 3.9 | 2.0 | 0.133 | 33 |
| | O | 5.2 | 2.4 | 0.135 | 32 |
| | N | 4.2 | 2.9 | 0.129 | 35 |
| 8.5 | F | 9.5 | 2.9 | 0.205 | 34 |
| | G | 7.0, 6.3 | 2.0, 1.1 | 0.193 | 36 |
| | H | 7.1, 6.2 | 1.5, 1.1 | 0.182 | 41 |
| | I | 6.3, 5.9 | 1.7, 1.2 | 0.187 | 39 |
| 11.4 | E | 10.0 | 2.3 | 0.230 | 46 |
| | D | 10.6 | 2.5 | 0.272 | 36 |
| | C | 12.8 | 1.9 | 0.263 | 38 |
| | B | 12.1 | 1.9 | 0.252 | 40 |
| | A | 9.8 | 2.7 | 0.273 | 35 |

Table 3.4b

γ-ray data for crystal PP3I recorded using the 200 reflection in the positions shown in figure 3.8

| T mm | | $r_p$ % | β mrad | $R_\Theta$ $10^{-3}$ | $E_s$ % |
|---|---|---|---|---|---|
| 3.0 | M | 3.8 | 0.56 | 0.030 | 36 |
| | N | 1.7 | 0.90 | 0.019 | 59 |
| 5.9 | E | 8.3 | 1.0 | 0.093 | 51 |
| | F | 6.2 | 1.1 | 0.089 | 53 |
| | G | 9.4 | 1.0 | 0.076 | 60 |
| | H | 8.5 | 1.0 | 0.092 | 52 |
| | S | 10.7 | 1.2 | 0.131 | 32 |
| | T | 7.1 | 0.9 | 0.084 | 56 |
| 8.9 | A | 9.3 | 0.53 | 0.062 | 35 |
| | B | 7.3 | 0.82 | 0.064 | 33 |
| | K | 5.6 | 1.1 | 0.064 | 34 |
| | L | 7.1 | 0.83 | 0.061 | 36 |
| | O | 6.5 | 0.79 | 0.053 | 40 |
| | P | 9.1 | 0.43 | 0.060 | 37 |
| 11.7 | C | 5.5 | 1.5 | 0.083 | 42 |
| | D | 6.6 | 1.3 | 0.085 | 41 |
| | I | 7.1 | 1.1 | 0.080 | 44 |
| | J | 6.5 | 1.1 | 0.079 | 45 |
| | Q | 5.0 | 1.5 | 0.081 | 44 |
| | R | 7.5 | 1.4 | 0.113 | 13 |

Table 3.5a

γ- ray rocking curve results for crystal PP3II using the $0\bar{2}2$ reflection in the positions of figure 3.8

| T mm | | $r_p$ % | β mrad | $R_\Theta$ $10^{-3}$ | $E_s$ % |
|---|---|---|---|---|---|
| 3.0 | J | 10.0 | 1.0 | 0.110 | 24 |
| | K | 8.6 | 1.2 | 0.111 | 23 |
| | L | 3.9 | 2.8 | 0.106 | 27 |
| 8.9 | I | 16.5 | 1.3 | 0.237 | 44 |
| | H | 12.0 | 2.1 | 0.253 | 40 |
| | G | 14.2 | 1.8 | 0.241 | 43 |
| | F | 13.2 | 1.7 | 0.229 | 46 |
| 11.7 | A | 3.5 | 5.1 | 0.165 | 71 |
| | B | 4.4 | 3.4 | 0.153 | 72 |
| | C | 6.0 | 2.0 | 0.145 | 74 |
| | D | 5.0 | 2.7 | 0.146 | 74 |
| | E | 4.9 | 3.1 | 0.151 | 73 |

Table 3.5b

Data recorded in crystal PP3II with γ-ray rocking curves and the $11\bar{1}$ reflection in the positions shown in figure 3.8

| T mm | | $r_p$ % | β mrad | $R_\Theta$ $10^{-3}$ | $E_s$ % |
|---|---|---|---|---|---|
| 3.0 | A | 3.5 | 2.2 | 0.074 | 32 |
| | B | 4.0 | 1.4 | 0.078 | 28 |
| | C | 2.6 | 2.9 | 0.073 | 33 |
| 5.9 | M | 3.4 | 4.1 | 0.120 | 45 |
| | N | 4.7, 3.6 | 0.8, 1.7 | 0.108 | 50 |
| | O | 3.0, 2.7 | 1.1, 3.0 | 0.121 | 45 |
| | P | 2.7 | 3.0 | 0.107 | 51 |
| 8.9 | D | 10.4 | 1.4,1.7 | 0.207 | 36 |
| | E | 10.7, 7.6 | 1.0,1.3 | 0.199 | 39 |
| | F | 10.8, 6.8 | 1.2,1.0 | 0.205 | 37 |
| | G | 9.9, 6.5 | 1.6,1.2 | 0.206 | 37 |
| | H | 9.2 | 3.1 | 0.194 | 40 |
| 11.6 | I | 10.7 | 1.5 | 0.237 | 45 |
| | J | 11.4 | 1.8 | 0.239 | 45 |
| | K | 8.9 | 2.4 | 0.232 | 47 |
| | L | 7.6, 5.4 | 2.0,2.2 | 0.241 | 45 |

Table 3.6a

Rocking curve data from γ-ray measurements using the 200 reflection in crystal PP3II. The letters correspond to the positions indicated in figure 3.

| T mm | | $r_p$ % | β mrad | $R_\Theta$ $10^{-3}$ | $E_s$ % |
|---|---|---|---|---|---|
| 3.0 | A | 5.1 | 1.8 | 0.093 | 11 |
| | B | 5.2 | 1.5 | 0.093 | 11 |
| | C | 4.1 | 1.6 | 0.093 | 15 |
| 5.9 | M | 5.5, 4.6 | 2.5,2.0 | 0.189 | 13 |
| | N | 7.9, 6.1 | 1.0,1.3 | 0.192 | 12 |
| | O | 3.7 | 6.4 | 0.183 | 16 |
| | P | 4.3 | 2.5 | 0.172 | 19 |
| 8.9 | D | 13.2, 9.4 | 1.2,1.45 | 0.279 | 14 |
| | E | 15.9, 12.1 | 0.8,1.2 | 0.271 | 17 |
| | F | 14.5, 10.4 | 0.1,0.7 | 0.279 | 14 |
| | G | 15.2, 9.6 | 1.0,1.1 | 0.292 | 10 |
| | H | 11.3 | 2.5 | 0.293 | 10 |
| 11.7 | I | 16.9 | 1.9 | 0.365 | 16 |
| | J | 17.2 | 1.8 | 0.364 | 17 |
| | K | 12.3 | 2.8 | 0.370 | 15 |
| | L | 11.7 | 4.1 | 0.372 | 15 |

Table 3.6b

These data were recorded for crystal PP3II under the same conditions as for table 3.6a, following an arbitrary rotation about the scattering vector 200.

| Crystal | B1 | B2 | B3 | B4 |
|---|---|---|---|---|
| Stress MPa | 4.26 | 47.7 | 8.2 | 18.2 |
| Strain % | 0.48 | 2.76 | 2.79 | 1.5 |
| Strain rate $10^{-4}$ $sec^{-1}$ | 6 | 3 | 6 | 1.5 |
| Deformation temperature K | ~100 | 290 | ~100 | 290 |

Table 3.7

Details of the compression of the rectangular block crystals.

| Crystal | $R_\Theta$ $10^{-3}$ | $r_p$ % | β mrad | $R_\Theta$ $10^{-3}$ | $r_p$ % | β mrad |
|---|---|---|---|---|---|---|
| B1 | 0.012 | 5.39 | 0.183 | 0.172 | 28.79 | 0.406 |
| B2 | 0.012 | 5.70 | 0.163 | 0.349 | 4.93 | 7.280 |
| B3 | - | - | - | 0.315 | 3.24 | 2.401 |
| B4 | 0.022 | 5.33 | 0.436 | 0.270 | 9.74 | 2.180 |

Table 3.8a, before (left) and after (right) deformation

| Crystal | $R_\Theta$ $10^{-3}$ | $r_p$ % | β mrad | $R_\Theta$ $10^{-3}$ | $r_p$ % | β mrad |
|---|---|---|---|---|---|---|
| B1 | 0.151 | 24.22 | 0.475 | 0.346 | 35.29 | 0.631 |
| B2 | 0.161 | 30.38 | 0.405 | 0.881 | 10.18 | 8.79 |
| B3 | 0.203 | 31.54 | 0.518 | 0.999 | 11.14 | 7.67 |
| B4 | 0.247 | 30.83 | 0.725 | 0.814 | 20.84 | 2.75 |

Table 3.8b, before (left) and after (right) deformation

| Crystal | $R_\Theta$ $10^{-3}$ | $r_p$ % | β mrad | $R_\Theta$ $10^{-3}$ | $r_p$ % | β mrad |
|---|---|---|---|---|---|---|
| B1 | 0.154 | 30.36 | 0.456 | 0.356 | 40.50 | 0.644 |
| B2 | 0.211 | 36.78 | 0.410 | 0.902 | 9.81 | 7.19 |
| B3 | 0.104 | 36.22 | 0.341 | 1.140 | 9.49 | 7.65 |
| B4 | 0.235 | 25.48 | 0.796 | 0.745 | 18.96 | 3.16 |

Table 3.8c, before (left) and after (right) deformation

Tables 3.8

Data from Y-ray measurements on the block crystals before and after compression, using the 220 (table 3.8a) and 111 (3.8b) reflections. Table 3.8c contains results for the 111 reflection following a $90^o$ rotation about the scattering vector.

| $\phi^\circ$ | $\beta$ mrad | $r_p$ % | $R_\Theta$ $10^{-5}$ | $E_s$ % | |
|---|---|---|---|---|---|
| +15 | 2.24 | 0.91 | 2.431 | 8.8 | |
| +10 | 2.25 | 0.88 | 2.226 | 15.9 | |
| + 5 | 2.33 | 0.88 | 2.186 | 17.4 | |
| 0 | 2.38 | 0.83 | 2.161 | 18.3 | |
| - 5 | 2.33 | 0.84 | 2.189 | 17.3 | |
| -10 | 2.23 | 0.95 | 2.281 | 13.8 | |
| -15 | 1.97 | 1.00 | 2.239 | 15.36 | |
| -20 | 1.86 | 1.16 | 2.527 | 4.4 | Table 3.10a |

| $\phi^\circ$ | $\beta$ mrad | $r_p$ % | $R_\Theta$ $10^{-5}$ | $E_s$ % | |
|---|---|---|---|---|---|
| +15 | 7.56 | 0.27 | 2.182 | 17.7 | |
| +10 | 6.73 | 0.24 | 1.489 | 43.8 | |
| + 5 | 6.40 | 0.27 | 2.020 | 23.8 | |
| 0 | 6.33 | 0.14 | 1.173 | 55.5 | |
| - 5 | 5.82 | 0.40 | 2.512 | 5.2 | |
| -10 | 5.59 | 0.41 | 2.121 | 19.9 | |
| -15 | 5.11 | 0.41 | 2.474 | 6.6 | |
| -20 | 4.80 | 0.41 | 2.357 | 1.1 | |
| -25 | 4.36 | 0.41 | 2.064 | 22.1 | Table 3.10b |

| $\phi^\circ$ | $\beta$ mrad | $r_p$ % | $R_\Theta$ $10^{-5}$ | $E_s$ % | |
|---|---|---|---|---|---|
| +25 | .551 | 3.22 | 1.853 | 29.4 | |
| +20 | .471 | 3.71 | 1.745 | 33.4 | |
| +15 | .409 | 3.93 | 1.583 | 39.4 | |
| +10 | .416 | 3.76 | 1.595 | 39.0 | |
| + 5 | .366 | 4.25 | 1.601 | 38.6 | |
| 0 | .343 | 3.94 | 1.501 | 42.4 | |
| - 5 | .298 | 4.19 | 1.550 | 40.4 | |
| -10 | .271 | 4.49 | 1.665 | 35.8 | |
| -15 | .295 | 4.45 | 1.671 | 35.7 | |
| -20 | .245 | 4.20 | 1.533 | 40.8 | |
| -25 | .256 | 4.04 | 1.666 | 36.7 | Table 3.10c |

Tables 3.10

Y-diffraction data from rocking curves measured at $5^\circ$ intervals in the range $\pm 25^\circ$ to the direction [ 111 ] , rotating about the vector $0\bar{2}2$ (section 3.3).

| $\lambda$ Å | $r_p$ % | $\beta$ mrad | $R_\theta$ $10^{-3}$ | $R_k$ $10^{-3}$ | $\eta$ mrad | $E_s$ % | $r_{pth}$ % |
|---|---|---|---|---|---|---|---|
| 0.683 | 11.78 | 3.49 | 0.116 | 0.414 | 1.48 | 72 | 8.79 |
| 1.08 | 26.75 | 4.80 | 1.093 | 1.099 | 2.04 | 0 | 15.97 |
| 1.69 | 42.22 | 4.36 | 2.291 | 3.253 | 1.85 | 29 | 36.54 |
| 1.971 | 35.63 | 4.80 | 1.146 | 5.215 | 2.038 | 78 | 35.63 |

Table 5.1a

| $\lambda$ Å | $r_p$ % | $\beta$ mrad | $R_\theta$ $10^{-3}$ | $R_k$ $10^{-3}$ | $\eta$ mrad | $E_s$ % | $r_{pth}$ % |
|---|---|---|---|---|---|---|---|
| 0.683 | 19.26 | 3.49 | 0.549 | 0.896 | 1.48 | 39 | 13.90 |
| 1.08 | 37.73 | 5.67 | 1.060 | 2.382 | 2.41 | 55 | 21.55 |
| 1.69 | 47.95 | 5.67 | 2.924 | 7.049 | 2.41 | 58 | 34.81 |
| 1.971 | 43.81 | 6.11 | 6.540 | 11.299 | 2.60 | 42 | 33.96 |

Table 5.1b

| $\lambda$ Å | $r_p$ % | $\beta$ mrad | $R_\theta$ $10^{-3}$ | $R_k$ $10^{-3}$ | $\eta$ mrad | $E_s$ % | $r_{pth}$ % |
|---|---|---|---|---|---|---|---|
| 0.683 | 26.08 | 4.36 | 0.712 | 1.432 | 1.85 | 50 | 13.56 |
| 1.08 | 43.47 | 5.23 | 2.086 | 3.805 | 2.22 | 45 | 25.00 |
| 1.69 | 50.0 | 6.98 | 3.363 | 11.258 | 2.96 | 70 | 29.63 |
| 1.971 | 44.77 | 7.42 | 3.917 | 18.045 | 3.15 | 73 | 27.12 |

Table 5.1c

| $\lambda$ Å | $r_p$ % | $\beta$ mrad | $R_\theta$ $10^{-3}$ | $R_k$ $10^{-3}$ | $\eta$ mrad | $E_s$ % | $r_{pth}$ % |
|---|---|---|---|---|---|---|---|
| 0.683 | 22.80 | 6.11 | 0.843 | 1.844 | 2.60 | 54 | 10.86 |
| 1.08 | 45.53 | 6.98 | 3.268 | 4.901 | 2.96 | 33 | 21.81 |
| 1.69 | - | - | - | - | - | - | - |
| 1.971 | 49.94 | 10.03 | 6.230 | 23.239 | 4.26 | 73 | 22.74 |

Table 5.1d

Table 5.1

Neutron measured parameters and values derived from these results for the $0\bar{2}2$ reflection in crystal PP4. Table 5.1a is for the thickness 2.5mm, 5.1b for 5.5mm, 5.1c for 8.7mm and table 5.1d is for the 11.2mm thickness. The theoretical peak reflectivities, $r_{pth}$, are those corresponding to figure 5.2b.

| $\lambda$ Å | $r_p$ % | $\beta$ mrad | $R_\theta$ $10^{-3}$ | $R_k$ $10^{-3}$ | $\eta$ mrad | $E_s$ % | $r_{pth}$ % |
|---|---|---|---|---|---|---|---|
| 0.71 | 19.3 | 4.58 | 0.962 | 1.046 | 1.94 | 8 | 15.28 |
| 1.049 | 32.7 | 4.76 | 1.727 | 2.330 | 2.02 | 26 | 27.04 |
| 1.458 | 44.49 | 5.41 | 2.654 | 4.642 | 2.30 | 43 | 36.74 |
| 1.859 | 43.33 | 6.72 | 3.081 | 7.887 | 2.85 | 61 | 40.49 |
| 2.239 | 45.95 | 7.11 | 3.607 | 12.036 | 3.02 | 70 | 42.14 |

Table 5.2a

| $\lambda$ Å | $r_p$ % | $\beta$ mrad | $R_\theta$ $10^{-3}$ | $R_k$ $10^{-3}$ | $\eta$ mrad | $E_s$ % | $r_{pth}$ % |
|---|---|---|---|---|---|---|---|
| 0.71 | 31.45 | 5.85 | 1.924 | 2.268 | 2.48 | 15 | 19.10 |
| 1.049 | 40.13 | 7.33 | 3.056 | 5.049 | 3.11 | 39 | 28.03 |
| 1.458 | 45.70 | 8.99 | 4.195 | 10.058 | 3.82 | 58 | 35.16 |
| 1.859 | 47.45 | 9.21 | 4.789 | 17.089 | 3.91 | 72 | 37.62 |
| 2.239 | 51.13 | 9.55 | 5.136 | 26.078 | 4.06 | 80 | 36.23 |

Table 5.2b

| $\lambda$ Å | $r_p$ % | $\beta$ mrad | $R_\theta$ $10^{-3}$ | $R_k$ $10^{-3}$ | $\eta$ mrad | $E_s$ % | $r_{pth}$ % |
|---|---|---|---|---|---|---|---|
| 0.71 | 38.36 | 6.59 | 2.527 | 3.622 | 2.80 | 30 | 19.68 |
| 1.049 | 44.91 | 7.85 | 4.104 | 8.064 | 3.33 | 49 | 27.87 |
| 1.458 | 48.06 | 9.51 | 4.721 | 16.063 | 4.04 | 71 | 32.92 |
| 1.859 | 48.30 | 11.61 | 5.264 | 27.293 | 4.93 | 81 | 32.56 |
| 2.239 | 50.64 | 11.17 | 5.764 | 41.648 | 4.74 | 86 | 30.00 |

Table 5.2c

| $\lambda$ Å | $r_p$ % | $\beta$ mrad | $R_\theta$ $10^{-3}$ | $R_k$ $10^{-3}$ | $\eta$ mrad | $E_s$ % | $r_{pth}$ % |
|---|---|---|---|---|---|---|---|
| 0.71 | 43.67 | 5.98 | 2.972 | 4.665 | 2.54 | 36 | 20.31 |
| 1.049 | 50.16 | 7.02 | 3.831 | 10.385 | 2.98 | 63 | 26.84 |
| 1.458 | 49.38 | 10.12 | 4.880 | 20.687 | 4.30 | 76 | 30.01 |
| 1.859 | 49.62 | 11.61 | 6.004 | 35.149 | 4.93 | 83 | 29.00 |
| 2.239 | 51.45 | 13.26 | 5.207 | 53.637 | 5.63 | 90 | 25.90 |

Table 5.2d

Neutron measured parameters, and values derived from these results, for the 111 reflection in crystal PP4. Table 5.2a is for the thickness 2.5mm, 5.2b for 5.5mm, 5.2c for 8.7mm and 5.2d for 11.2mm. $r_{pth}$ are theoretical peak reflectivities.

## APPENDIX II

A bibliography containing the referenced from the body of the thesis (here numbered on the right), and some additional material not specifically referenced elsewhere. These references are divided according to subject matter and listed in alphabetical order of author.


Standard text books

Arndt U.W., Willis B.T.M. Single crystal diffractometry Cambridge University Press 1966.

Bacon G.E. Neutron diffraction 3rd Ed. Oxford

James R.W. The optical principles of the diffraction of x-rays Cornell University Press 1965.

Hirsch P.B., Howie A., Nicholson R.B., Pashley D.W., Whelan M.J. Electron microscopy of thin crystals Butterworths 1971.

Marshall W., Lovesey S.W., Theory of thermal neutron scattering Oxford University Press 1971

Zachariasen W.H. The theory of x-ray diffraction in crystals Dover Press 1967.

Diffraction theory

| | | |
|---|---|---|
| Atans'ev A.M., Kohn V.G. | Acta Cryst.A27, 421, 1971 | |
| Becker P.J., Coppens P., | Acta Cryst.A30, 129 & 148, 1974 | 31 |
| " " | Acta Cryst.A31, 417, 1975 | 31 |
| Coppens P., Hamilton W.C., | Acta Cryst.A26, 71, 1970 | 31 |
| Darwin C.G. | Phil.Mag.27, 315 & 657, 1914 | 15 |
| " | Phil.Mag.43, 800, 1922 | 15 |
| Goldberger M.L., Seitz F., | Phys.Rev.71, 294, 1947 | 14 |
| Hamilton W.C. | Acta Cryst.10, 629, 1957 | |
| Howie A., Whelan M.J., | Proc.Eur.Reg.Conf.Elect.Mic. Delft 1, 194, 1960 | 24 |
| " " | Proc.Roy.Soc.A263, 217, 1961 | 24 |
| " " | Proc.Roy.Soc.A267, 206, 1962 | 24 |

Hirsch P.B., Howie A., Whelan M.J.,
Trans.Roy.Soc. A252, 499, 1960 25
Kambe K. Z.Naturforsch 20a, 770, 1965 29
Katagawa T., Kato N., Acta Cryst. A30, 830, 1974
Kato N. J.Phys.Soc.Japan 10, 46, 1955
" Acta Cryst. 13, 349, 1960
" Acta Cryst. 4, 526 & 627, 1961 22
" J.Phys.Soc.Japan 18, 1785, 1963 28
" Acta Cryst. A32, 455, & 458, 1976 28
" Acta Cryst. A35, 9, 1979 28
Krivoglaz M.A., Ryaboshapka K.P.,
Phys.Met.Metall. 15, 14, 1963 62
Krivoglaz M.A. Fiz.Met.Metall. 12, 465, 1961 61
Kuriyama M. J.Phys.Soc.Japan 23, 1369, 1967
" Acta Cryst. A28, 588, 1972
Kuriyama M., Early J.G., Acta Cryst. A30, 525, 1974
Kuriyama M. Acta Cryst. A31, 774, 1975 30
Kuriyama M., Miyakawa T., Acta Cryst. A26, 667, 1970 30
Ladell J., Spielberg N., Acta Cryst. A21, 103, 1966
Schlangenoto H. Z.Phys. 203, 17, 1967 23
Tagaki S. Acta Cryst. 15, 1311, 1962 19
" J.Phys.Soc.Japan 26, 1239, 1969 19
Taupin D. Bull.Soc.Franc.Miner.Cryst.LXXXVII,
469, 1964 20
Wilkens M. Phys.Stat.Sol. 5, 175, 1964 26
" Phys.Stat.Sol. 6, 939, 1964 26
" Phys.Stat.Sol. 13, 529, 1966 26
Zachariasen W.H. Acta Cryst. A23, 558, 1967 12
" Acta Cryst. A25, 102, 1969 12

Neutron diffraction

Antonini M., Corchia M., Nicotera E., Rustichelli F.,
Nuc.Inst.& Meth. 104, 147, 1972 1
Bacon G.E., Lowde R.D., Acta Cryst. 1A, 303, 1948 17
Barrett C.S., Meuller M.H., Heaton L.,
Rev.Sci.Inst. 34, 847, 1963 40

Bogdanov S.G., Menshikov A.Z., Acta Cryst. A32, 869, 1976 72

Brugger R.M. Nuc.Inst.& Meth. 135, 289, 1976 74

Boeuf A., Rustichelli F., Nucl.Inst.& Meth. 107, 429, 1973 7

Cooper M.J., Rouse K.D., Acta Cryst. A26, 214, 1970

" " Acta Cryst. A32, 806, 1976

DeWarmes R.W., Hall W., Lehman G.W., Bull Amer.Phys.Soc. 11, 129, 1966 13

Dietrich O.W., Als Nielsen J., Acta Cryst. 18, 184, 1965 21

Dolling G., Niemann H., Nucl.Inst.& Meth. 49, 117, 1967 41

Dorner B. J.App.Cryst. 4, 185, 1971 16

Dymond R.R. MSc.thesis, McMaster University, Ontario

Dymond R.R., Brockhouse B.N., Inst.Neut.Scatt.Res.I.A.E.A. Vienna 1970 39

Freund A. Nucl.Inst.& Meth. 124, 93, 1975 32

Freund A. J.Cryst.Growth 13/14, 247, & 726 1972 6

" Nucl.Inst.& Meth. 124, 93, 1975 32

" J.App.Cryst. 8, 194, 1975

" I.L.L. report 74F42S 32

" ORNL report CONF 7606601-P2 Oak Ridge 32

" HMI Bericht B273 Berlin 1978 71

" PhD.thesis Technischen Universität München 33

Frey F. Nucl.Inst.& Meth. 115, 277, 1974

" Nucl.Inst.& Meth. 125, 9, 1975

Hohlwein D. J.App.Cryst. 8, 465, 1975 8

Kalus J., Gobert G., Schedler E., J.Phys.E 6, 488, 1973 3

Maier-Leibnitz H. Ann.Acad.Sci.Fenn.Phys.Ser. A6, 267, 1967 4

Malik S.S. J.App.Cryst. 9, 273, 1976 18

Moon R.M., Schull C.G., Acta Cryst. 17, 805, & 812, 1964

Riste T., Otnes K., Nucl.Inst.& Meth. 75, 197, 1969

" Nucl.Inst. & Meth. 86, 1, 1970

| | | |
|---|---|---|
| Rustichelli F. | Nucl.Inst.& Meth. 74, 219, 1969 | 5 |
| " | Nucl.Inst.& Meth. 83, 124, 1970 | 5 |
| Popa N.C. | Acta Cryst. A32 | |
| Sailor V.L., Foote H.L., Landon H.H., Wood R.E., | Rev.Sci.Inst. 27, 26, 1956 | |
| Schneider J.R., Stump N., | Nucl.Inst.& Meth. 125, 605, 1975 | 43 |
| Schull C.G. | M.I.T. report AFSOR TR 60-111, 1960 | 42 |
| Sears V.F. | Acta Cryst. A33, 373, 1977 | |
| Sturm W.J. | Phys.Rev. 71, 757, 1947 | 44 |
| Thomas P. | J.App.Cryst. 5, 78, 1972 | 2 |
| Tuberfield K.C. | A.E.R.E. report 25647 Harwell 1968 | 37 |
| Weber K. | Acta Cryst. 16, 535, 1963 | |
| Werner S.A., Arratt A., | Phys.Rev. 140, 675, 1965 | |
| Werner S.A., Arratt A., King J.S., Kendrick H., | J.App.Phys. 37, 2343, 1966 | |
| Werner S.A. | Acta Cryst. A25, 639, 1969 | |
| " | Acta Cryst. A27, 665, 1971 | |
| " | J.App.Phys. 45, 3246, 1974 | 34 |


γ-ray and x-ray diffraction


| | | |
|---|---|---|
| Bachmann K.J., Baldwin T.O., Young F.W., | J.App.Phys. 41, 4783, 1970 | 66 |
| Baldwin T.O. | J.App.Phys. 39, 1541, 1968 | |
| Brogren G. | Acta Cryst. A25, 111, 1969 | |
| Colella R., Merlini A., | Phys.Stat.Sol. 14, 81, 1966 | |
| Kaufmann L., Kulin S.A., | Trans.A.I.M.E. 215, 273, 1959 | 65 |
| Penning P., Polder D., | Acta Cryst. 17, 950, 1964 | 27 |
| Schneider J.R. | J.App.Cryst. 7, 541, 1974 | |
| " | J.App.Cryst. 7, 547, 1974 | 35 |
| " | J.App.Cryst. 8, 195, 1975 | 73 |
| " | J.App.Cryst. 8, 350, 1975 | |
| " | J.App.Cryst. 9, 394, 1976 | |
| Schneider J.R., Lehmann M., | Acta Cryst. A33, 789, 1977 | 36 |
| Schwartz L.H. | Acta Cryst. 17, 1614, 1964 | |
| Tounarie J.R. | Acad.Sci.(France) 242, 2016 & 2161, 1956 | 77 |
| Warren B.E., Averbach B.L., | J.App.Phys.21, 595, 1950 | 67 |
| " " | J.App.Phys.23, 497, 1952 | 67 |

| | | |
|---|---|---|
| Wilkens M. | Phys.Stat.Sol. 2, 692, 1962 | |
| " | Phys.Stat.Sol. 3, 1718, 1963 | 76 |
| " | Acta Cryst. 17, 963, 1964 | |
| " | Can.J.Phys. 45, 567, 1967 | |
| " | Acta Met. 15, 1412, 1967 | |
| " | Phys.Stat.Sol. (a)2, 359, 1970 | 64 |
| " | J.App.Cryst. 8, 191, 1975 | 64 |
| Wilkens M., Bargouth M.O., | Acta Met. 16, 465, 1968 | 64 |
| Wilson A.J.C. | Proc.Phys.Soc. 78, 249, 1961 | 78 |
| Wittels M.C., Sherrill F.A., | Young F.W., Phys.Letters 5, 183, 1963 | 63 |
| Young F.W., Baldwin T.O., | Phys.Rev. 163, 3, 1967 | |
| Young F.W. | J.App.Phys. 36, 2225, 1965 | |

Crystal deformation structures

| | | |
|---|---|---|
| Aldinger F., Freund A., | Proc.Be.Conf.,Roy.Met.Soc. 1978 | 10 |
| Basinski Z.S., Basinski S., | Phil.Mag. 9, 51, 1964 | 49 |
| Bassim N.M., Kuhlmann-Wilsdorf D., | Cryst.Latt.Def.4, 9, 1973 | |
| " | Phys.Stat.Sol. A15, 725, 1973 | |
| " | Phys.Stat.Sol. A16, 241, 1974 | |
| " | Phys.Stat.Sol. A17, 379, 197 | |
| " | Phys.Stat.Sol. A19, 335, 197 | |
| Boeuf A., et.al. | Nucl.Inst.& Meth. 152, 415, 1978 | 58 |
| Buck O., Essmann U., | Acta Met. 12, 1181, 1964 | 11 |
| " " | Phys.Stat.Sol. 4, 143, 1964 | 57 |
| Crump J.D., Young F.W., | Phil.Mag. 17, 381, 1968 | |
| Essmann U. | Acta Met. 12, 1463, 1964 | 49 |
| " | Phys.Stat.Sol. 12, 707, & 723, 1965 | 51 |
| " | Phys.Stat.Sol. 17, 723, 1966 | 49 |
| " | Acta Met. 21, 1305, 1973 | 49 |
| Essmann U., Rapp M., Wilkens M., | Acta Met. 16, 1275, 1968 | 49 |
| Fourie J.T., Murphy M.J., | Phil.Mag. 7, 1617, 1962 | 49 |
| Fourie J.T. | Can.J.Phys. 45, 777, 1967 | |
| " | Phil.Mag. 17, 735, 1968 | 49 |
| Göttler E., Krause D., | Phys.Stat.Sol. 9, 435, 1965 | 52 |
| Göttler E. | Phil.Mag. 28, 1057, 1973 | 52 |

Göttler E., Ambrosi P., Schwink C.,
Scripta Met. 8, 1093, 1974 52

Ham R.K. Phil.Mag. 6, 1183, 1961 70

Hazzledine P.M. Can.J.Phys. 45, 765, 1967 49

" Inst.of Phys.Conf.Elec.Mic.Cambridge 1963 69

Jazienski Z., Piatkowski A., Litwora A.,
Mem.Sci.Rev.Met.mai, 323, 1976 46

Katajima S., Tanaka H., Kaieda H.,
Trans.Jap.Inst.Met. 10, 12,1969 49

Kawasaki Y. J.Phys.Soc.Japan 36, 142, 1974 55

Kochs U.F., Nakada Y., Ramaswami B.,
Trans.A.I.M.E. 230, 1005, 1964 50

LeHazif R., Dorizzi P., Poirier J.P.
Acta.Met.21, 903, 1973 45

Livingston J.D. Acta Met. 10, 229, 1962 49

" J.App.Phys. 31, 1071, 1960

Mecking H., Bulian G., Acta Met. 24, 249, 1976 56

Mughrabi H. Phil.Mag. 18, 1211, 1967 53

" Phil.Mag. 23, 869, 1971 53

" Phys.Stat.Sol. 39, 317, 1970 53

Muira S., Kuriyama Y., Saeki Y.,
Trans.Jap.Inst.Mets. 18, 852, 1977

Rasmussen S.E., Schneider J.R.,
I.L.L. report 74F42S 9

Roberts W., Bergstrom Y., Acta Met. 21, 457, 1973

Price A.J., Washburn J., J.Aust.Inst.Mets. 8, 1, 1963 49

Scoble W., Weissmann S., Cryst.Latt.Defects 4, 123, 1973 59

Staker M.R., Holt D.L., Acta Met. 20, 569, 1972 49

Swann P.R., Warlimont H., Acta Met. 11, 511, 1963 49

Steeds J.W. Proc.Roy.Soc. A292, 343, 1966 54

Takeuchi T. Jap.J.App.Phys. 8, 320, 1969

" J.Phys.Soc.Jap. 32, 677, 1972

" Trans.Jap.Inst.Met. 16, 629, 1975 48

" Trans.Jap.Inst.Met. 18, 97, 1976 48

" J.Phys.Soc.Jap. 40, 741, 1976 48

" J.Phys.Soc.Jap. 41, 490, 1976 48

VanDrunen G., Saimoto S., Acta Met. 19, 213, 1971 49

VorBrugg W., Goetting H.C., Schwink H.C., Phys.Stat.Sol. 46(b), 257, 1971 47

Material parameters

Arlinghaus F.J. Phys.Rev. 153, 743, 1969

Linkoaho M.V. Phil.Mag. 23, 191, 1971

Straumanis M.E., Yu L.S., Acta Cryst. A25, 676, 1969

Varshni Y.P. Phys.Rev. B2, 3952, 1971

Schneider C.S. Acta Cryst. A32, 375, 1976

Wakoh S., Yamashita J., J.Phys.Soc.Japan 30, 422, 1971

Specimen preparation

Livingston J. J.App.Phys. 31, 1071, 1960

Lovell L.C., Wernick J.H., J.App.Phys. 30, 590, 1959

Mitchell J.W., Chevrier J.C., Hockey B.J., Monaghan J.P., Can.J.Phys. 45, 453, 1967

Nauhausen H., Schulz G., Phys.Stat.Sol. 43, 493, 1978

Ruff A.W. J.App.Phys. 33, 3392, 1962

Stepian R.M., Prohaska J.P., Metallography 9, 51, 1976

Young F.W. J.App.Phys. 32, 192, 1961

" J.App.Phys. 33, 963, 1962

## APPENDIX III

### Symbols used in the text

$\Theta, \Theta_B$ the angle between the incident direction and the reflecting planes, i.e. the Bragg angle.

$\lambda$ the wavelength in Angstroms.

$\Delta\lambda$ the wavelength spread.

$\phi$ the azimuthal angle measured in the plane perpendicular to the scattering vector.

$P_o$ the power of the incident beam.

$P_T$ the power in the transmitted beam measured far from the Bragg reflecting position.

$P_H$, the power of the diffracted beam recorded as a function of crystal.

$P_H(T)$ rotation through the Bragg reflection, (at depth T in the crystal).

$\omega$ the crystal rotation measured from an arbitrary origin.

$r_p$ the maximum ordinate of the diffraction profile, usually as a percentage of the incident intensity.

$\beta$,FWHM the width of the diffraction profile at half maximum intensity, usually in units of mrads.

$R_\Theta$ the integrated intensity or integrated reflectivity, i.e. the area under the diffraction profile.

$R_k$ the kinematical integrated reflectivity, $R_k = QT_o$.

$R_m$ the measured integrated intensity.

$\kappa$ a measure of absorption related to the anomolous dispersion of electrons in outer valence shells.

$A$ a term characterising the diffraction behaviour of a crystal, $A = r_o F T_o K / (V)$.

$r_o$ the classical electron radius, $r_o = e^2/mc^2$.

$F$ the structure factor.

$T_o, T$ the crystal thickness.

| | |
|---|---|
| $K$ | a polarisation factor, $K = (1 + \cos^2 2\theta)/2$. |
| $\gamma$ | $= \cos\theta$, or gamma radiation depending on context. |
| $V$ | the volume of a crystallographic unit cell. |
| $t_o$ | the mean mosaic block thickness. |
| $\mu_e$ | the effective absorption coefficient. |
| $\mu_o, \mu$ | the linear absorption coefficient |
| $\zeta\sigma$ | the fractional power loss per unit path length, the secondary extinction coefficient. |
| $\sigma$ | the scattering power. |
| $W(\Delta)$ | the mosaic distribution, a Gaussian error function. |
| $\Delta$ | the deviation from the exact Bragg angle. |
| $\eta$ | the theoretical mosaic spread parameter, equivalent to the standard deviation of a Gaussian error function. |
| $y$ | $= T_o \Delta\pi \sin 2\theta/(\lambda\gamma)$. |
| $Q$ | $= r_o^2 K\lambda^3 F^2/(V^2 \sin 2\theta)$ for x-rays and $\gamma$-rays, $Q = \lambda^3 F^2/(V^2 \sin 2\theta)$ for neutrons. |
| $j$ | $= (\eta\ 2\pi)^{-1}$. |
| $f(\lambda)$ | a correction factor for primary extinction. |
| $\underline{g}$ | the scattering vector. |
| $I$ | intensity of radiation. |
| $I_o, I_b$ | incident and background intensities respectively. |
| $E_s$ | the measured extinction coefficient, as a percentage, $E_z = R_k - R_m/R_k$. |
| $b_s$ | the neutron scattering length in units of $10^{-10}$mm. |
| $\underline{B}$ | the electron beam direction. |
| $\underline{N}$ | the downward normal to the specimen. |
| $\underline{D}$ | the displacement of a unit cell from its lattice position in a perfect crystal. |
| $\Phi_o, \Phi_g$ | the amplitudes of the direct and diffracted electron beams respectively. |

$\xi_o, \xi_g$ extinction lengths for electron diffraction.

$s_g$ the deviation from the exact Bragg angle for electron diffraction.

b the Burgers vector.

$\Lambda$ applied stress in MPa.

f the thickness of an electron microscope specimen.

$L_p$ the length of a line feature projected onto the electron microscope screen.

$\nu$ the number of intercepts of dislocations with randomly drawn circles on electron micrographs.

$L_c$ the total length of the random circles (above).

$\rho$ the dislocation density.

$\delta\theta$ the orientation change across a band of dislocations.

$L_K$ Kikuchi line shift.

x the distance of a diffraction spot from the centre of the diffraction pattern.

$d_o$ the lattice spacing of a given set of reflecting planes.

$\mu_T$ the total neutron attenuation.

$\mu_C$ the neutron capture cross-section.

$\mu_{FA}$ the neutron free-atom cross-section per unit volume.

$\exp(-2G)$ the Debye-Waller factor reducing the coherent scattering amplitude.

Y a material constant relevant to neutron absorption.

$B_D$ the Debye parameter.

$\tau$ the absolute temperature.

$\mu_M$ the measured total neutron absorption.

m the number of deformation bands per unit path length of incident radiation.

$\underline{q}$ the slip plane normal.

d slip plane or, alternatively, deformation band spacing.

$\underline{p}$ a reference direction in the scattering plane.

$d_1$ the projection of d in the scattering plane.

$d_2$ $= 1/m$.

$\varphi_3$ the angle between a reference direction in the scattering plane and the trace of the slip plane in the scattering plane.

$\varphi_2$ the angle between the direction of incidence and the projection of the slip plane normal in the scattering plane.

$S$ $= \frac{2}{\lambda}(\sin\omega - \sin\Theta_B)$.

$\bar{C}$ a constant describing dislocation character for analysis of x-ray diffraction profiles.